Synthesis and Magnetic Properties of Folate Chitosan Coated Cobalt Ferrite Nanoparticles for Biomedical Applications.

This dissertation is submitted in partial fulfillment of the requirements for the degree of

Master of Philosophy in Physics

Submitted by

Arijun Nahar

Registration No: 110, Session: 2015-2016

Department of Physics, University of Dhaka

February 2021

Declaration of Originity

This is certifying that the author is solely responsible for the work entitled, "Synthesis and Magnetic Properties of Folate Chitosan Coated Ferrite Nanoparticles for Biomedical Applications" and her work has not been submitted to any university or elsewhere for the award of any degree or diploma.

Author

(Arijun Nahar)
Registration No.: 110, Session: 2015-2016
Department of Physics
University of Dhaka

Supervisor

(Dr. Kazi Hanium Maria)
Associate Professor
Department of Physics
University of Dhaka

Joint- Supervisor

(Dr. Engr. Sheikh Manjura Hoque)
Head and Chief Scientific Officer
Materials Science Division
Atomic Energy Centre, Dhaka
Bangladesh Atomic Energy Commission

DEDICATED TO MY BELOVED PARENTS & HUSBAND

Acknowledgement

At the very first, I would like to express my admiration to praise the Almighty Allah who has given me the strength and opportunity to complete my research work and leading to M.Phil degree.

I take this opportunity to express my sincere gratitude and thanks to my honorable thesis supervisor Dr. Kazi Hanium Maria, Associate Professor, Department of Physics, University of Dhaka, for guiding me as a mentor and encourage me by her constant guidance and supervision throughout the work.

I express my deepest sense of gratitude and profound respect to my joint-supervisor honorable Dr. Engr. Sheikh Manjura Hoque, Head and Chief Scientific Officer (CSO), Material Science Division, Bangladesh Atomic Energy Commission for her invaluable time, dedication and helpful attitude provided during the work.

I am thankful to International Science Programme, Uppsala University to give me fellowship for my M. Phil degree.

I am thankful to Engr. Faizul Mohammad Kamal, CE, Dr. Md. Mahbubul Haque, CSO, Dr. Md. Nazrul Islam Khan, CSO, Dr. Md. Al Mamun, PSO, Dr. Harinarayan Das, PSO, Dr. Rimi Rashid, SE, Samia Islam Liba, SSO, Razibul Hasan, SSO and Arup Kumar, SO at Materials Science Division in Bangladesh Atomic Energy Commission for their valuable suggestions, affection and inspiration throughout the research work.

I would like to thank Alhamra Parveen, SEO, Anjuman Ara Begum, SEO, Kamrul Hasan Fakir, TO, Md. Anowar Hossain, SSA, Nazmun Nahar Begum, JEO, Zarna Begum, SA-1 and Nurul Islam, SA-1 at Materials Science Division in Bangladesh Atomic Energy Commission for their helps and cooperation during my research work.

Moreover, I am also thankful to Md. Dulal Hossain and Md. Aminul Islam, PhD students in Materials Science Division and my roommate Nijhum for their helps and supports during my thesis works. Finally, I would like to express my gratitude to my beloved parents and my husband for their tremendous support through all these years of my eduction. This dissertation would never have been possible without their love and affection.

Arijun Nahar

Abstract

Cobalt ferrite ($CoFe_2O_4$) nanoparticles were synthesized by co-precipitation method and were coated with biocompatible, biodegradable folate chitosan. The XRD studies confirmed the formation of single phase with inverse spinel structure. The lattice parameter calculated from XRD was founded to be 8.335 Å and average crystallite size was ~12 nm. Similar particle size (5-15 nm) was determined from the TEM analysis. A good crytallinity and single phase formation of the synthesized nanoparticles were confirmed using the HRTEM lattice fringes and SAED patterns diffraction rings, respectively. The value of saturation magnetization for uncoated $CoFe_2O_4$ nanoparticle was 44 emu/g and it was reduced to 40 emu/g for folate chitosan coating. The Mössbauer spectra demonstrated superparamagnetic phases embedded in the ferromagnetic matrix which had the good agreement with the M-H curve. The FTIR and Raman spectroscopy studies confirmed the spinel structure of the $CoFe_2O_4$ nanoparticle and coated $CoFe_2O_4$ nanoparticles. The DSC-TG curves show that the exothermal reaction and mass loss were occurred in the $CoFe_2O_4$ nanoparticle. The hydrodynamic size and polydispersity index of all the samples were varied from 143-361 nm and 0.185-0.331, respectively at different temperature which are promising results for biomedical applications. The positive zeta potential value of all the samples confirmed that the folate chitosan was stably coated on the surface of the nanoparticles. Induction heating of folate chitosan coated $CoFe_2O_4$ was investigated to reveal the self-heating temperature rising properties. The heating capability was found in the hyperthermia range (42-45 ºC) for all the samples. To demonstrate $CoFe_2O_4$ as a good contrast agent, the MRI images obtained from the phantoms and in-vivo experiments using *Albino Wister* rats.

Contents

List of Figures

List of Tables

Chapter 1: Introduction

1.1 Nanotechnology

Nanoscience is one of the most important topics in the modern scientific research. The thought of nanotechnology started with a talk entitled "There's Plenty of Room at the Bottom" by physicist Richard Feynman at an American Physical Society meeting at the California Institute of Technology on December 29, 1959, long before the term nanotechnology was used. Feynman mentioned about the miniaturization of atoms by manipulation of systems for data storage down to the scale of a single atom **[1].** Later, Japanese Professor Norio Taniguchi introduced the term nanotechnology in his explorations of ultra-precision machining **[2].** He also expressed the necessity of better microscopes systems. The first article on molecular nanotechnology published in 1974 and with the advent of technique such as Scanning Tunneling Microscope (STM) in 1981 and Atomic Force Microscope (AFM) in 1986, visualization of nano world become reality, which gave a pace to development of modern nanotechnology **[2].** Nanotechnology is helping to improve products across a range of areas, including food safety, medicine and health care, energy, transportation, communications, environmental protection and manufacturing. It is being used in the automotive, electronics and computing industries, household products, textiles, cosmetics and the list goes on **[3].**

1.1.1 Nanoparticle and nanoscale

Nanotechnology is beginning to allow scientists, engineers, chemists, and physicians to work at the molecular and cellular levels to produce important advances in the life sciences. The use of nanoparticles (NPs) offers major advantages due to their unique size and physicochemical properties **[4].** Biocompatible nanoparticles can be loaded with an optical imaging agent and used as drug **[5].** The entire entity migrates to the trouble spot in human body and release of the drug allows real time monitoring of the drug delivery by optical

imaging **[6].** Because of the widespread applications of nanoparticles (NPs) in biotechnology, biomedical, material science, engineering, and environmental areas, much attention has been paid to the synthesis of different kinds of nanoparticles. It is most important question that how small is nanoscale? The word "nanometer" defines a length unit of 1 nm= 10^{-9} m=10 Å. To have a clear idea of how large or tiny 1 nm is, take an example of individual atom that is up to a few Angstroms, or up to a few 10^{th} of nanometer, in diameter **[7].** How can we imagine the Nanoscale? Another way to imagine the nanoscale is to think in terms of relative sizes. Consider an ant of size 3-5 millimeters. An ant is roughly 1000 times smaller than a human. Now think of an ant with respect to the size of an amoeba (about 1 micron). An amoeba is about 1000 times smaller than an ant. Now, consider that a nanometer is roughly 1000 time smaller than an amoeba! Therefore, ant needs to shrink down by a factor of 1000 three times in a row in order to get down to the level of the nanoscale **[8].** What if we measured the size of various objects in terms of nanometers? A typical atom is anywhere from 0.1 to 0.5 nanometers in diameter. DNA molecules are about 2.5 nanometers wide. Most proteins are about 10 nanometers wide, and a typical virus is about 100 nanometers wide. A bacterium is about 1000 nanometers. Human cells, such as red blood cells, are about 10,000 nanometers across. At 100,000 nanometers, the width of a human hair seems gigantic. The head of a pin is about a million nanometers wide. An adult man who is 2 meters tall (6 feet 5 inches) is about 2 billion nanometers tall **[8].**

On a comparative scale, if a marble were a nanometer, then one meter would be the size of the Earth. Therefore, nano is super, super tiny. In general, material systems with possible size 1-100 nm range by virtue of possessing large surface to volume ratio come within the periphery of nanomaterial or nanosystems or nanometric system or nanostructural systems.

1.2 Magnetic nanoparticles

Among nanomaterials (NMs), magnetic nanoparticles (MNPs) are one of the very vital and extensively exploited subcategories of NMs. MNMs are usually multi-component, characteristically enclosed with nano-scale magnetic constituents to trigger the response to an external magnetic field **[9].** Magnetic nanoparticles (MNPs) have gained a lot of attention in biomedical applications due to their biocompatibility, easy surface modification, large magnetic anisotropy constant and saturation magnetization **[10].** Therapeutic agents are attached to, or encapsulated within MNPs to form the MNPs/therapeutic agent co-complex. These magnetic carriers are injected into the blood-stream and guided to focus over the tumor location through external applied inhomogeneous magnetic fields **[11].** MNPs tend to agglomerate because of their large surface energy and strong magnetic interactions **[12].** In recent years, there has been intense research interest in the fabrications of core-shell particles with suitable properties for various applications in materials science. The properties of the core-shell can be significantly changed by the shell surrounding **[13].** The Fe_3O_4 nanoparticles can be synthesized by co-precipitation route **[14].** As MNPs are used in a wide variety of biomedical applications, their toxicity should be taken into account. The toxicity depends on the various factors such as the size of the particle, chemical composition and coated materials **[15].** To remove the toxicity and make biocompatible a biological or molecular coating or layer should be attached to the MNPs.

A variety of magnetic nanoparticles composed of different atoms or ions with different magnetic moments have been synthesized to target these applications. Metal nanoparticles such as Fe_3O_4 (magnetite), γ-Fe_2O_3 (maghemite), and spinel structured magnetic nanoparticles (MFe_2O_4, M = Fe, Co, Ni, Mn) have been widely used for their applications in nanomedicine **[16],** while metal nanoparticles have stability problems in atmospheric condition. However, metal oxides are stable under ambient conditions. For example, the

well-known iron oxide Ferro fluid becomes undesirable because of their iron atoms are poorly distinguishable from those of hemoglobin **[17].** A conceivable solution is to use mixed-ferrites using highly magnetic materials such as Cobalt and Nickel. Those ferrites have attracted special attention because of their easy synthesis, physical and chemical stability, and suitable magnetic properties **[18].**

1.3 Prospect of magnetic nanomaterial in biomedical applications

The magnetic nanoparticles (MNPs) have gained a lot of attention in biomedical application for their biocompatibility and their surface can be easily modified. The short description of various applications of MNPs is given below.

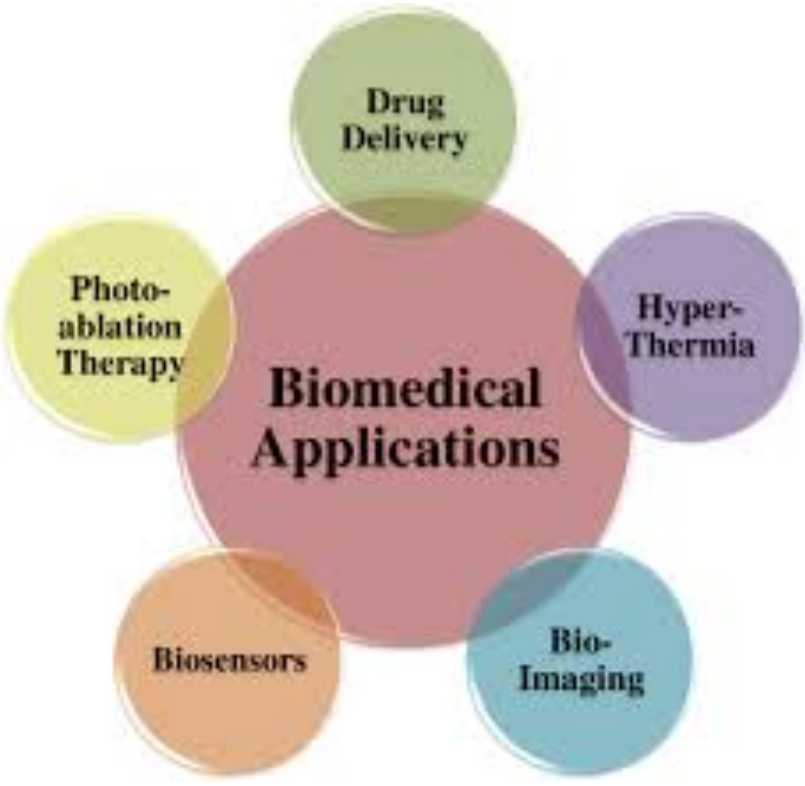

Figure 1.1: Biomedical application of magnetic nanoparticle, retrieved from **[19]**

1.3.1 Nanoparticles use in cancer prevention, diagnosis and therapy

Cancer is a leading cause of morbidity and mortality worldwide. Unfortunately, the antitumor drugs have significant side effects; hence finding new ways to improve their efficacy and specificity being one of the top research directions. Due to their unique physical and chemical properties, nanoparticles are promising candidates for the development of efficient early diagnosis and therapeutic tools, A great variety of nanostructured materials, such as inorganic (iron oxide, titanium dioxide, gold, and silver) nanoparticles, quantum dots, nano encapsulation, polymeric, liposomes, micelles, ceramic based carriers, dendrimers, nano shells, and carbon nanotubes, are presently investigated for their potential applications in the anticancer therapy **[20].** Due to their properties, NPs harbor many biomedical applications including (i) carrier, for drug and gene delivery; (ii) biosensors, for detection of pathogens or proteins; (iii) therapeutic substances **[21].**

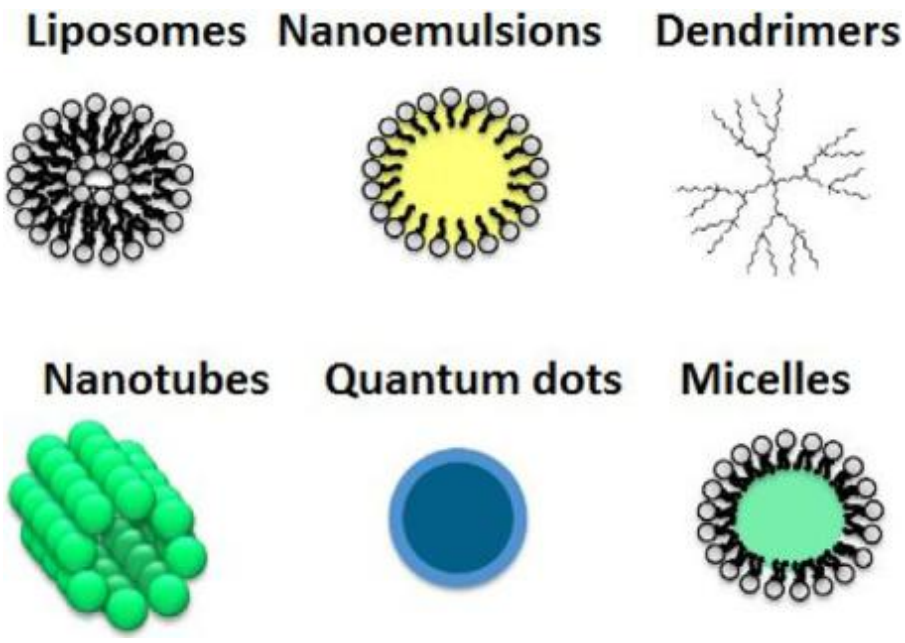

Figure 1.2: Schematic representation of the most common nanoparticle systems used for cancer treatment, retrieved from **[21].**

1.3.2 Nanoparticles use in hyperthermia

Hyperthermia (HT) represents one of the emerging methods currently being tested for cancer treatment, in consort with resection surgery, chemotherapy, radiotherapy, gene therapy, and immunotherapy. It is a procedure that increases tissue temperature above normal in order to kill cancer cells or inhibit their growth. Usually, normal tissues have resistance to temperatures of 42–45 °C, in contrast to cancer cells that experience apoptosis at those temperatures. Although tumor treatment with heat has been applied since many centuries ago (The time of ancient Greeks, Egyptians, and Romans), the use of this procedure has some limits. These comprise the struggle to precisely achieve uniform heat dispersion all over the tumor without damaging healthy cells (due to overheating), targeting invisible micro metastases **[22].** To be operational aspirants for cancer-assisted hyperthermia, nanoparticles must have a low toxicity, biocompatibility, ease of functionalization, and cell acceptance and, essentially, able to make effective heating profiles when exposed to an applied magnetic field. Over the last decades, numerous reviews on synthesis routes, functionalization, and magnetic properties of MNPs for biomedical applications have been published. In this respect, a plethora of synthesized MNPs with varied characteristics and magnetizations for both in vivo and in vitro HT have been studied **[22].**

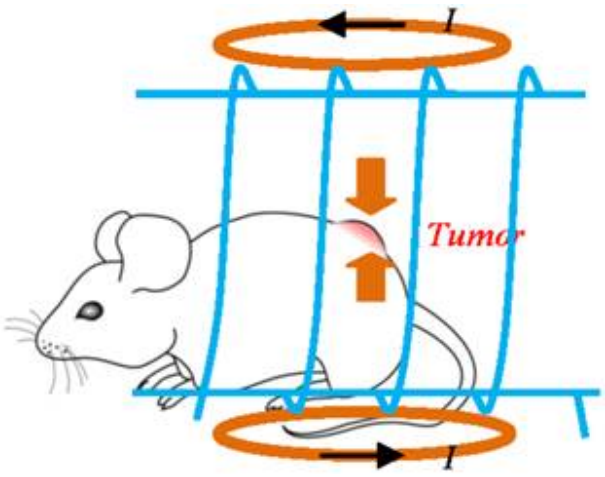

Figure 1.3: Magnetic nanoparticle based hyperthermia, retrieved from **[23].**

1.3.3 Magnetic resonance imaging

Magnetic Resonance Imaging (MRI) is a non-invasive imaging modality that offers both anatomical and functional information. Relaxation in Nuclear Magnetic Resonance (NMR) spectroscopy plays a pivotal role. Intrinsic longitudinal and transverse relaxation times (T_1 and T_2, respectively) provide tools to manipulate image contrast. The emphasis in MRI is on longitudinal (spin-lattice) and transverse (spin-spin) relaxation times (T_1 and T_2, respectively The advent in technology and the spread of higher field strength magnets made available a wealth of imaging pulse sequence that rely on the manipulation of T_1 and T_2 weighting to produce different diagnostic information. Early quantification of relaxation times in biological tissues hoped to find a consistent difference in their values between malignant tumors and normal tissues **[24].** Iron oxide nanoparticles (IONPs) are extensively employed beyond regenerative medicines to imaging disciplines because of their great constituents for magneto responsive nano systems. The unique superparamagnetic behavior makes it very suitable for imaging applications. From the last decade, versatile functionalization with surface capabilities, efficient contrast properties and biocompatibilities make IONPs an essential imaging contrast agent for MRI. IONPs have shown signals for both longitudinal relaxation and transverse relaxation; therefore, negative contrast as well as dual contrast can be used for imaging in MRI **[25].**

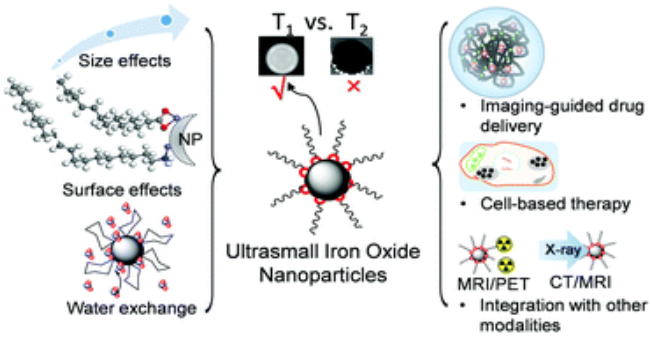

Figure 1.4: Magnetic iron oxide nanoparticles as T_1 contrast agents for MRI, retrieved from **[26]**

1.4 Reason for selecting $CoFe_2O_4$ and coated with folate chitosan

The biocompatibility and toxicity less nanoparticle is needed for the biomedical application. Some of the recent works refer to the understanding of the biocompatibility and toxicity of nanoparticles **[27]**. For biomedical uses, the application of particles that present superparamagnetic behavior at room temperature is preferred. Furthermore, applications in therapy and biology and medical diagnosis require the magnetic particles to be stable in water at pH 7 and in a physiological environment. Among spinel ferrites, $CoFe_2O_4$ has larger coercivity (~ 5 kOe), permeability, reasonable magnetic saturation (~ 80 emu), chemical stability, mechanical hardness, high electromagnetic, magneto-optic performance **[28]**, and tunable magnetic properties at the atomic level **[29].** Therefore, cobalt ferrite is a talented contestant material for high-density magnetic recordings, ferro-fluids, drug delivery, magnetic resonance imaging (MRI), and hyperthermia treatment and in magneto-optical devices **[30].** Cobalt ferrites nanoparticles are also suitable for the isolation and purification of genomic DNA, the separation of PCR (polymerase chain reaction) ready DNA **[31]**.

For in vivo biomedical applications, magnetic nanoparticles must be made of a non-toxic and non-immunogenic material, with particle sizes small enough to remain in the circulation after injection and to pass through the capillary systems of organs and tissues, avoiding vessel embolism **[32].** They must also have a high magnetization so that their movement in the blood can be controlled with a magnetic field and so that they can be immobilized close to the targeted pathologic tissue. As MNPs have been used for a wide variety of biomedical applications, their toxicity should be investigated in detail. As a promising candidate for biomedical applications we would study thoroughly the superparamagnetic nano-ferrite with biocompatible coating of folate chitosan for hyperthermia protocol of cancer and its toxic effects on the human body. Synthesis methods play a very important role in undermining the

toxicity of nanoparticles as it controls the cation distribution, physicochemical properties, and presence of residual reagents.

Further, the application of nanoparticles in biomedicine fields, such as cancer diagnosis, and therapy, involves direct human exposure. Thus, it is worth to know the toxic effects of nanoparticles in in-vivo experiments (healthy adult rat, for example) before their use in human treatments and diagnostics.

1.5 Review of earlier research

Akbarzadeh et al. addressed some relevant findings on the importance of having well defined synthetic strategies developed for the generation of MNPs, with a focus on particle formation mechanism and recent modifications made on the preparation of monodisperse samples of relatively large quantities not only with similar physical features, but also with similar crystallochemical characteristics **[4]**. Then, different methodologies for the functionalization of the prepared MNPs together with the characterization techniques are explained. Theoretical views on the magnetism of nanoparticles are considered.

Mc Bain et al. investigated the magnetic micro and nanoparticles for targeted drug delivery that began over 30 years ago **[9]**. Since that time, major progress has been made in particle design and synthesis techniques, however, very few clinical trials have taken place. Here we review advances in magnetic nanoparticle design, in vitro and animal experiments with magnetic nanoparticle based drug and gene delivery, and clinical trials of drug targeting. Though progress in clinical applications of magnetically targeted carriers has been slow since first introduced in the 1970s, the potential for this technique remains great. Rapid developments in particle synthesis have enabled the use of new materials for more efficient capture and targeting and novel strategies are being developed for applying magnetic fields which could lead to treatments for diseases such as cystic fibrosis and localized cancerous

tumors. Though clinical trials are few, the results have been promising. While magnetic targeting is not likely to be effective in all situations, with further development it should provide another tool for the effective treatment of a variety of diseases.

Kafrouni et al. reported that, nanomaterials science contributed to developing new micro and nano devices as potential diagnostic and therapeutic tools in the field of oncology **[10]**. The synthesis of superparamagnetic nanoparticles (SPMNPs) has been intensively studied, and the use of these particles in magnetic hyperthermia therapy has demonstrated successes in the treatment of cancer. However, few physical limitations have been found to impact the heating efficiency required to kill cancer cells. Moreover, the safety issues of these particles have not been completely solved because it is difficult to compare the cytotoxicity data since the toxic effects of NPs are influenced by many parameters (such as size distribution, surface coating, magnetic properties, etc.). Also, numerous studies showed contradicting findings since different cell types will interact with the same particle in different ways. Moreover, the lack of coherence between various research activities for establishing priorities among the research needs is one reason why a toxicological profile of these particles has not yet been well documented in the literature. Therefore, along with the expanding applications of NPs and the growing numbers of consumer products containing NPs, the release of these substances into the environment is expected, and the impact of these materials is increasing significantly. In their study, they reviewed the basics of magnetic properties and nontoxicity of NPs for magnetic hyperthermia.

Wu et al. reported that the magnetic nanoparticles (MNPs) have been widely applied in the area of biomedicine in recent years due to their broad versatility, such as good biological compatibility, unique physicochemical properties, and easy guidance by external magnetic fields **[11]**. In their review, they have summarized the synthesis, function and biomedicine applications of magnetic nanoparticles. The concept of employing magnetic nanoparticles on

the biomedicine applications greatly benefits from the rapid development of the nanotechnology. On one hand, the magnetic nanoparticles with controlled and narrowly distributed sizes can be synthesized by delicately selecting the experimental conditions, while on the other hand, surface functionalization of the magnetic nanoparticles with various biomolecules, which is highly essential for the biomedicine application, has been developed and demonstrated by the rational design of both the composition of the magnetic nanoparticles and the molecular structure of the biomolecules. These functionalized magnetic nanoparticles with high selectivity, high sensitivity and unique magnetic properties exhibit the superiority not only over the traditional methods or agents used in the bioseparation, biosensing and magnetic resonance imaging by increasing the efficiency and accuracy, but also in the drug delivery and hyperthermia by increasing the specificity and reducing the damage of the health human tissues during the in-vivo treatment.

Pankhurst et al. reviewed the physical principles underlying some current biomedical applications of magnetic nanoparticles. Starting from well-known basic concepts, and drawing on examples from biology and biomedicine **[17]**, the relevant physics of magnetic materials and their responses to applied magnetic fields are surveyed. The way these properties are controlled and used is illustrated with reference to (i) magnetic separation of labelled cells and other biological entities; (ii) therapeutic drug, gene, and radionuclide delivery; (iii) radio frequency methods for the catabolism of tumors via hyperthermia; and (iv) contrast enhancement agents for magnetic resonance imaging applications.

Cheng et al. reported the vasodilatory effect of folate chitosan nanoparticles, ligustrazine (LZ) improves the sensitivity of multidrug resistant cancer cells to chemotherapeutic agents **[33]**. To enhance the specificity of LZ delivery to tumor cells/tissues, folate chitosan nanoparticles (FA-CS-NPs) were synthesized by a combination of folate ester with the amine group on chitosan to serve as a delivery vehicle for LZ (FA-CS-LZ-NPs). The structure of

folate-chitosan and characteristics of FA-CS-LZ-NPs, including its size, encapsulation efficiency, loading capacity and release rates were analyzed. MCF-7 (folate receptor-positive) and A549 (folate receptor-negative) cells cultured with or without folate were treated with FA-CS-LZ-NPs, CS-LZ-NPs or LZ to determine cancer targeting specificity of FA-CS-LZ-NPs. Fluorescence intensity of intracellular LZ was observed by laser scanning confocal microscopy, and the concentration of intracellular LZ was detected by HPLC. The average size of FA-CS-LZ-NPs was 182.7±0.56 nm, and the encapsulation efficiency and loading capacity was 59.6±0.23 and 15.3±0.16%, respectively. The cumulative release rate was about 95% at pH 5.0, which was higher than that at pH 7.4. There was higher intracellular LZ accumulation in MCF-7 than that in A549 cells and intracellular LZ concentration was not high when MCF-7 cells were cultured with folate. These results indicated that the targeting specificity of FA-CS-LZ-NPs was mediated by folate receptor. Therefore, the FA-CS-LZ-NPs may be a potential folate receptor-positive tumor cell targeting drug delivery system that could possibly overcome multidrug resistance during cancer therapy.

Hoque et al. synthesized $ZnFe_2O_4$ nanoparticles and coated this nanoparticle with chitosan and PEG **[34]**. X-ray diffraction studies confirmed the formation of single phase spinel structure of the synthesized samples. The lattice parameter turned out to be 8.48 Å and grain size 4.8 nm. Similar particle size was observed by transmission electron microscope analysis. HRTEM studies showed the distinct lattice fringes thus confirming the good crystallinity of the synthesized nanoparticles. M-H curve at room temperature showed the prepared sample was superparamagnetic in nature, which is also confirmed by the doublets of Mössbauer spectroscopy. Relaxivity values (r_2) of chitosan and PEG coated $ZnFe_2O_4$ nanoparticles are 68 $mM^{-1}s^{-1}$ and 76 $mM^{-1}s^{-1}$ respectively. The r_2 relativity was found as 54 $mM^{-1}s^{-1}$. MRI images obtained from the in vitro experiments based on phantoms

demonstrated good contrast enhancement. Induction heating of bare and coated particles was investigated to reveal the self-heating temperature rising properties of $ZnFe_2O_4$ nanoparticles.

Nasrin et al. synthesized $Mn_{1-x}Zn_xFe_2O_4$ (0.2, 0.4, 0.6, 0.8, 1.0) by co-precipitation method and coated the samples with biocompatible and biodegradable chitosan **[35]**. Face centered cubic structure of the nano ferrites has been revealed by XRD analysis and the mean crystalline size was 6nm. The TEM determined the particle size of the samples 5-7 nm. EDS studies confirmed the presence of all the elemental distribution of both bare and coated ferrite nanoparticles. The value of saturation magnetization of $Mn_{1-x}Zn_xFe_2O_4$(x = 0.4 and 0.6) is more than that of $Mn_{0.8}Zn_{0.2}Fe_2O_4$. The maximum saturation magnetization value for $Mn_{0.4}Zn_{0.6}Fe_2O_4$ is 15 emu/g, and it reduces to 12 emu/g for $ZnFe_2O_4$. This range of saturation magnetization is appropriate to generate temperature with the low radio frequency field and can provide the enhanced heating profile for hyperthermia purpose. Mössbauer results showed that for x=0.2; manganese, iron, and zinc irons are dispersed over the tetrahedral and octahedral sites and exhibit ferromagnetic nature. A ferromagnetic to super-magnetic transition occurs with the increase of Zn content. From DLS scattering data, it has been observed that the hydrodynamic diameter and polydispersity index (PDI) of the samples varies from 78 nm to 218 nm and 0.271 to 0.328 at 45 ^oC respectively. The heating capability was found in the hyperthermia range for samples x= 0.4 and 1.0.

Hoque et al. synthesized $Fe_xCo_{1-x}Fe_2O_4$ (where x ranges from 0.2 to 0.8) by chemical co-precipitation under N_2 atmosphere and ambient temperature **[36]**. Structural characterization was performed with XRD, TEM, and Mössbauer spectroscopy. Magnetization studies were performed on both bare and coated particles. Both the maximum magnetization M_{max} and the coercivity H_C values significantly reduced for the coated particles compared to the bare particles. High performance was noticed with the mortality of 9L rat gliosarcoma cells by the

magnetic particle hyperthermia experiments using chitosan and PEG coated suspensions of the nanoparticles with an RF field of 400 kHz and 76 mT. The T_2 relaxivities were quite high for most of the samples and followed values of saturation magnetization of the coated particles. While different types of coating, such as chitosan and PEG, changed the values of both SLP and T_2 relaxivity. Their results lay the ground work for future in vivo biomedical applications of these Fe-Co mixed spinel ferrites.

Hoque et al. reported the thermo-therapeutic applications of chitosan and PEG-coated nickel ferrite ($NiFe_2O_4$) nanoparticles **[37]**. In this study $NiFe_2O_4$ nanoparticles were synthesized by the co-precipitation method, tuning the particle size through heat treatment in the temperature range from 200–800 °C for 3h. XRD and TEM analysis revealed that the ultrafine nanoparticles were of size 2–58 nm. Crystallinity of the $NiFe_2O_4$ nanoparticles in the as-dried condition with the particle size 2-3 nm was confirmed from the presence of a lattice fringe in the HRTEM image. VSM measurements showed that the superparamagnetic/ferromagnetic transition occurs with increasing particle size, which was further confirmed by Mössbauer spectroscopy. The nickel ferrite nanoparticles with an optimum particle size of 10 nm were then coated with materials commonly used for biomedical applications, i.e. chitosan and PEG, to form homogeneous suspensions. The hydrodynamic diameter and the polydispersity index (PDI) were analyzed by dynamic light scattering at the physiological temperature of 37 °C and found to be 187 nm and 0.21 for chitosan coated nanoparticles and 285 nm and 0.32 for PEG coated ones. The specific loss power of r_f induction heating by the set-up for hyperthermia and r_2 relaxivity by the nuclear magnetic resonance were determined. The results of induction heating measurements showed that the temperature attained by the nanoparticles of size 10 nm and concentration of about 20 mg/ml was >70 °C (for chitosan) and >64 °C (for PEG). It has been demonstrated that the required temperature for hyperthermia heating could be tuned by tuning the particle size, shape and magnetization and

the concentration of the solution. The concentration dependence of T_1 and T_2 relaxation was further evaluated by NMR studies and found to be linear. The ratio, r_2/r_1 shows that, this is applicable as a T_2 contrast agent for magnetic resonance imaging.

Das et al. reported the structural, magnetic and heat generation properties of $La_{0.77}Sr_{0.23}MnO_3$ (LSMO) nanoparticles with different crystallite size to the proper application of self-controlled magnetic hyperthermia treatments of cancer **[38]**. They synthesized a series of nanocrystalline LSMO manganite by the polymerized complex method and then subsequently annealed at the different temperature from 600 to 1400 ^oC to obtain various crystallite size. Phase formation and crystal structure of the prepared powder were determined by the powder X-ray diffraction (XRD) using Rietveld analysis. The XRD patterns reveal that all powder samples are a single phase rhombohedral perovskite like structure with *R*3*c* space group. The mean crystallite size of prepared particles varied from 19 to 243.8 nm with the increase of the annealing temperature starting from 600 to 1400 °C. The field emission scanning electron microscopy (FESEM) analysis shows the surface morphology with a strong agglomeration of fine nanoparticles. The magnetic study reveals that these nanoparticles exhibit ferromagnetic nature with a different value of magnetization, coercivity, curie temperature which is strongly dependent on their crystallite size. The maximum saturation temperature (T_S¼ 66 °C) under AC magnetic field (H ¼ 1.77 kA/m, f ¼ 370 kHz) was found for the crystallite size of 39.5 nm due to its pure single domain phase. Such LSMO nanoparticles, having the higher heating rate, can be used in magnetically induced hyperthermia cancer treatment.

Roy et al. synthesized cobalt ferrite ($CoFe_2O_4$) nanoparticles by chemical co-precipitation method **[39]**. They studied the effect of annealing temperatures on the structural parameters and magnetic properties of the sample. X-ray powder diffraction (XRD), transmission electron microscope (TEM) and SAD pattern demonstrated that single face (fcc) spinel

structure of $CoFe_2O_4$ has been formed showing particles in completely crystalline state which was further confirmed by the lattice parameter and the unmixed hkl values. The particle size is in the range of about 5-10 nm depending on the annealing temperature from 200 to 400 °C. The grain growth occurred monotonically with the increase of annealing temperature. The magnetic properties demonstrated a strong dependence on particle size. The saturation magnetization M_S, remanent ratio M_R/M_S and coercivity H_C increased with the increase of particle size. The hysteresis curves for samples of different grain size showed the ferromagnetic behavior which is completely analogous to the slow relaxation sextet peaks of Mossbauer spectroscopy. Other parameters such as chemical shift, quadruple splitting and hyperfine field and site occupancy of Fe^{3+} were determined by Mossbauer spectroscopy. Ferrimagnetic to superparamagnetic transition temperature known as blocking temperature T_B was determined from the temperature dependent magnetization curves. With the increase of grain size, blocking temperature also increases. Maximum entropy changes due to magnetic phase transition were also observed for mentioned annealing temperatures in the context of the magneto caloric effect.

Gingasu et al. synthesized chitosan-coated cobalt ferrites by wet ferritization method through two different approaches **[40]**. X-ray diffraction patterns confirmed the formation of $CoFe_2O_4$ cubic spinel structure with an average crystallite size of 1.75 nm and 5.5 nm, respectively. Mössbauer spectra consist in a central quadruple pattern. The deconvolution in the hypothesis of the Lorentzian line shape evidences the prevailing presence of Fe^{3+} ions at the nano particle surface. The antimicrobial activity of chitosan-coated cobalt ferrites against gram-positive and gram-negative bacteria, as well as fungal strains was investigated. Based on the results, chitosan-coated cobalt ferrites are thought to be suitable candidates for the development of novel anti-biofilm agents.

Sun et al. synthesized the nano conjugate by coating superparamagnetic iron oxide nanoparticles with covalently bound bifunctional poly (ethylene glycol) (PEG), followed by conjugation with folic acid (FA) **[41]**. The specificity of the nano conjugate targeting cancerous cells was demonstrated by comparative intracellular uptake of the nano conjugate and PEG/dextran-coated nanoparticles by human adenocarcinoma HeLa cells. Preferential targeting to cancerous cells was studied by comparing the uptake of the nano conjugate by HeLa cells and by non-FR expressing osteosarcoma MG-63 cells. Uptake of the nano conjugate by HeLa cells after 4 h incubation was found to be a 12-fold higher than that of PEG or dextran coated nanoparticles as quantified by inductively coupled plasma spectroscopy. A significant negative contrast enhancement was observed with magnetic resonance (MR) phantom imaging for HeLa cells over MG-63 cells, when both were cultured with the nano conjugate. Specificity of the nano conjugate for folate receptors was also verified with a competitive inhibition assay, in which HeLa cells were incubated with both NP–PEG–FA and free FA. The bifunctional PEG used has amide linkages within the PEG chains that can form interchange hydrogen bonding, leading to improved stability of the PEG coating. Self-assembled PEG can be controlled at the molecular level and are suitable for nanoscale coatings.

Unsoy et al. synthesized the chitosan coated magnetic nanoparticles (CS MNPs) by cross linking method **[42]**. The XRD and XPS analysis proved that the synthesized iron oxide was magnetite (Fe_3O_4). The layer of chitosan on the magnetite surface was confirmed by FTIR. TEM results demonstrated a spherical morphology. In the synthesis, at higher NH_4OH concentrations, smaller sized nanoparticles were obtained. From the TEM data they measured the average diameters were generally between 2-8 nm. The average diameters of bare MNPs were found as around 18 nm both in TEM and DLS. TGA results indicated that the chitosan content of CS MNPs were between 15 and 23 % by weight. Bare and CS MNPs were

superparamagnetic. These nanoparticles were found non cytotoxic on cancer cell lines (SiHa, HeLa). The synthesized MNPs have many potential applications in biomedicine including targeted drug delivery, magnetic resonance imaging (MRI), and magnetic hyperthermia.

Kima et al. synthesized cobalt ferrite ($CoFe_2O_4$) magnetic nanoparticles by co-precipitation method **[43]**. The average particle size could be varied in the range of 2–14 nm by controlling co-precipitation temperature. The average particle sizes of the ferrites, estimated from XRD line broadening, were 2.0, 2.4, 9.2 and 13.8 nm when the precipitation temperatures are 20 ^oC, 40 ^oC, 60 ^oC and 80 ^oC, respectively. As the precipitation temperature increased, the average sizes increased. However, there was a transition in size and crystallinity at the temperature between 40 ^oC and 60 ^oC. The field dependent and temperature dependent magnetization measurements and Mossbauer spectra measured at various temperatures showed that the cobalt ferrites nanoparticles prepared at the temperature lower than 40 ^oC are entirely superparamagnetic at room temperature with TB of around 80 K and those, prepared at temperatures higher than 60 ^oC, consisted of superparamagnetic and ferromagnetic components with TB higher than 673 ^oC. For the latter, the fraction of superparamagnetic components decreased as the precipitation temperature increased with the increased particle size.

Gyergyek et al. synthesized the Co ferrite nanoparticles by three different methods having a relatively uniform size distribution around 8 nm **[44]**. The methods were: (1) A simple co-precipitation from aqueous solutions (2) A co-precipitation in an environment of microemulsions are low temperature methods at 50 °C (3) A thermal decomposition of organometallic complexes was performed at elevated temperature of 290 °C. The X-ray diffractometer (XRD) confirmed the spinel structure, and the high-resolution transmission electron microscopy (HRTEM) a good crystallinity of all the nanoparticles. Energy dispersive X-ray spectroscopy (EDS) showed the composition close to stoichiometric ($CoFe_2O_4$) for

both co-precipitation method nanoparticles, whereas the nanoparticles prepared by the thermal decomposition were Coefficients. The variations in cation distribution within the spinel lattice were observed by structural refinement of X-ray absorption fine structure (EXAFS). Like the bulk $CoFe_2O_4$, the nanoparticles synthesized at elevated temperature using thermal decomposition displayed inverse spinel structure with the Co ions occupying predominantly octahedral lattice sites, whereas co-precipitated samples showed considerable proportion of cobalt ions occupying tetrahedral sites (nearly 1/3 for the nanoparticles synthesized by co-precipitation from aqueous solutions and almost 1/4 for the nanoparticles synthesized in micro emulsions). Magnetic measurements performed at room temperature and at 10 K were in good agreement with the nanoparticles composition and the cation distribution in their structure. The presented study clearly shows that the distribution of the cations within the spinel lattice of the ferrite nanoparticles, and consequently their magnetic properties are strongly affected by the synthesis method.

Houshiar et al. synthesized the cobalt ferrite ($CoFe_2O_4$) nanoparticles by using three different methods; combustion, co-precipitation, and precipitation **[45]**. XRD data analysis showed an average size of 69.5 nm for combustion, 49.5 nm for co-precipitation, and 34.7 nm for precipitation samples. XRD data further revealed a reverse cubic spinel structure with the space group Fd-3m in all three samples. VSM data of samples showed a saturation point in the magnetic field of less than 15 kOe. Magnetization saturation (MS) was 56.7 emu/g for combustion synthesized samples, 55.8 emu/g for co-precipitation samples, and 47.2 emu/g for precipitation samples. Coercivity (Hc) was 2002 Oe for combustion synthesized samples, 850 Oe for co-precipitation samples, and 233 Oe for precipitation samples. These results show that various method of nanoparticle synthesis can lead to different particle sizes and magnetic properties. H_C and M_S are greatest in the combustion method and least in the precipitation method. Combustion method is simple and quick. The rate of fuel to nitrates can

highly affect the size and magnetic properties. In co-precipitation method the size is controlled by the quick addition of the precipitating agent (sodium hydroxide) with the salt solution and performing vigorous stirring during the reaction.

Amiri et al. said that cobalt ferrite nanoparticles is one of the competitive candidates because of its suitable physical, chemical and magnetic properties like the high anisotropy constant, high coercivity and high Curie temperature, moderate saturation magnetization and ease of synthesis **[46]**. This paper introduces the magnetic properties, synthesis methods and some medical applications, including the hyperthermia, magnetic resonance imaging (MRI), magnetic separation and drug delivery of cobalt ferrite nanoparticles. Cobalt ferrite nanoparticles with good physical and magnetic properties can be produced by several synthesis methods, including conventional and chemical ones used for different applications, especially in the medical field. A number of properties such as high coercivity, strong (L-S) coupling, high magnetic anisotropy, small super-paramagnetic size at room temperature and moderate saturation magnetization make it suitable for hyperthermia. Also the high relaxivity, anisotropy energy and initial susceptibility make it appropriate for MRI imaging. Moreover, due to good electrostatic interaction, it can be used for magnetic separation. The ability to be functionalized with drug and coatings make it a good carrier in drug delivery applications, particularly chemotherapy.

Yuqiu et al. synthesized Cobalt ferrite nanoparticles by using co-precipitation technique at different temperatures **[47]**. The effect of reaction temperature on the particle size and magnetic properties of the nanoparticles have been studied. XRD patterns, TEM and FESEM micrographs show the formation of uniaxial shaped single-phase cubic spinel structure and the increase of particle size with the increasing reaction temperature. Raman spectra confirm the formation of $CoFe_2O_4$ nanoparticles. The results of VSM indicate that the saturation magnetization of $CoFe_2O_4$ increases with the increase of reaction temperature and shows a

maximum saturation magnetization of 29.5 emu/g at room temperature. The variations of coercivity and remanence ratio are dependent on the particle size. The maximum values of coercivity and remanence ratio are 3267 Oe and 0.58, respectively. The variations may be attributed to the single domain size of ca. 34 nm, below and above which the magnetization mechanism for particles will be different. The critical size of superparamagnetic transformation is about 9 nm determined by TEM and FESEM.

1.6 Objective of the research work

The objective of this research is to synthesis cobalt ferrite nanoparticle and to coat it by biocompatible material to exploit their biomedical application. Among various methods for synthesis of magnetic nanoparticle, co-precipitation process has several advantages over other methods including good homogeneity, low cost, high purity of product and not requiring organic solvent. So the cobalt ferrite nanoparticles will be prepared chemical co-precipitation method where the pH of the solution will be kept controlled in the range 11-13. After that solvent will allowed to precipitate. Finally, after washing the sample it will be annealed at 80 ^{o}C for 72 h to get the final product. The outline of methodology might be enlisted below:

- Superparamagnetic nanaoparticle of $CoFe_2O_4$ have been synthesized by the chemical co-precipitation method. After that the prepared samples have been coated by biocompatible folate chitosan.
- XRD characterization has been done to know about the crystal structure and crystallinity.
- Transmission electron beam (TEM) images have been done to determine the particle size.

- The VSM characterization has been performed by PPMS to study the magnetic behavior of the synthesis nanomaterials along with all the characterization like saturation magnetization and coercivity.
- Hydrodynamic size distribution of the sample will be investigated by dynamic light scattering (DLS).
- The Zeta potential has been done to determine the surface stability of the suspension of the coated sample.
- The Raman spectroscopy has been done to determine the sample structure.
- The FTIR has been done to confirm the bonding of the sample.
- Mossbauer studies have been performed to analysis the cation distribution. the isomer shift; quadruple splitting and hyperfine field splitting will be measured.
- The induction heating properties of the sample will be investigated by the magnetic hyperthermia setup and from here specific loss factor would be investigated.

1.7 Overview of the thesis

In this thesis the magnetic nanoparticles were synthesized for biomedical application. Then the sample was coated with biodegradable and biocompatible folate chitosan. This thesis is confined into five chapters which are as follows.

In chapter 1 includes the introduction of Cobalt ferrites and its magnetic properties which made it biomedical applicable. This chapter incorporates information to understand the aims and objectives of this investigation and also reviews of recent reports by other investigations with which these results can compare.

In chapter 2 an introduction to the general properties of the magnetic particles together with some theoretical background related to the present work have been discussed. Also a brief discussion of the various synthesis method of cobalt ferrites nanoparticles.

In chapter 3 includes the details description of the sample preparation and the brief description of the experimental setup and instrumentation for the different characterization of the samples.

Chapter 4 represents the structural (XRD, Raman, FTIR), magnetic properties (VSM, Mössbauer), thermal properties (DSC, TGA) of the sample. The hydrodynamic diameter and the zeta potential of the folate chitosan coated sample also have been described. Finally, we report the hyperthermia effect of the samples.

Finally, in Chapter 5 an overall conclusion with the suggestions for the further research on this field is given.

References are added at the end.

Chapter 2: Theoretical Background

2.1. Class of magnetic materials

The origin of magnetism lies in the orbital and spin motions of electrons and how the electrons interact with one another. The best way to introduce the different types of magnetism is to describe how materials respond to magnetic fields. The behavior of the magnetic materials can be classified into five categories as diamagnetism, paramagnetic, ferromagnetism, anti-ferromagnetism and ferrimagnetism. Fig. 2.1 shows the magnetic arrangements of paramagnetic, ferromagnetic, anti-ferromagnetic and ferromagnetic materials.

2.1.1. Diamagnetism

Diamagnetism is a fundamental property of all matter, although it is usually very weak. It is due to the non-cooperative behavior of orbiting electrons when exposed to an applied magnetic field. Diamagnetic substances are composed of atoms that have no net magnetic moments (i.e., all the orbital shells are filled and there are no unpaired electrons). However, when exposed to a field, a negative magnetization is produced and thus the susceptibility is negative **[48].**

2.1.2. Paramagnetism

In paramagnet, some of the atoms or ions in the material have a net magnetic moment due to unpaired electrons in partially filled orbitals. One of the most important atoms with unpaired electrons is iron. However, the individual magnetic moments do not interact magnetically, and like diamagnetism, the magnetization is zero when the field is removed. In the presence of a field, there is now a partial alignment of the atomic magnetic moments in the direction of the field, resulting in a net positive magnetization and positive susceptibility **[48]**. Pierre Curie showed that in these cases, the susceptibility (χ) which is defined as

$$\chi = M/H \quad (2.1)$$

Where χ = susceptibility, M = magnetization or moment, H = Magnetic field strength follows the Curie Law given as,

$$\chi = C/T \quad (2.2)$$

Where: C = Curie constant, T = Temperature in Degrees Kelvin

Also, $$1/\chi = T/C \quad (2.3)$$

2.1.3. Ferromagnetism

Ferromagnetic materials exhibit parallel alignment of moments resulting in large net magnetization below the Curie temperature even in the absence of a magnetic field. But over the Curie temperature ferromagnetic materials become paramagnetic. The elements Fe, Ni, and Co and many of their alloys are typical ferromagnetic materials **[48].** Above the Curie point, the ferromagnetic material becomes paramagnetic, the susceptibility of which decreases with temperature. If the reciprocal susceptibility, $1/\chi$ is plotted against T, the curve obeys the Curie Weiss Law,

$$1/\chi = 1/[C(T-T_C)] \quad (2.4)$$

Where, C = Curie weiss constant, Tc = Curie point

2.1.4. Ferrimagnetism

The magnetic structure is composed of two magnetic sub-lattices (called A and B) separated by oxygens. The exchange interactions are mediated by the oxygen anions. When this happens, the interactions are called indirect or super exchange interactions. The strongest super exchange interactions result in an antiparallel alignment of spins between the A and B sub-lattice. In ferrimagnets, the magnetic moments of the A and B sub-lattices are not equal and result in a net magnetic moment. Ferrimagnetism is therefore similar to ferromagnetism.

It exhibits all the hallmarks of ferromagnetic behavior- spontaneous magnetization, Curie temperatures, hysteresis, and remanence. However, Ferro and ferrimagnets have very different magnetic ordering **[48].**

2.1.5. Anti-ferromagnetism

If the A and B sub-lattice moments are exactly equal but opposite, the net moment is zero. This type of magnetic ordering is called anti-ferromagnetism **[48].** Antiferromagnetic susceptibility of the Curie-Weiss law at high temperatures with negative θ as,

$$\chi = C/(T+\theta) \tag{2.5}$$

where θ = Experimentally determined constant

$$\text{Also } \chi = C/(T-T_N) \tag{2.6}$$

where T_N= Néel temperature

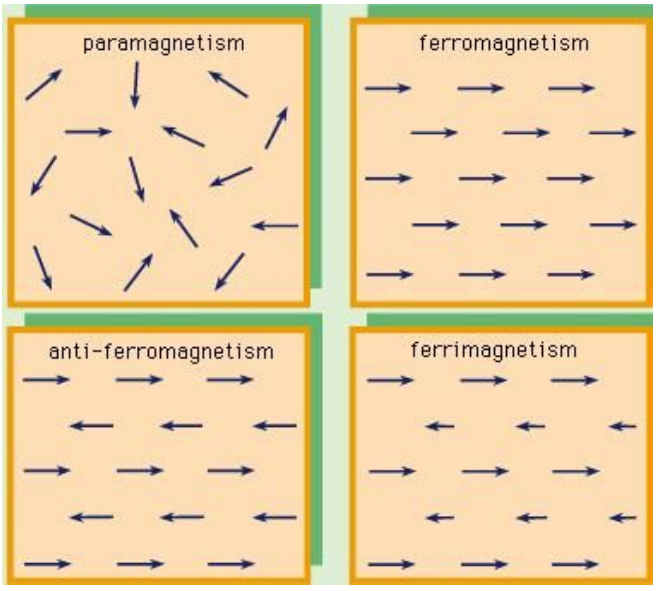

Figure 2.1: Magnetic arrangements of ferromagnetic, anti-ferromagnetic and ferrimagnetic materials, retrieved from **[49]**

2.2. Hysteresis loop

For unmagnetized bulk material, there is a zero magnetic moment. When the materials are subjected to an external magnetic field, this extreme situation corresponds respectively to the random orientation of domain complete alignment is one direction with the elimination of the domain walls. If we start with the applied magnetic field, the bulk material will be progressively magnetized by the domain dynamics. The magnetization of the sample will follow the path as shown in the dotted line in the Fig. 2.2. Firstly, the lower section is in the initial susceptibility region and is characterized by reversible domain wall movement and rotation. The shape of the hysteresis curve is an important factor for discussing magnetic materials. When a magnetic material is magnetized in one direction in the influence of the external magnetic field, it will track back to zero after the applied magnetic field is keep away. In addition, if an opposite magnetic field is applied to these materials, its magnetization will trace out a loop is known as a hysteresis loop **[10]**. In Fig. 2.2 shows the B-H curve which following the path of a-b-c-d-e-f-a as the alternating magnetic is applied.

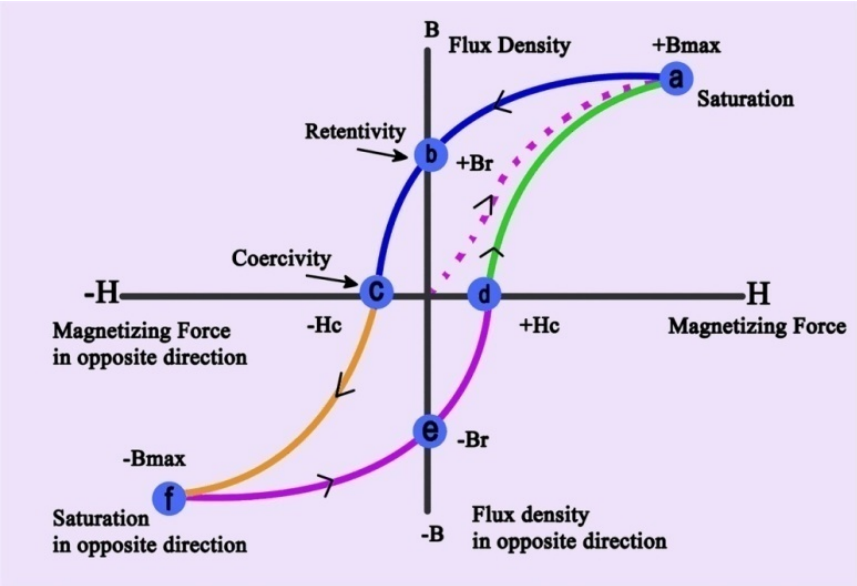

Figure 2.2: Hysteresis loop, retrieved from **[50]**

The shape and size of the hysteresis loop heavily depends on the magnetic properties of magnetic materials. For particular applications need particular magnetic materials. By using the hysteresis loop, one can get some specific information about the magnetic properties of materials, such as magnetization, coercive force, residual magnetism, permeability, and reluctance.

2.2.1. M-H Curve

In ferromagnetic materials, M is typically 10^4 larger than would appear otherwise. The susceptibility in order materials depends not just on temperature but also on H, which give rise to the characteristic sigmoidal shape of the M-H curve, with M approaching a saturation value at large values of H. Furthermore, in ferromagnetic and ferrimagnetic materials one often exhibits hysteresis which is irreversibility in the magnetization process that is related to the pinning of magnetic domain walls at impurities or grain boundaries within the materials, as well as to intrinsic effect such as the magnetic anisotropy of the crystallite lattice. This gives rise to open M-H curves, called hysteresis loop. The shape of these loops are determined in part by particle size: in large particles, there is a multiple domain ground state which leads to a narrow hysterias loop since a fake relatively lattice field energy to make the domain walls move; while in smaller particles there is a single domain ground state which leads to a broad hysterias loop. At an even smaller size of the order of tens of nm or less. One can see the superparamagnetic, where the magnetic moment of the particle as a whole is free to fluctuate in response to thermal energy, while the individual atomic moments maintain their order state relative to others. This leads to the hysteretic; but still, sigmoidal M-H curve shown in Fig. 2.3 **[48].**

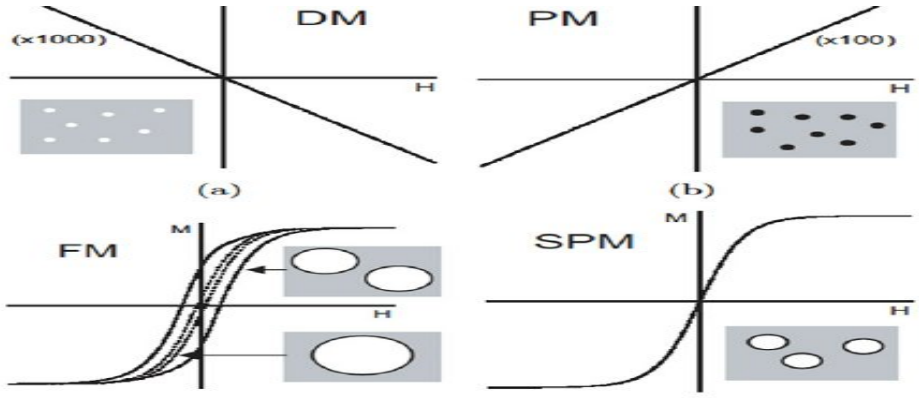

Figure 2.3: Graphical presentation of interaction of the magnetic moment M with external field H and M-H curve for Diamagnetic, paramagnetic, ferromagnetic and superparamagnetic materials, retrieve from **[51].**

In Fig. 2.3 shows in ferromagnetic materials, in absence of external magnetic field magnetic moment M aligned parallel. Hence the hysteresis loop is observed with remanence and coercivity. On the other hand, superparamagnetic materials show a similar pattern but with the absence of hysteresis loop, remanence, and coercivity. For the biomedical application especially on hyperthermia therapy need superparamagnetic material. Those materials show some special properties of hysteresis loop like zero retentivity and zero coercivity. The M-H curve for the ferromagnetic and superparamagnetic nanoparticle is represented below. There are a large number of iron oxide compounds like γ- Fe_2O_3, γ- Fe_2O_4 shows super paramagnetic behavior.

2.3. Magnetic nanoparticles and single domain particles

The nanoscale magnetic materials have gained the attention of a lot to the researcher over the last decade not only for the business and technological reasons, but also for fundamental research points of view. For finding biomedical applications like improving the quality of

magnetic resonance imaging (MRI), hyperthermia treatment for malignant cells, site- specific drug delivery, etc. nanoscale magnetic materials are used over the last decade **[52].**

Pierre Weiss et. al first explain the behavior of the hysteresis of ferromagnetic bulk materials by using the concept of domains. Ferromagnetic materials are consisting of domains, which are separated by domains wall **[53]**. This domain walls tries to minimize the net energy of the system. The magnetostatic energy and domain wall energy increase proportionally to the volume and surface respectively. When the particle size lower than the critical size, the surface area is increased as well the domain energy so it became unfavorable for creating domains. In this situation, the single uniform domain is formed and the system behaves like a small permanent magnet. The size of the single-domain particle depends on the material and contributions from different anisotropy energy terms **[54]**.

Stoner and Wohlfarth are describing the model of magnetization for single-domain particles. They assumed noninteracting particles with uniaxial anisotropy in which spins are parallel and rotate at the union. Furthermore, at any finite temperature, the thermal activation can overcome the anisotropy energy barrier leading to switching of the particle moment. This relaxation process was first proposed by Neel in 1949 and further developed by Brown **[55-56].** This function is commonly used to fit the experimental magnetization curve of nanoparticles and to determine the size of the crystal and its specific magnetization. The characteristics features of superparamagnetic nanoparticles are their response to the magnetic field, where there are no remanent magnetization and a very high field of saturation magnetization **[57].**

2.4 Synthesis methods of nanoparticles

Nanoparticles growth mechanism is a complex process and depends on many conditions (temperature, viscosity, the concentration of medium). Conditions, determinant of nanoparticle growth, may change depending on the method of preparation of nanoparticles.

2.4.1 Chemical co-precipitation

Chemical co-precipitation method may be the most promising one because of its simplicity and productivity. It is widely used for biomedical applications because of ease of implementation and the need for less hazardous materials and procedures **[58].**

There are two main methods for the synthesis in the solution of magnetic spherical particles in the nanometer range. In the first, ferrous hydroxide suspensions are partially oxidized with different oxidizing agents. Spherical magnetic particles of narrow size distribution with mean diameters between 30 and 100 nm can be obtained from Fe (ii) salt, a base and a mild oxidant (nitrate ions) **[59]** the other method consists in aging stoichiometric mixtures of ferrous and ferric hydroxides in aqueous media, yielding spherical magnetic particles homogeneous in size **[60].** It has been shown that by adjusting the pH and the ionic strength of the precipitation medium, it is possible to control the mean size of the particles over one order of magnitude (from 15 to 2 nm). The size decreases as the pH and the ionic strength in the medium increases **[61].** The difficulty in preparing Fe_3O_4 magnetic nanoparticles by chemical co-precipitation is the tendency of agglomeration of particles because of extremely small particle size leading to great specific surface area and high surface energy, consideration of the effect of alkali, emulsifier and reaction temperature are the decision making factors of the final product **[58].**

2.4.2 Sol-gel

Sol-gel method is very convenient for making metal oxides via the hydrolysis of reactive metal precursors, as a colloidal sol, usually alkoxide (CH_3O^-) in an alcoholic solution, resulting in the corresponding hydroxide, as the technology makes it possible to form widely different morphologies and particle sizes with modest means. Condensation of hydroxide molecules by the elimination of water leads to the formation of a network of metal hydroxide. When all hydroxide species are linked in one network- like structure, gelatins is achieved and a dense porous gel is obtained. Removal of the solvents and appropriate drying of the gel results in an ultra-fine powder of the metal hydroxide. When drying is achieved by evaporation under normal conditions, the gel network shrinks and the hydroxide product obtained is referred to as xerogel **[62].** Growing the primary sol particles and aggregating them to the gel is often controlled with the pH of the solution. Sol-gel synthesis of inorganic oxides involves the gelatin of aqueous or non-aqueous precursors with concentration corresponding to the stoichiometry of the final product, followed by slow evaporation and calcination, to yield the desired product **[63].**

2.4.3 Microemulsion

Microemulsion is a thermodynamically stable isotropic dispersion of two immiscible liquids, where the micro-domain of either or both liquids is stabilized by an interfacial film of surfactant molecules **[64].** In water-in-oil microemulsions, the aqueous phase is dispersed as micro droplets (typically 1–50 nm in diameter) surrounded by a monolayer of surfactant molecules in the continuous hydrocarbon phase. The size of the reverse micelle is determined by the molar ratio of water to surfactant **[65].** By mixing two identical water-in-oil microemulsions containing the desired reactants, the micro-droplets will continuously collide, coalesce, and break again, and finally precipitate forms in the micelles **[66].** By the

addition of solvent, such as acetone or ethanol, to the microemulsions, the precipitate can be extracted by filtering or centrifuging the mixture. In this sense, a microemulsion can be used as a nano reactor for the formation of nanoparticles.

2.4.4. Hydrothermal synthesis

Under hydrothermal conditions, a broad range of nanostructured materials can be formed. A mixture, consisting of $FeCl_3$, ethylene glycol, sodium acetate, and polyethylene glycol, was stirred vigorously to form a clear solution, then sealed in a Teflon-lined stainless steel autoclave, and heated to and maintained at 200 ^{O}C for 8–72 h. In this way, monodisperse ferrite spheres were obtained with tunable sizes in the range of 200–80 nm **[67].**

2.5. Spinel structure nanoparticles

Cobalt ferrite nanoparticle has the spinel structure with general formula MFe_2O_4 [M = Mn, Co, Ni, Zn, Mg, etc], which has remarkable properties **[32].** The spinel structure belongs to space group Fd3m. The cubic unit cell is formed by 56 atoms, 32 oxygen anions distributed in a cubic close packed structure, and 24 cations occupying 8 of the 64 available tetrahedral sites (A-sites) and 16 of the 32 available octahedral sites (B-sites). Depending on cation distribution, a spinel can be normal, inverse, or partially inverse. Fig. 2.4 shows a normal spinel structure, the 8 bivalent cations are all located in tetrahedral sites and the 16 trivalent cations are all located in octahedral sites, while, in an inverse-spinel structure, the 8 bivalent cations occupy 8 octahedral sites and the 16 trivalent cations are distributed between 8 tetrahedral and 8 octahedral sites **[68].**

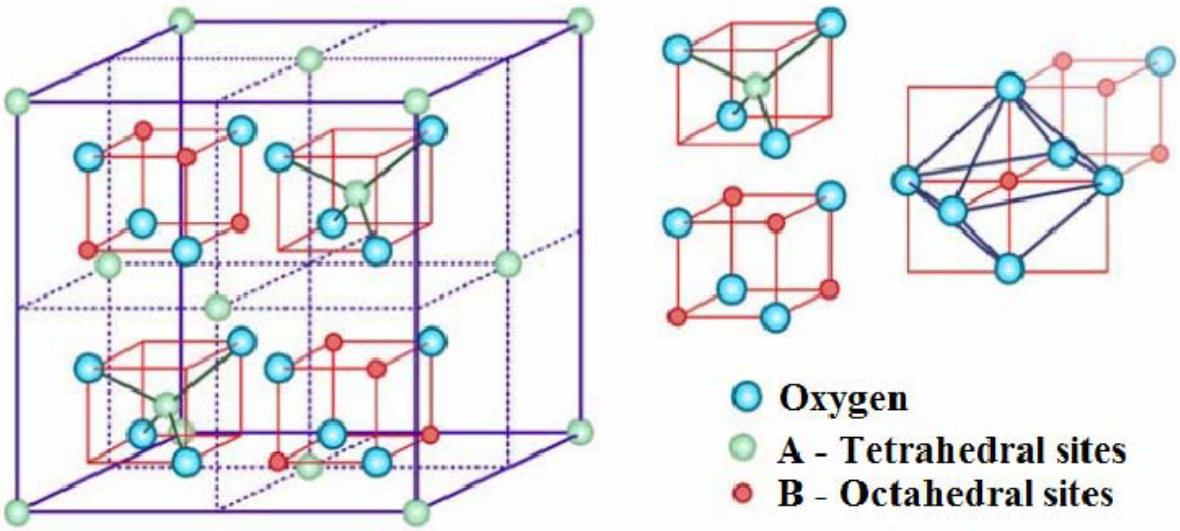

Figure 2.4: The magnetite spinel structure, retrieved from **[69].**

2.6 Surface coating

The surface coating is a very interesting features of nanoparticles for biocompatibility and nontoxicity. For instance, contrast agents for Magnetic Resonance Imaging (MRI), like super-paramagnetic iron oxide (SPIO) NPs or paramagnetic gadolinium labeled NPs are often coated with polymers to increase their solubility and biocompatibility **[70].**

2.6.1 Folate chitosan as surface coating agent

Chitosan NPs are emerging as a drug delivery system due to its favorable characteristic features such as size, biocompatibility, high drug encapsulation efficiency, controlled drug release potential and long circulating half-life. Furthermore, due to the presence of primary amino groups, CS-NPs are easily modified by various ligands, including folate, epidermal growth receptor and polypeptides. Thus, modifications of CS-NPs with ligands specific for receptors on tumor cells may enhance the specificity of the drugs delivered to the tumor cells. Folate is an extensively studied ligand as it is stable, inexpensive and has low

immunogenicity. Furthermore, the expression of the folate receptor (FR) is higher in human cancer cells, including HeLa and MCF-7 cells, than in normal cells. FA-CS-NPs loaded with anticancer agents produced enhanced intracellular accumulation of therapeutic agents **[33]**. Fig. 2.5 shows the schematic process of folate chitosan conjugate.

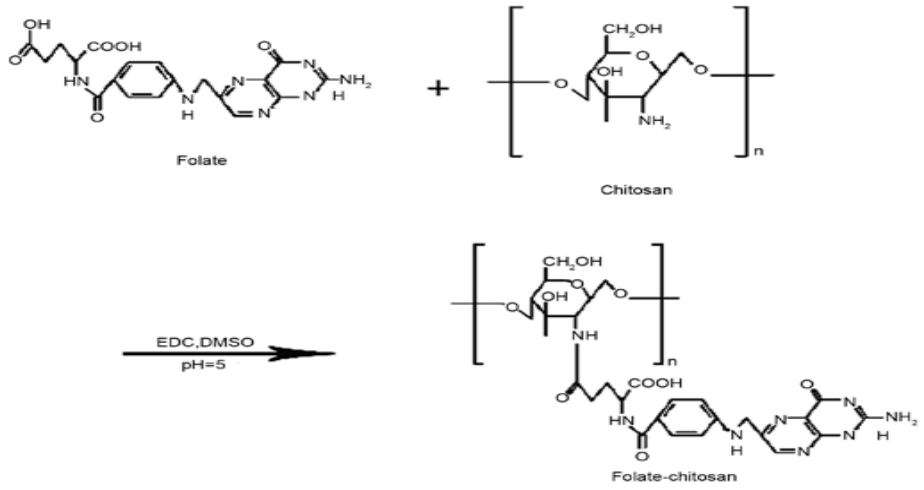

Figure 2.5: Schematic process of folate chitosan conjugate, retrieved from **[71]**

2.7. Hyperthermia

Hyperthermia (HT, thermal therapy, thermotherapy) is thought to be one of the cancer therapies amongst surgery, radiation therapy, chemotherapy, gene, and immunotherapy. It is a natural or artificial phenomenon that involves increasing the temperature of the body or a particular region of it over the threshold temperature set at a particular moment by the thermoregulation system of an organism **[71].** This is a very promising approach and in this thesis study, our concentration has been given to find out the efficiency of this method by using iron oxide nanoparticles.

2.7.1 Different methods of hyperthermia

There appear to be three main clinical methods of high temperature application depending on location, depth, and staging of the tumor. They are as follows:

2.7.1.1. Local hyperthermia

Local hyperthermia is dedicated to rather small tumors (≤3 cm up to 5–6 cm in the longest diameter) located superficially or within an accessible body cavity such as the rectum or esophagus **[72].** Superficial, interstitial, intraluminal or intracavitary applicators can be applied, and most commonly, microwaves, radio waves or ultrasound are used to deliver heat to the tumors. Local techniques enable heating of small cancerous areas with sufficient sparing of normal tissues. Tumors located in the skin or just below can be heated with superficial applicators or antennas emitting a particular type of energy, placed directly in or near the area of interest such as radio waves, microwaves, ultrasound waves, and other forms of energy. When ultrasound is used, the technique is called high intensity focused ultrasound, or HIFU, sometimes also referred to as just focused ultrasound **[73].**

Among interstitial hyperthermia techniques, radiofrequency ablation should be noted as well. Radiofrequency ablation (RFA) is probably the most commonly used type of thermal ablation. It uses high-energy radio waves for treatment **[74].** Thermoablation uses radio waves to raise the temperature within the tumor to over 50 °C for more than 4 to 6 minutes and causes vascular stasis, cellular coagulation, and tissue necrosis. This method is able to destroy small focal tumors located within the liver, lung, kidney or bones. RFA is most often used to treat tumors that cannot be removed with surgery or for patients who are not able to go through the stresses of surgery **[75].** It can usually be done as an outpatient. RFA may be repeated for tumors that come back or start to grow. It can also be added to other treatments

like surgery, radiation therapy, chemotherapy, hepatic arterial infusion therapy, alcohol ablation, or chemo immobilization **[76].**

2.7.1.2. Regional hyperthermia

Regional or part-body hyperthermia is a term for heating large parts of the body, e.g. abdominal cavity, particular organs, or limbs. Most often it is devoted to treating advanced tumors situated in the major and minor pelvis, abdomen (cervical, prostate, bladder, colorectal, and ovarian carcinomas) or thighs (soft tissue sarcomas). Three main approaches can be listed: deep-seated tumors heated with external applicators, limbs or organs heated by means of thermal perfusion, and continuous hyperthermic peritoneal perfusion **[77].**

In the case of the deep-seated heating method, the treatment uses devices that are placed on the surface of the organ or body cavity and produce high energy waves directed at a certain area. These devices give off radiofrequency or microwave energy to heat the area being treated. In the thermal perfusion approach, the blood supply to a part of the body is isolated from the rest of the circulation. The blood in that part of the body is pumped into a heating device and then pumped back into the area to heat it. Chemotherapy can be pumped in at the same time. This technique is being studied as a treatment for certain cancers in the arms or legs, such as sarcomas and melanomas. Continuous hyperthermic peritoneal perfusion (CHPP) technique can be used along with surgery to treat cancers in the peritoneum (the space in the body that contains the intestines and other digestive organs). During surgery, heated chemotherapy drugs are circulated through the peritoneal cavity. This is also known as hyperthermic intraperitoneal chemotherapy (HIPEC). In studies, this has seemed helpful in treating certain types of cancer, but it isn't yet clear if it is better than other types of treatments.

2.7.1.3. Whole-body hyperthermia

Whole-body hyperthermia (WBH) is a chance for patients with a metastatic disease such as melanoma, soft tissue sarcoma or ovarian cancer. Disseminated cancerous cells are thought to be destroyed or sensitized to drugs with high temperature of the whole organism. To achieve that aim (approximately 41.8–42.2 °C) thermal chambers, hot water blankets or infrared radiators are used, concomitantly with the prevention of temperature loss and electrolyte fluids restoration. Depending on the subtype of WBH, patients demand general anesthesia or deep sedation while heated up to 42.0 °C for 60 minutes (extreme WBH) or to 39.5–41.0 °C for 3 to 4 hours (moderate WBH), respectively. WBH offers the most homogeneous thermal distribution. On the other hand, it is related to the greatest probability of complications (thermal stress to the heart, lungs, liver or brain).

2.7.2. Magnetic particle hyperthermia (MPH)

Magnetic particle hyperthermia (MPH) with magnetic materials has emerged as one of the promising cancer modalities either alone or in combination with chemo/radiotherapy in the past few decades **[78].** In MPH therapy, magnetic nanoparticles were used to heat the specific region of the body or tissue via absorption of radio/micro frequency when subjected to an alternating current (AC) magnetic field **[79].** Clinical applications of MPH required that nanoparticles should possess a large specific absorption rate (SAR), high biocompatibility, and good chemical stability in a physiological tolerable range of magnetic fields and amplitudes **[80].**

In magnetic particle hyperthermia (MPH) one deposits magnetic media in tumor tissue with subsequent heating by means of an external alternating magnetic field. Former approaches dealt with electro conductive or ferromagnetic implants; recent studies are applying magnetic nanoparticles (MNP) as their heat generation potential appears beneficial and they provide

the opportunity of direct tumor targeting through blood circulation. Besides a localized heat generation, the application of MNP offers the possibility of a self-limitation of the temperature enhancement by using a magnetic material with a suitable Curie temperature **[81].** However, for biomedical applications, the vast number of known magnetic materials is strongly restricted by the demand of biocompatibility (e.g. non-toxicity, sufficient chemical stability in the bio-environment, appropriate circulation time in blood and finally harmless biodegradability). Though there are a few suggestions in the literature to use metallic iron particles, several spinel ferrites as well as special magnetic alloys for MPH, the majority of investigations concentrate on magnetic iron oxides Fe_3O_4 (magnetite) and γ -Fe_2O_3 (maghemite) which have been proven to be well tolerated by the human body **[82].**

Chapter 3: Sample Preparation & Experimental Procedures

3.1 Sample preparation

3.1.1 Synthesis of $CoFe_2O_4$ nanoparticles

There are a lot of synthesis strategies for preparing cobalt ferrite magnetic nanoparticles but chemical co-precipitation method is a prominent one. In this method, the particle size depends on pH, salt concentration, temperature, stirring speed etc. Simplicity and low cost make this method more convenient. In this method, we can control the production of ferrite particle, and its particle size distribution can be controlled.

Cobalt ferrite nanoparticle was synthesized by co-precipitation method described by Hoque et al. **[37].** As a raw sample cobalt chloride hexahydrated ($CoCl_2$. $6H_2O$), and ferric chloride hexahydrated ($FeCl_3$. $6H_2O$), and solium hydroxide (NaOH) has been taken.

At first, those materials were weighted according to the molar ratio and then making a solution using deionized water. The entire sample has taken in a magnetic starrier to dissolve the salt properly. Then the reactant solutions were mixed together. 8 M NaOH solution was also prepared in another beaker. NaOH was added drop-wise in the beaker and the speed of the magnetic stirrer was gradually increased. Deionized water was used as a solvent in order to avoid the production of impurities in the final product. NaOH was added to control the pH of the solution. Using a pH meter, the pH of the solution was kept at 11-13. The reactant was constantly stirred using a magnetic stirrer until a pH level of 10-12 was reached. Then the temperature was applied to heat the solution. The temperature was increased from room temperature to 60 °C within 1 h after that 60 ^{o}C to 80 ^{o}C within 1 h. Then the stirring process stopped and the sample was left to precipitate and cool to room temperature for one night. The particles were settled down at the bottom of the beakers. In this final product an enormous amount of NaOH remained which should be washed away from the final product. The solution was centrifuged at 13000 rpm for 20 minutes for 10 times with deionized water to remove NaOH. After the removal of NaOH from the mixture, the mixture was heated at 80

^{o}C for 72 h. This solid phase is formed via a chemical process involving the formation of an intermediate phase. The sample was hand milled for 3 h to remove that phase and preserved this powder sample in a vial.

The reaction that take place during the synthesis of cobalt ferrite nanoparticles are –

$CoCl_2.6H_2O + 2NaOH = Co(OH)_2 + 2NaCl + 6H_2O$

$2FeCl_3 + 6NaOH = 2Fe(OH)_3 + 6NaCl$

$Co(OH)_2 + 2Fe(OH)_3 = CoFe_2O_4 + 4H_2O$

Overall Reaction: $CoCl_2.6H_2O + 8NaOH + 2FeCl_3 = CoFe_2O_4 + 8NaCl + 10H_2O$

Fig. 3.1 shows the flow chart of the experimental procedure to synthesized $CoFe_2O_4$ nanoparticles and Fig. 3.2 shows the image of synthesized $CoFe_2O_4$ nanoparticle.

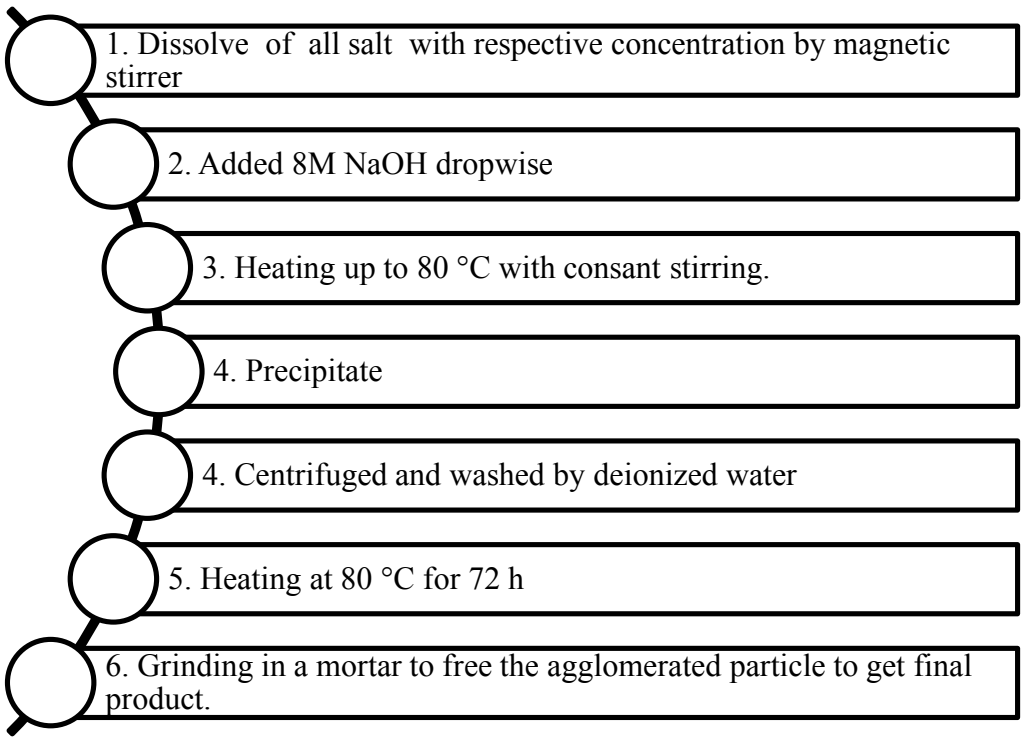

Figure 3.1: Flow chart for the synthesis of $CoFe_2O_4$ nanoparticles

Figure 3.2: Synthesized cobalt ferrite nanoparticle's attraction to magnet

3.1.2 Preparation of folate chitosan (FA-CS) conjugate

Li et al **[83]** and Alupei **[84]** synthesized the folate chitosan (FA-CS) conjugated with some modification. There were two steps for the preparation of folate chitosan. In the first step folic acid was reacted with N-hydroxysuccinimide to form N-hydroxysuccinimide ester of folic acid and in the second step this ester was reacted with chitosan to prepare folate conjugated chitosan.

3.1.2.1 Preparation of N-hydroxysuccinimide ester of folic acid (NH-FA)

In this process 60 ml anhydrous dimethyl sulfoxide (DMSO) and 1.5 ml triethylamine (TEA) were mixed together. Then 3 g of folic acid was dissolved in the mixture. This was followed by the addition of 2.82 g dicyclohexylcarbodiimide (DCC) and 1.56 g N-hydroxysuccinimide (NHS). The mixture was stirred for 12 h at room temperature; the insoluble side product dicyclohexylurea was removed by filtration. The filtrate was then poured into an ice-cold anhydrous ether solution containing 30% acetone, centrifuge, and then washed with deionized water. Finally, NHS-FA a delicate light yellow solid powder was obtained by

drying at room temperature. Fig. 3.3 shows the reaction mechanism of activation of γ-COOH group of folic acid.

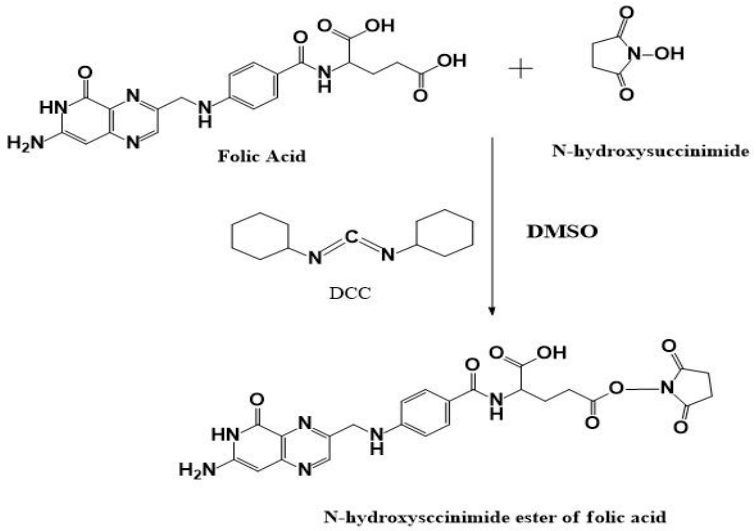

Figure 3.3: Reaction mechanism of activation of γ-COOH group of folic acid, retrieved from **[84].**

3.1.2.2 Preparation of folate conjugated chitosan (FA-CS)

1.5 g of the prepared ester (NH-FA) was dissolved in 150 ml dimethyl sulfoxide (DMSO). The adequate dissolution process was performed in an ultra-sonication bath. Thereafter 1.0 g of chitosan was added into the DMSO containing NH-FA, and stirred for 4 h at 60 °C. The reactant was deposited after centrifugation (6000 rpm, 15 min) at room temperature, and free NH-FA was washed out by DMSO. Finally, the product was washed with deionized water to remove residual DMSO. Finally, yellow colored FA–CS products were collected and freeze-dried at -50 ^{o}C for 24 h. Fig. 3.4 shows the reaction mechanism of *N*-hydroxysuccinimide ester of folic acid with chitosan and Fig 3.5 shows the image of prepared folate chitosan (FA-CS) conjugate.

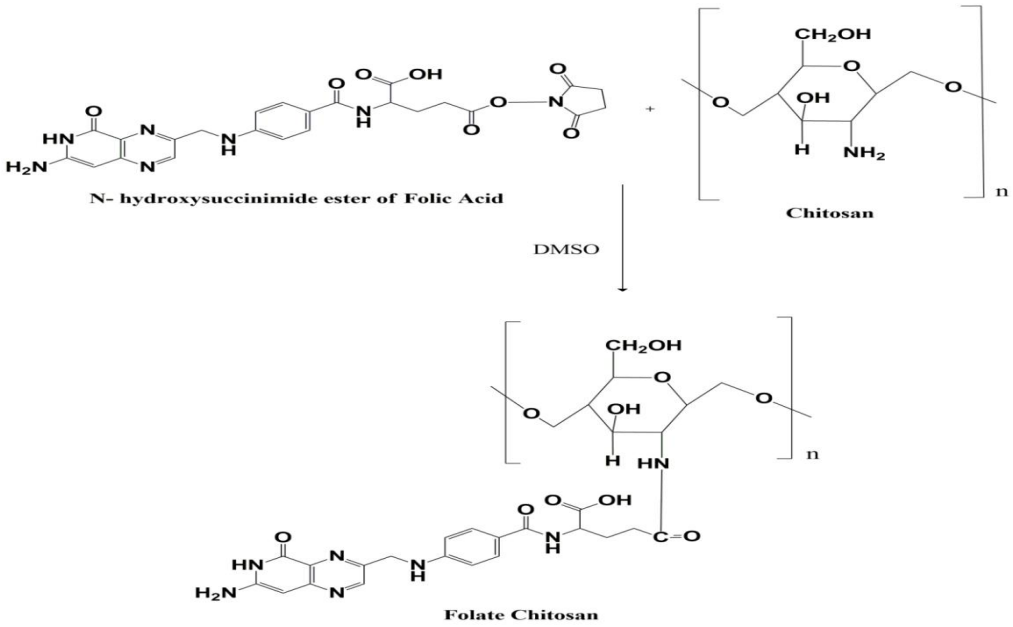

Figure 3.4: Reaction mechanism of *N*-hydroxysuccinimide ester of folic acid with chitosan, retrieved from **[84]**

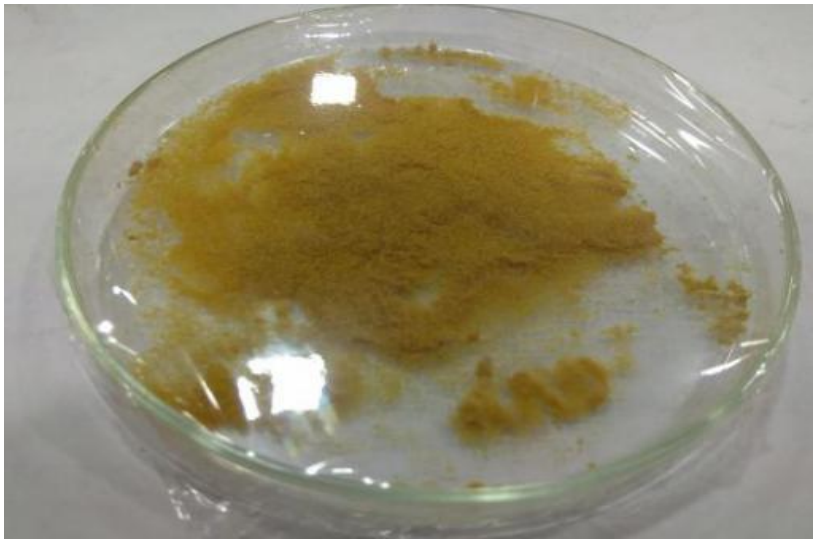

Figure 3.5: Folate conjugated chitosan (FA-CS)

3.1.3 Coating of cobalt ferrite nanoparticle with folate chitosan

Coating of iron oxide (Fe_3O_4) nanoparticles by folate conjugated chitosan were followed by the method described by Islam et al. **[85]** and Kuo et al. **[86]** with some modification. According to the procedure, 0.5 gm folic acid conjugated chitosan was dissolved in 50 ml 1% (V/V) acetic acid. Then 1.0 g as dried $CoFe_2O_4$ nanoparticle was taken in a falcon tube and 5 ml dissolved folic conjugated chitosan solution was added, vortexed 10 minutes to mix and the mixture sonicated in an ultra-sonication bath for 30 min for the first time. Then 12.5 ml (1 mg/ml) sodium tripolyphosphate (TPP) solution was added into the solution as a cross linker to enhance colloidal stability. After that the sample was vortexed 10 minutes and sonicated 10 minutes below 40 °C temperature until it was fully coated. Then the 20 mg/ml suspension of fotate chitosan-coated $CoFe_2O_4$ nanoparticle was obtained. After that using deionized water 0.5 mg/ml, 1 mg/ml, 2 mg/ml, 4 mg/ml and 6 mg/ml sample were prepared which are shown in Fig. 3.6.

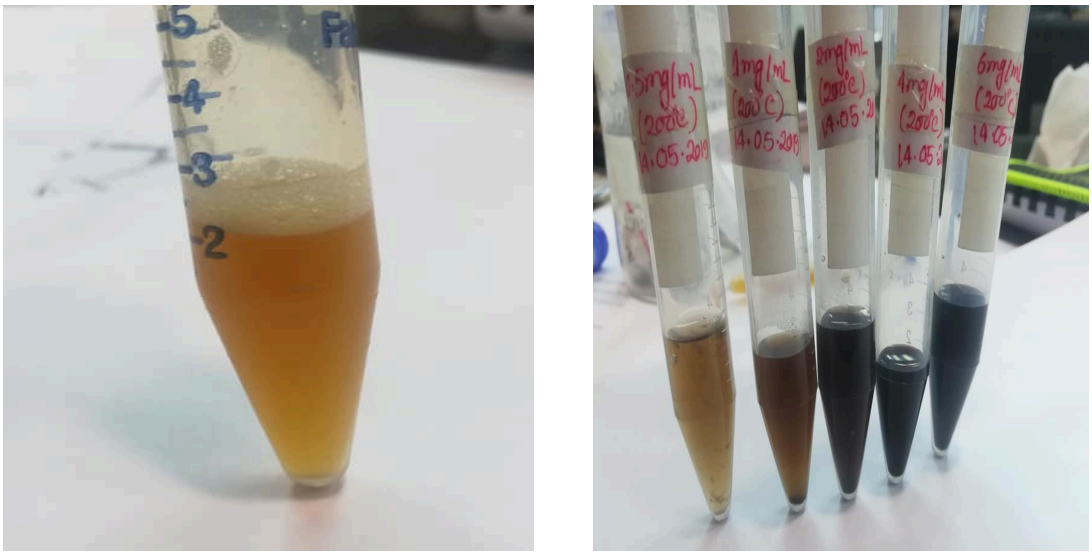

(a) **(b)**

Figure 3.6: (a) Dissolve folate conjugated chitosan, **(b)** folate chitosan coated cobalt ferrite nanoparticles for 0.5 mg/ml, 1 mg/ml, 2 mg/ml, 4 mg/ml and 6 mg/ml.

3.2 Materials characterizations

3.2.1 X-Ray diffraction

X-ray diffraction (XRD) is the most precise technique for studying the crystal structure of solids, generally requiring no elaborate sample preparation and is essentially non-destructive When X-rays interact with a crystalline substance (Phase), one gets a diffraction pattern. An electron in an alternating electromagnetic field will oscillate with the same frequency as the field. When an X-ray beam hits an atom, the electrons around the atom start to oscillate with the same frequency as the incoming beam. In almost all directions we will have destructive interference, that is, the combining waves are out of phase and there is no resultant energy leaving the solid sample. XRD is based on the constructive interference of monochromatic X-Rays and a crystalline sample. The monochromatic X-rays are generated by a cathode ray tube, filtered to produce monochromatic radiation, collimated to concentrate them, and directed toward the sample **[87].** Let us consider an incident X-ray beam interacting with the atoms arranged periodically as shown in two dimensions in Fig. 3.7.

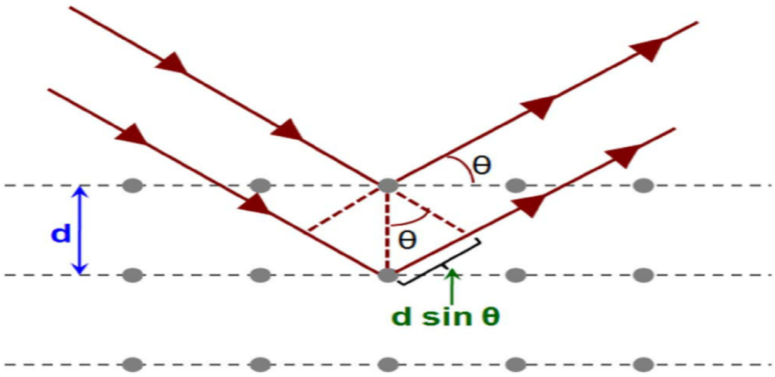

Figure 3.7: Schematic diagram of Bragg's diffraction pattern, retrieved from **[88].**

The interaction of the incident rays with the sample produces constructive interferences (and a diffracted ray), when conditions satisfy Bragg's law. In accordance with Bragg's law when X-rays hit an atom, they make the electronic cloud move as does any electromagnetic wave.

The interference is constructive when the phase shift is a multiple of 2π; this condition can be expressed by Bragg's law nλ = 2d sinθ **[89],** where, d is the distance between the crystal planes and n is an integer, λ is the wavelength of the x-ray. From different peaks in XRD spectra, the phase identification can be possible in terms of different sets of d spacing for a certain material. From the law, we find that the diffraction is only possible when λ< 2d **[90].**

Since the crystal pattern repeats in three dimensions, forming a three-dimensional diffraction grating, three integers, denoted h, k, l are required to describe the order of the diffracted waves. These three integers, the Miller indices used in crystallography, denote the orientation of the reflecting sheets with respect to the unit cell and the path difference in units of wavelength between identical reflecting sheets.

The lattice parameter for each peak of each sample was calculated by using the formula (for cubic spinel structure)

$$a = d\sqrt{h^2 + k^2 + l^2} \tag{1}$$

where h, k and l are the indices of the crystal planes. To determine the exact lattice parameter for each sample, Nelsion-Riley method was used. The Nelsion-Riley Function F(θ) is given as

$$F(\theta) = \frac{1}{2}[(Cos^2\theta / Sin\theta) + (Cos^2\theta / \theta)] \tag{2}$$

where θ is the Bragg's angle. Now drawing the graph of 'a' vs. F (θ) and using linear fitting of those points will give us the lattice parameter 'a_o'. This value of 'a_o' at F (θ) = 0° or θ = 90°. These 'a_o's are calculated with an error estimated to be ± 0.0001 Å.

The crystal size of the nanoparticle can be determined by using Scherrer's formula which is expressed as

$$D = K\lambda / (\beta \cos\theta) \tag{3}$$

where, D= Grain size (nm), K= Scherrer constant. K varies from 0.68 to 2.08. Value of K is 0.94 for spherical crystallites with cubic symmetry, λ= X-ray wavelength, which is 1.54178 Å for Cu- Kα radiation, β= FWHM (Full Width at Half Maximum) of XRD peak, θ = is the Bragg angle (in degrees). In the present work a Philips X'pert pro XRD (PW3040) at the materials science division in Bangladesh Atomic Energy Commission (Fig. 3.8) was used to study the crystalline phases of the prepared samples. It uses Cu target for X-ray production and uses nickel filter to yield monochromatic Cu- Kα radiation (λ = 1.54 Å). For all the measurements of nickel ferrite, powder specimens of about 20 mg were exposed to Cu Kα radiation with a primary beam power of 40 kV and 30 mA and with a sampling pitch of 0.02° and time for each step of data collection was 1 second. A scan was taken from 15° to 75° to get possible fundamental peaks of the sample. The programmable divergence slit was used to control the irradiated beam area and the programmable receiving slit was used to control the output intensity. Powder diffraction data were analyzed using the software X'pert High score. An instrumental broadening of the system was determined from θ to 2θ scan of standard Silicon. At (110) reflection's position of the peak the value of instrumental broadening was found to be 0.07°. This value of instrumental broadening was subtracted from the pattern.

Figure 3.8: Philips X'pert pro XRD (PW3040) at materials science division in Bangladesh Atomic Energy Commission.

3.2.2 Transmission electron microscopy (TEM)

Transmission electron microscopy (TEM) is a microscopy technique in which a beam of electron is transmitted through an ultra-thin specimen interacting with the specimen as it passes through. An image is formed from the interaction of the electrons transmitted through the specimen; the image is magnified and focused onto an imaging device, such as a fluorescent screen, on a layer of photographic film, or to be detected by a sensor such as a CCD camera to examine fine detail even as small as a single column of atoms, which is thousands of times smaller than the smallest resolvable object in a light microscope. TEM consists of an electron gun (virtual source), which produces a stream of monochromatic electrons. This stream is focused to a small, thin, coherent beam by the use of condenser lenses 1 and 2. The first lens largely determines the "spot size"; the general size range of the final spot that strikes the sample. The second lens changes the size of the spot on the sample, changing it from a wide dispersed spot to a pinpoint beam. The beam is restricted by the optic axis, the dotted line down the center). The beam strikes at the specimen and parts of it are transmitted. This transmitted portion is focused by the objective lens into an image. The Objective aperture enhances contrast by blocking out high-angle diffracted electrons, the Selected Area aperture enables the user to examine the periodic diffraction of electrons by ordered arrangements of atoms in the sample. The image is passed down the column through the intermediate and projector lenses, being enlarged all the way. The image strikes the phosphor image screen and light is generated, allowing the user to see the image. The darker areas of the image represent those areas of the sample that fewer electrons were transmitted through (they are thicker or denser). The lighter areas of the image represent those areas of the sample that more electrons were transmitted through (they are thinner or less dense) **[91].**

In the present work, a thermoscientific TEM (Talos) at the materials science division in Bangladesh Atomic Energy Commission (Fig. 3.9) was used to observe the micrograph of the

prepared samples. To take the TEM micrograph, the samples were prepared according to the Hoque et al **[37].** At first the coated and uncoated samples were taken in an apendrop and mix with methanol. Then vortex and sonicate the samples to disperse the sample and remove the agglomeration. Therefore, using the pipette (1-20 μL) drop cost the sample on the cupper grid.

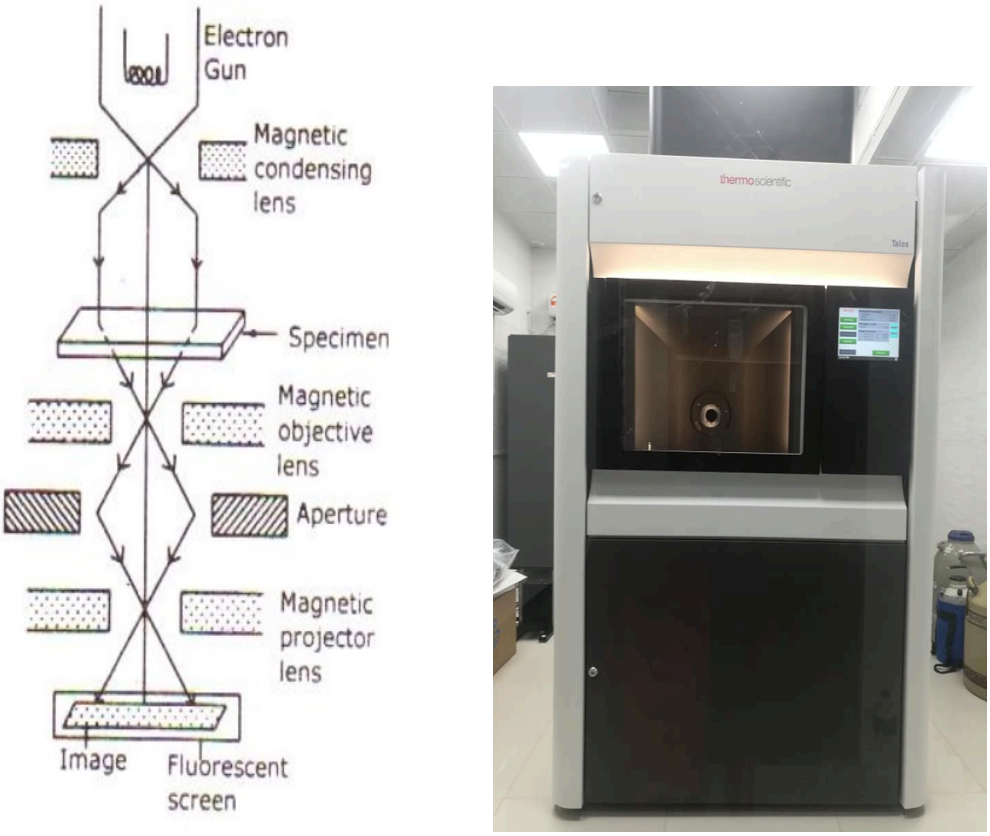

(a) **(b)**

Figure 3.9: **(a)** Schematic diagram of transmission electron microscope, retrieved from **[91], (b)** Thermo scientific Talos at materials science division in Bangladesh Atomic Energy Commission.

3.2.3 Vibrating sample magnetometer (VSM)

The principle of VSM is shown in Fig. 3.10. VSM is the measurement of electromotive force induces by magnetic sample when it is vibrating at a constant frequency in the presence of a static and uniform magnetic field. The VSM was first designed by Simon Foner, in 1959 at the Lincoln laboratories **[92].** Since then many transformations and variants have been seen, but the basic underlying principle remains the same induction of emf by Faraday's law. All the VSM studies, involves the measurement of the voltage induced in a stationary coil, otherwise called as detection coils, due to the harmonic vibration of the sample in a uniform magnetic field. It is thus the detection coil geometry and configuration which decides the sensitivity of the measurement. Due to the vibration, the flux linked to the coil changes and a voltage is induced $(t) = -N\frac{\partial \emptyset(t)}{\partial t}$ **[93].**

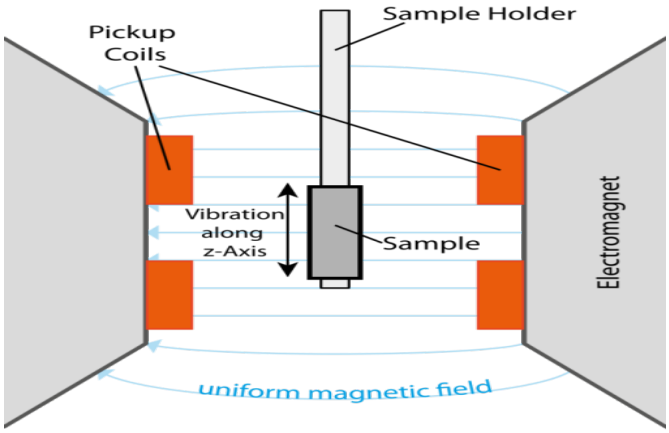

Figure 3.10: Vibrating sample magnetometer, retrieved from **[94].**

In this work, to measure the magnetic properties of the coated and uncoated samples, the Physical properties measurement system (PPMS), Quantum Design Dyna Cool was used (Fig. 3.11). At first an amount of 6 mg and 7 mg of the coated and uncoated $CoFe_2O_4$ were taken in a sample holder. Then the magnetic properties measurement was measured from magnetic field -90 kOe to +90 kOe at 27 ^oC temperature.

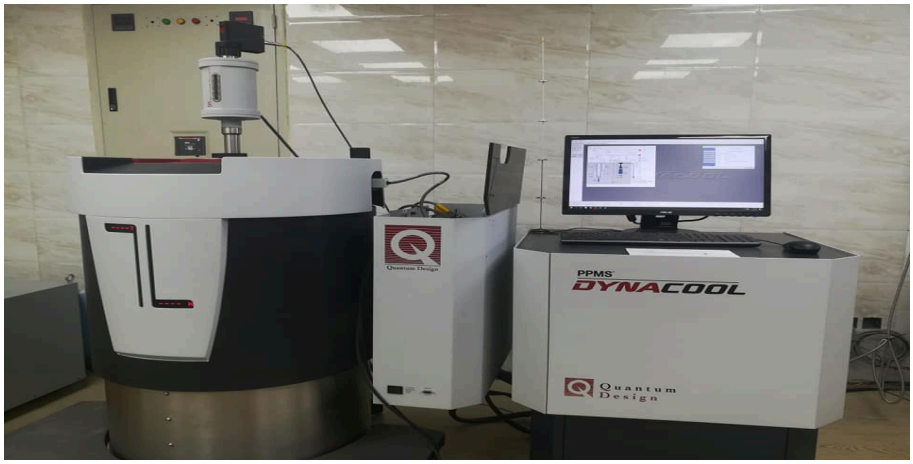

Figure 3.11: Quantum Design Dyna Cool PPMS at materials science division in Bangladesh Atomic Energy Commission.

3.2.4 Mössbauer spectroscopy

Fifty years ago Rudolf L. Mössbauer discovered the recoilless nuclear resonance absorption of γ-rays while working on his doctoral thesis. This phenomenon, which rapidly developed into a new spectroscopic technique is known as the Mössbauer effect **[95].** Over the last couple of decades, Mössbauer spectroscopy has become one of the most captivating tools in chemical physics providing information about the chemical environment of the resonating nucleus on an atomic scale **[96].** The most well-known application is the determination of iron ^{57}Fe in crystalline and in disordered solid samples. Besides iron, there are many elements in the periodic table that have Mössbauer active nuclei **[97-98].** The Mössbauer effect has been observed for the elements which are dotted in the periodic table shown the phenomenon of recoilless resonance absorption/emission of γ-rays by nuclei is the basic characteristic of Mössbauer Spectoscopy **[99].** The information of the local magnetic and electronic environment of Mössbauer nuclei (i.e. ^{57}Fe or ^{119}Sn) in a sample can be get from the Mössbauer effect. External magnetic field has no effect on this technique. Mössbauer spectroscopy has also been used to determine the average direction of magnetization by using the well-known fact that for the ^{57}Fe, The intensity of the six lines of the hyperfine spectra

have an area ratio 3: Z: 1:1: Z: 3 where $Z=\frac{4}{1+cot2\theta}$, θ being the angle between the direction of the magnetic field at the nucleus and the direction of γ-ray emission **[100].** In ^{57}Fe the strength of this magnetic field is H=33 T at room temperature. The value Z varies from 0 for the axis magnetization in the sample phase to 4 for the axis of magnetization in the sample plane. By using Mössbauer spectroscopy the resonant energy of the γ-ray's absorption could be determined precisely. So for that, it is easy to detect the small change in energy of the hyperfine interactions between the nucleus and surrounding. The change in number, shape, position, and relative force of the different ingestion lines are the main determining parts of change in the Mössbauer spectrum. This change is most often archived by oscillating a radioactive source in a very small velocity ie. mm/sec, and record the spectrum in discrete velocity steps. The energy scale of a Mössbauer spectrum in terms of the source velocity is shown in Fig. 3.12. A Mössbauer spectrum, which is a plot of the relative transmission of the γ radiation as a function of the Doppler velocity, reflects the nature and strength of the hyperfine interactions between the Mössbauer nucleus and the surrounding electrons. The Mössbauer effect makes it possible to resolve the hyperfine interactions and provide information on the electronic structure **[101].**

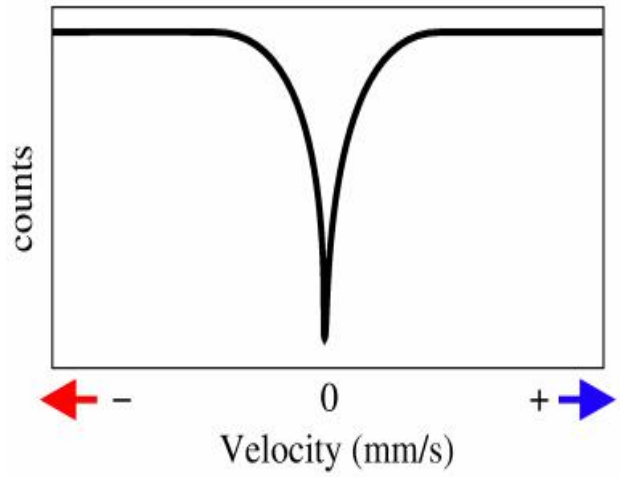

Figure 3.12: Spectrum counts vs source velocity, retrieved from **[102].**

The three main hyperfine interactions corresponding to the nuclear moments are:

Isomer Shift:

Isomer shift occurs due to a difference in the s-electron environment between the source and absorber thus produces a shift in the resonance energy of the transition. This shifts the whole spectrum positively or negatively depending upon the s-electron density, and sets the centroid of the spectrum.

Quadrupole Splitting:

Quadruple splitting occurs in the presence of an asymmetrical electric field (produces by an asymmetric electronic charge distribution) which splits the nuclear energy levels. Fe in nickel ferrite has an isotope with angular momentum quantum number, 1=3/2 excited state. The excited state is split into two sub-states $m_I=\pm1/2$ and $m_I=\pm3/2$, giving a two-line spectrum or 'doublet'.

Hyperfine field:

Magnetic field, if present, splits nuclear levels with a spin of I into (2I+1) sub states. This is known a hyperfine splitting.

In this present work, Mössbauer spectroscopy is measured in materials science division in Bangladesh Atomic Energy Commission. (Fig. 3.13).

Figure 3.13: Mössbauer spectroscopy at materials science division in Bangladesh Atomic Energy Commission.

3.2.5 Dynamic light scattering (DLS)

Dynamic light scattering (DLS) is a technique in physics that can be used to determine the size distribution profile of small particles in suspension in polymer solution **[103].** In the scope of DLS, temporal fluctuations are usually analyzed by means of the intensity or photon auto-correlation function (also known as photon correlation spectroscopy or quasi-elastic light scattering). In the time domain analysis, the autocorrelation function (ACF) usually decays starting from zero delay time, and faster dynamics due to smaller particles lead to faster decorrelation of scattered intensity trace. It has been shown that the intensity ACF is the Fourier transform of the power spectrum, and therefore the DLS measurements can be equally well performed in the spectral domain. DLS can also be used to probe the behavior of complex fluids such as concentrated polymer solutions **[104].**

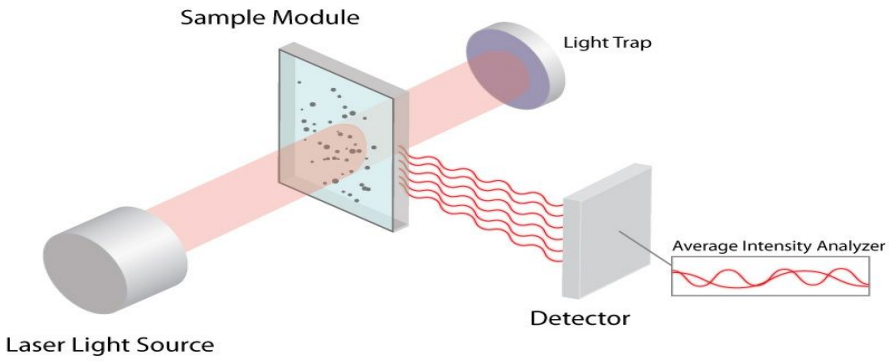

Figure 3.14: Dynamic light scattering from particle, retrieved from **[105]**

Dynamic light scattering (DLS) is a technique in physics that can be used to determine the size distribution profile of small particles in suspension or polymers in solution. A monochromatic light source, usually a laser, is shot through a polarizer and into a sample. The scattered light then goes through a second polarizer where it is collected by a

photomultiplier and the resulting image is projected onto a screen. This is known as a speckle pattern. Fig 3.14 shows the dynamic light scattering from particle.

All of the molecules in the solution are being hit with the light and all of the molecules diffract the light in all directions. The diffracted light from all of the molecules can either interfere constructively (light regions) or destructively (dark regions). This process is repeated at short time intervals and the resulting set of speckle patterns are analyzed by an auto-correlator that compares the intensity of light at each spot over time. The polarizers can be set up in two geometrical configurations. One is vertical/vertical (VV) geometry, where the second polarizer allows light through that is in the same direction as the primary polarizer. In vertical/horizontal (VH) geometry the second polarizer allows light not in the same direction as the incident light. In this work, to measure the dynamic light scattering properties of the coated samples, the Malvern Zetasizer was used (Fig. 3.15).

Figure 3.15: Malvern Zetasizer at materials science division in Bangladesh Atomic Energy Commission.

3.2.6 Zeta potential

Understanding and managing electro osmotic flow is central both to microchip separations and to the manifold techniques associated with separations analysis (sample injection, sample concentration, etc.). Microchip separations typically employ electric fields, owing both to the importance of several well-established electro kinetic separation techniques (electrophoresis, iso electric focusing, micellar electro kinetic chromatography, gel electrophoresis, and electro chromatography) and to the relative ease of integration of voltage sources and electro osmotic manipulation of fluids. The zeta potential, or potential at the solid-liquid interface (more precise definitions are to follow), is a fundamental parameter in models of electrical double layers and their associated properties (electrode capacitance, electro osmosis, etc.). The potential applied to an electrode is inherently well-defined and easily measured; hence the zeta potential is a natural parameter to use to describe electrochemical properties such as electrode capacitance. However, when the same double layer equations are extended for application to electro osmosis, interpretation of the zeta potential becomes much more complicated, since the zeta potential, rather than being straightforwardly controlled by an input voltage, is a result of detailed chemistry and ion distributions at the diffuse interface between substrate and solution. This chemical dependence, combined with the strictly inferential nature of zeta potential measurements, makes it much more difficult to measure and interpret the zeta potential for modeling of electro osmosis **[106].** In this present work the zeta potential measurements done by the Malvern Zitasizer shown in Fig. 3.15.

3.2.7 Fourier transform infrared spectroscopy (FTIR)

Fourier transform infrared spectroscopy (FTIR) is a technique that is used to obtain an infrared spectrum of absorption or emission of a solid, liquid or gas. An FTIR spectrometer simultaneously collects high spectral resolution data over a wide spectral range. FTIR spectroscopy exploits the fact that molecules absorb frequencies that are characteristic of their structure. These absorptions are resonant frequencies, i.e. the frequency of the absorbed radiation matches the vibrational frequency. The spectrum of a sample is recorded by passing a beam of infrared light through the sample. When the frequency of the IR is the same as the vibrational frequency of a bond or collection of bonds, absorption occurs. The examination of the transmitted light reveals how much energy was absorbed in each frequency (or wavelength). This measurement can be achieved by scanning the wavelength range using a monochromator. Alternatively, the entire wavelength range is measured using a Fourier transform instrument and then a transmittance or absorbance spectrum is generated using a dedicated procedure. In this present work the FTIR spectroscopy measurements done by the PerkinElmer FT-IR spectrometer shown in Fig. 3.16.

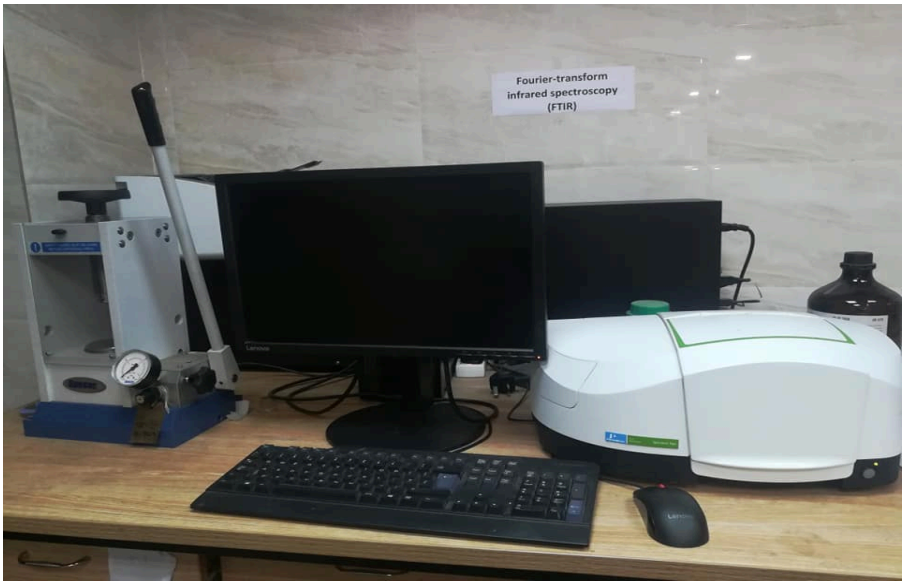

Figure 3.16: Perkin Elmer FT-IR spectrometer at materials science division in Bangladesh Atomic Energy Commission.

3.2.8 Raman spectroscopy

The discovery of Raman scattering by Krishna and Raman in 1928 is well documented. When monochromatic light of energy hν encounters matter (gas, solid, or liquid), there is a small probability that it will be scattered at the same frequency. If the object in question (e.g., a molecule) is much smaller than the wavelength of the light, the scattering is Rayleigh scattering. The "virtual state" is not necessarily a true quantum state of the molecule but can be considered a very short-lived distortion of the electron cloud caused by the oscillating electric field of the light. Blue light is more efficiently scattered than red (by a factor of ν^4, with ν the frequency of the light), and Rayleigh scattering is responsible for the blue sky. The electron cloud of the molecule is also perturbed by molecular vibrations, and the vibrational oscillations can interact, leading to Raman scattering. Raman scattering is shown in Fig. 3.17 in which the scattered photon is lower in energy by an amount equal to a vibrational transition **[107].**

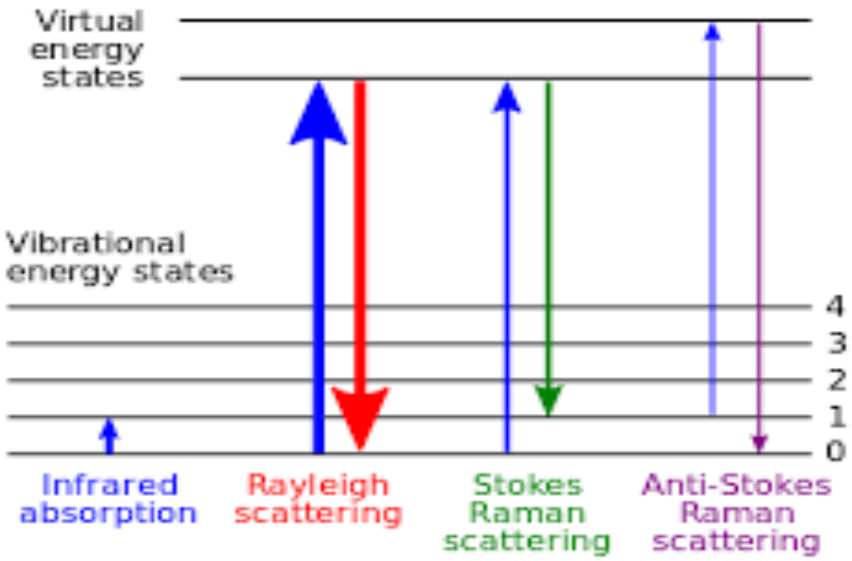

Figure 3.17: Raman spectroscopy, retrieved from **[27]**

If the molecule happens to be in an excited vibrational state when an incident photon is scattered, the photon may gain energy when scattered, leading to anti-Stokes Raman scattering. The Stokes and anti-Stokes Raman peaks are symmetrically positioned about the Rayleigh peak, but their intensities are very different except for low vibrational energies. Infrared absorption, often called Fourier transform infrared (FTIR) or mid- IR absorption, also depends on molecular vibrations. Although Raman spectroscopy probes vibrational transitions indirectly by light scattering, the Raman shift has the same energy range as FTIR absorption, and in many cases, the same energies are observed. The selection rules for Raman scattering and FTIR are different, but the chemical information is similar. A fundamental difference between absorption and Raman scattering is a probability, with absorption usually being a far more likely event **[108].** In this present work the Raman spectroscopy measurements done by the MonoVista CRS S&I shown in Fig. 3.18.

Figure 3.18: Mono Vista CRS S&I Raman Spectroscopy at materials science division in Bangladesh Atomic Energy Commission.

3.2.9 Induction heater

Magnetic hyperthermia is a promising option for cancer therapy. In this method, MNPs are heated by an external alternating (AC) magnetic field. After applying the magnetic field, nanoparticles are generating heat by the process of eddy current, hysteresis losses, and relaxation loss. Advances in science have made it so that magnetic nanoparticles can be specifically targeted at cancer cells, making magnetic hyperthermia a truly local treatment. MNPs can therefore, be used to induce localized hyperthermia used to kill tumors or by increasing the effectiveness of radiotherapy or chemotherapy. The procedure consists of dispersing MNPs within the target tissue and applying an AC magnetic field that causes the particle to produce heat. In addition, due to the small area of the treatment, the nanoparticles can be heated to a temperature high enough to kill the cancer cells while keeping surrounding tissue unaffected.

The hyperthermia measurements were carried out an induction heating set up. Induction heating is a convenient and flexible method to deliver high-strength magnetic fields to nanoparticles, resulting in a focused and targeted treatment that is gaining considerable interest in the medical research community. Induction heating systems are used in thermotherapy to generate alternating magnetic fields in the laboratory to elevate and manage the temperature of a solution of nano-particles in vitro or (in animal studies) in vivo. A basic induction heating setup consists of a high-frequency power supply that takes the input from the alternating current (AC) line mains. This power supply unit converts regular line frequency (50 Hz or 60 Hz) to a high-frequency signal, typically operating between 10 kHz and 400 kHz. This high-oscillating signal is then fed to a tank circuit that feeds the water-cooled induction heating coil. The high-frequency signal generates a high-frequency magnetic field inside the induction heating coil. The sample consisting of the nanoparticle mixture is placed inside this induction heating coil. It interacts with the high-frequency

magnetic field and produces heat. An optional fiber-optic thermocouple is immune to the radio frequency interference and can be used during the heat cycle. Its output can then be fed to a controller that can regulate the rate of increase of temperature as well as maintain a particular sample at temperature for a specific amount of time.

Typical induction heating coils are made of hollow copper tube with water as a cooling medium flowing through the inside. The most common type of coil is a simple solenoid or a helical coil. The copper coil is described by the size of the copper tube, the inside diameter (d=2a, where a is the radius) bore produced by the wound copper tube, the number of turns (N) of the copper tube, and the length (L) of the entire stacks of the copper tubes. The current (I) flows through the copper to create the magnetic field. The magnetic field intensity is the largest in the center of the coil and drops off as one traverse to the ends of the coil. The heat produced by the resistance heating of the copper of the coil might radiate to the sample and distort the absolute heating attained in the sample. A simple but innovative solution counteracts this heating effect. A 1.5875 mm (0.0625 in.) diameter non conducting tube made of synthetic fluorine-containing resin is wound in the shape of a solenoid and is placed between the sample and the induction heating coil. Care is taken that this solenoid does not physically touch the sample or the copper of the coil to prevent any conductive heat transfer. Air is then blown through the solenoid to dissipate any heat coming from the induction coil to the sample. This isolates the sample from any external heat input and only true heat produced in the nanoparticles is measured using the fiber-optic thermometer. Then the recorded temperature is plotted as a function of the duration of the applied magnetic field to determine the heating properties of the nonmaterial. In this present work the hyperthermia measurements done by Ambrell EASY HEAT (800s Series, USA) shown in Fig. 3.19.

Figure 3.19: Ambrell EASY HEAT (800s Series, USA)
at materials science division in Bangladesh Atomic Energy Commission.

3.2.10 Magnetic resonance imaging (MRI)

MRI is a high imaging technique used in radiology to form pictures of the anatomy and the physiological process of the body. MRI scanners use strong magnetic fields, magnetic field gradients, and radio waves to generate images of the organs in the body shown in Fig. 3.20 MRI does not involve X-rays or the use of ionizing radiation, which distinguishes it from CT or CAT scans and PET scans. MRI scan may still be seen as a better choice than a CT scan. In MRI, hydrogen atoms are most often used to generate a scan object being examined. Hydrogen atoms are naturally abundant in people and other biological organisms, particularly in water and fat. For this reason, most MRI scans essentially map the location of water and fat in the body. Pluses of radio waves excite the nuclear spin energy transition, and magnetic fields gradients localize the signal in space. By varying the parameters of the pulse sequence, different contrasts may be generated between tissues based on the relaxation properties of the hydrogen atoms.

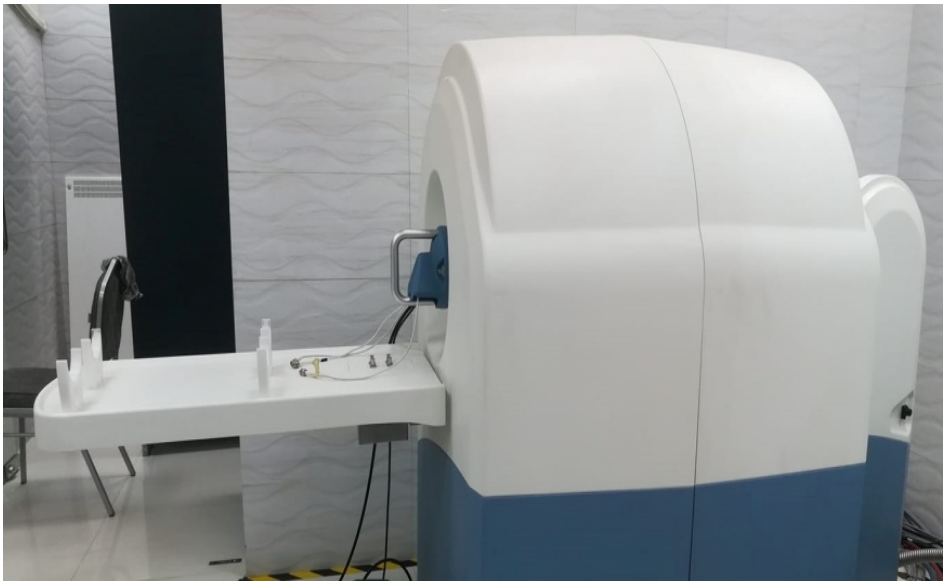

Figure 3.20: Laboratory research MRI (MRS7017, MR solution, UK) at materials science division in Bangladesh Atomic Energy Commission.

Chapter 4: Result & Discussions

4.1 X-ray diffraction (XRD)

X-ray diffraction (XRD) provides information on structures, phases, preferred crystal orientations (texture), and other structural parameters, such as average grain size, crystallinity, strain, and crystal defects. The peaks are determined by the diffraction of the incident beam of X-rays by the planes of atoms within the lattice that satisfy the Bragg's law $n\lambda = 2d \sin\theta$ caused by the constructive interference. The peak intensities are determined by the multiplicity of the planes. The X-ray diffraction patterns are the fingerprint of the structure of materials **[109].** In this study, X-ray diffraction technique has been utilized to discuss the structural parameters of $CoFe_2O_4$ nanoparticles prepared by chemical co-precipitation. As-prepared samples were analyzed by Philips X'pert pro XRD (PW3040) system with Cu- Kα radiation of wavelength λ= 1.54178 Å in the range of 2θ= 15 to 70 degree in the step of 0.01º/sec.

The XRD patterns of the synthesized sample are shown in Fig. 4.1. The XRD pattern was analyzed by X'Pert High score and was indexed compared with the standard pattern of $CoFe_2O_4$. It was found that there was a peak shift from the standard pattern, yet the peaks were identified as (111), (220), (311), (222), (400), (422), (511) and (440). Since there wasn't any additional peak detected, it might be assumed that the sample is single-phase with inverse spinel structure. The broad peaks represent the crystallite sizes of low dimensions **[110].** The full-width half maxima (FWHM) was determined by the peak fit using the X'Pert High score software. The average crystallite size was found 12 nm presented in Table 4.1, which was calculated from the line broadening of the highest intensity peak of Miller index (311) using Scherrer's formula,

$$D = K\lambda / (\beta \cos\theta) \qquad (1)$$

Where, D is the crystallite size (nm), K= Scherrer constant. K varies from 0.68 to 2.08. Value of K is 0.94 for spherical crystallites with cubic symmetry, λ= X-ray wavelength, which is

1.54178 Å for Cu- Ka radiation, β= FWHM (Full Width at Half Maximum) of XRD peak and θ = is the Bragg angle (in degrees).

The lattice parameter was determined using the following formula

$$a = d\sqrt{(h^2 + k^2 + l^2)} \qquad (2)$$

where, a is the lattice parameter, d is the interplanar spacing, and h, k, l are miler indices of respective planes. To determine the absolute value of the lattice parameter Nelson – Riley function was invoked. Nelson – Riley function F(θ) is given as:

$$F(\theta) = \frac{1}{2}[(Cos^2\theta / Sin\theta) + (Cos^2\theta / \theta)] \qquad (3)$$

The values of the relative lattice parameter determined from each peak are plotted as a function of F(θ) and presented in Fig. 4.2. From the linear fitting of the datathe lattice parameter was determined from the intercept at F(θ)= 0 and found as 8.335 Å. Thus, the lattice parameter of the synthesized cobalt ferrite nanoparticle was determined.

Table 4.1 : Grain size determination from most intense peak at (311) plane and lattice parameter of $CoFe_2O_4$ nanoparticle.

Scherrer's constant K	X-ray wavelength λ (Å)	Peak position 2θ (deg)	FWHM 2θ (deg)	Average D (nm)	Lattice parameter a (Å)
0.94	1.54178	35.88	0.7295	11.96	8.335

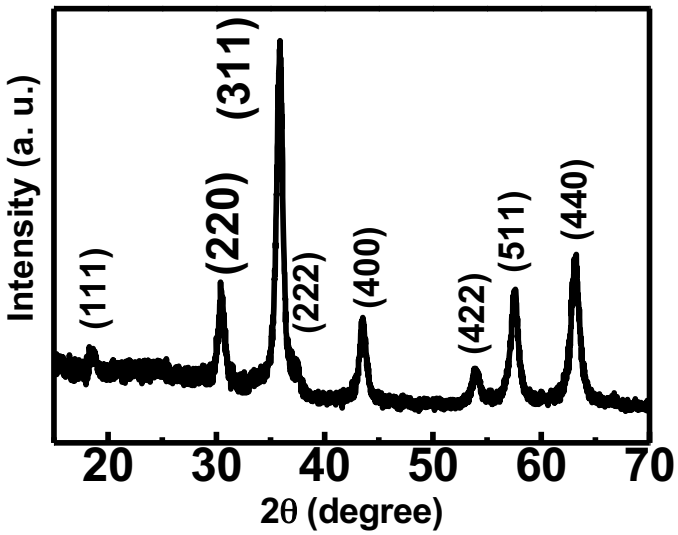

Figure 4.1: X-ray diffraction pattern of $CoFe_2O_4$ nanoparticle (as dried)

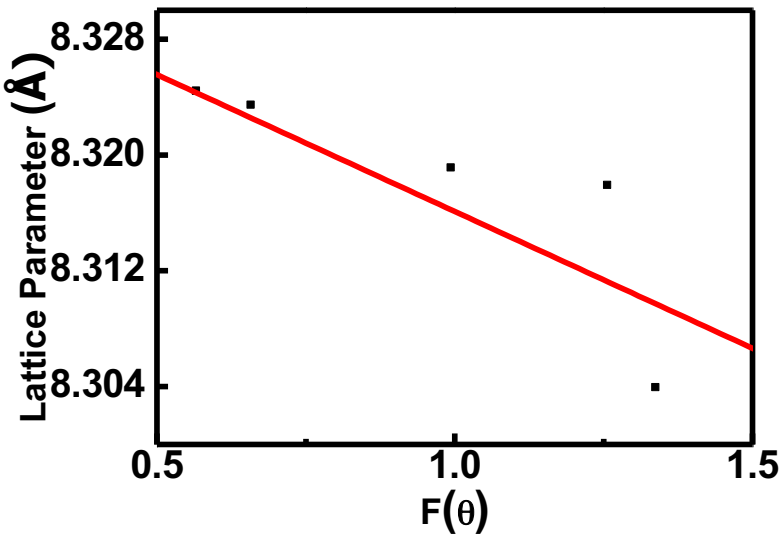

Figure 4.2: Lattice parameters of $CoFe_2O_4$ nanoparticle (as dried)

4.2 Transmission electron microscope (TEM)

For TEM analysis, a Talos 200X transmission electron microscope was used. The operating voltage was 200 kV. The samples for TEM analysis were prepared by drop-casting method dispersed on a Cu-grid. Fig. 4.3 shows TEM (a) bright-field (BF), (b) dark-field (DF) and (c) selected area diffraction (SAED) patterns of bare $CoFe_2O_4$ nanoparticles. The BF and DF images are constructed using the method of the conical dark field from the selected area diffraction patterns from the same region. The BF image was obtained from the transmission beam and the DF image was obtained from the diffracted beam of 311 diffraction circle. From the same region high resolution transmitted electron micrograph (HRTEM) image was obtained and presented in Fig. 4.3 (d). The lattice fringes of HRTEM images are visible in the HRTEM image. High crystallinity of the $CoFe_2O_4$ nanoparticles are evident from all the BF, DF, SAED and HRTEM images. An attempt has been made to determine the distribution of the particle size. The particle size distribution followed the log-normal distribution presented in Fig. 4.3 (e). Chemical purity and stoichiometry of the $CoFe_2O_4$ nanoparticles were investigated by EELS spectroscopy. The strong peaks related to Fe, Co and O were found in the Fig. 4.3 (e). The EELS results also confirmed that the precursors used in the synthesis have fully undergone the chemical reaction to form the single phase nanocrystalline cobalt ferrite.

The BF, DF, SAED and HRTEM images of folate-chitosan coated $CoFe_2O_4$ nanoparticles are presented in Fig. 4.4 (a), (b), (c) and (d) respectively. It might be mentioned that all the images were formed from the same region using conical dark field method where BF image was constructed from the transmitted beam and the DF image was constructed from the diffraction beam of 311 plane. The BF and DF images presented in Fig. 4.4 (a) and (b) were acquired at low magnification to demonstrate high dispersion of the coated nanoparticle. The diffraction rings of all the lattice planes are present in the selected area diffraction (SAED)

pattern presented in Fig. 4.4 (c). In Fig. 4.4 (d), the HRTEM image of a single agglomerate of the coated nanoparticle is presented. The lattice fringes of different directions represent the presence of more than a single particle. The size of this agglomerate is 10-12 nm. The layer of coating is clearly visible from the HRTEM image presented in Fig. 4.4 (d). It is observed from the TEM micrographs that most of the particles appear semi-spherical in shape. It is observed from the BF and DF images of Fig. 4.3 (a) and (b) and also the HRTEM image in Fig. 4.3 (d) that in the bare state particles are highly agglomerated. Whereas the BF, DF and HRTEM images of 4.4(a), (b) and (d) demonstrate that the folate-chitosan coated nanoparticles are well dispersed. The agglomeration of the bare state happened due to dipole and weak exchange interaction of the magnetic $CoFe_2O_4$ nanoparticle **[111].** The coating of a single particle is not possible; more than a single nanoparticle was agglomerated inside a coating as can be observed from the HRTEM image presented in Fig. 4.4(d).

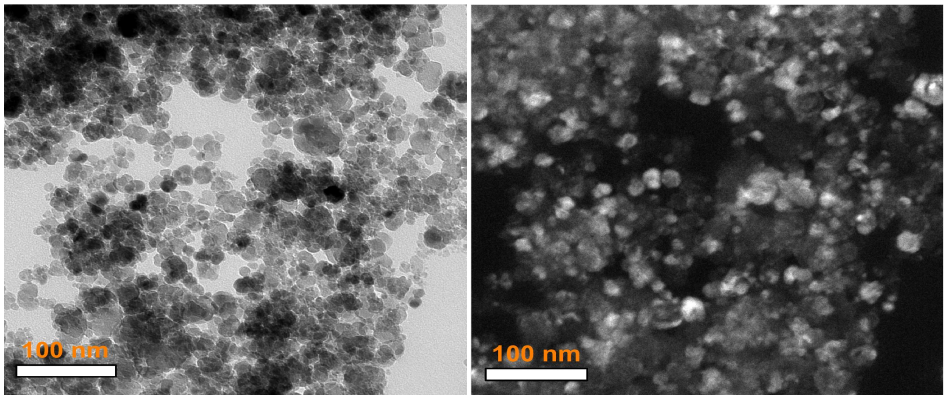

(a) **(b)**

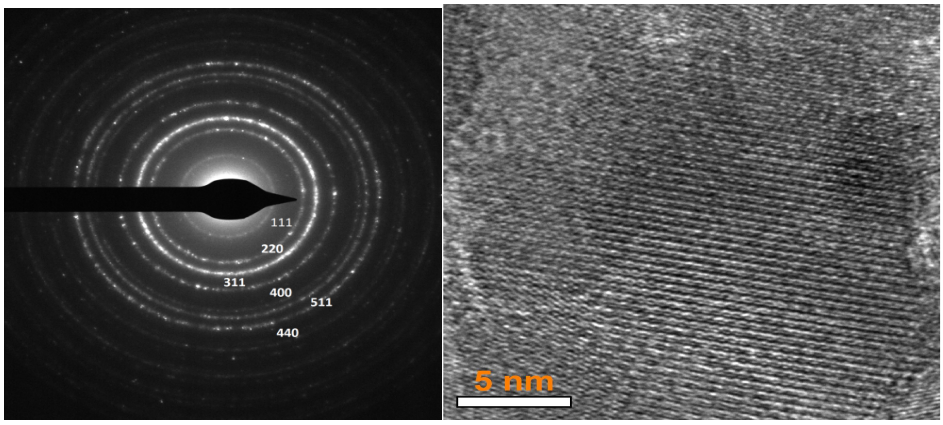

(c) **(d)**

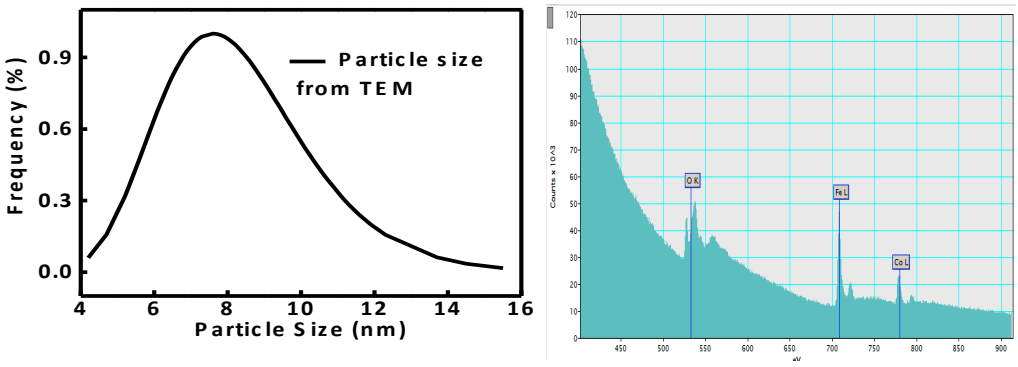

(e) **(f)**

Figure 4.3: Bare $CoFe_2O_4$ **(a)** Bright field TEM image **(b)** Dark field TEM image **(c)** SAED patterns **(d)** HRTEM image for lattice fringes **(e)** Log normal distribution of particle size **(f)** EELS image

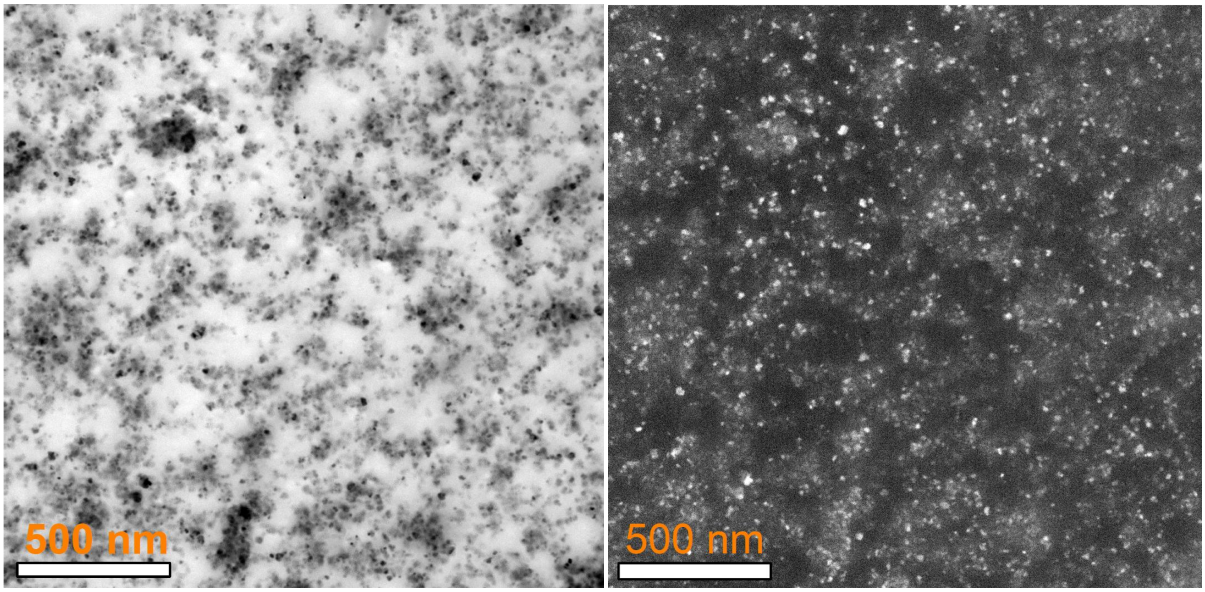

(a) **(b)**

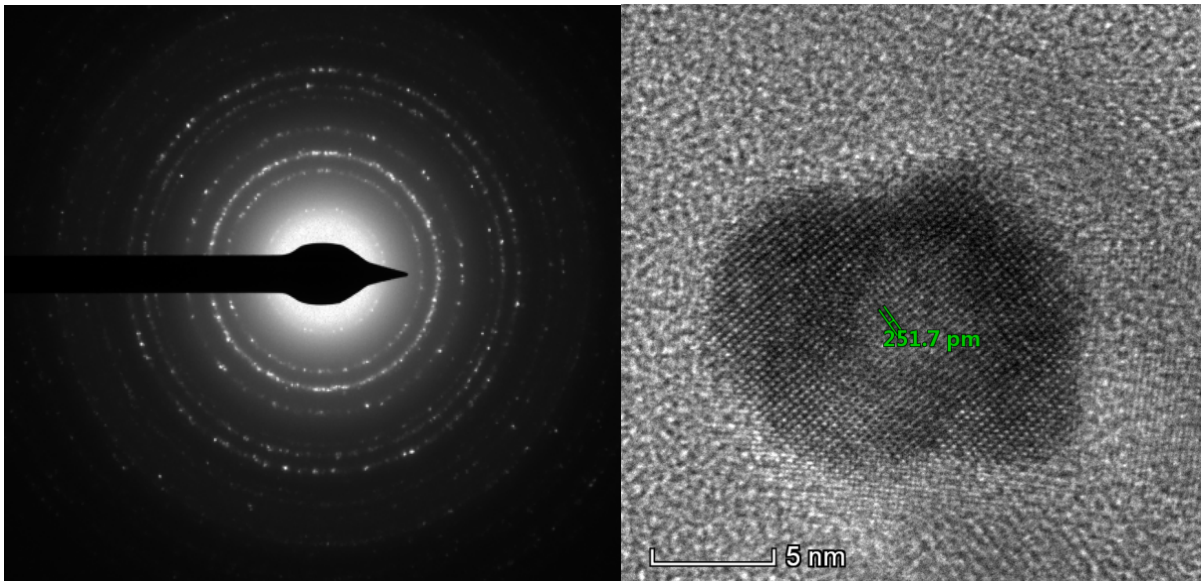

(c) **(d)**

Figure 4.4: Coated $CoFe_2O_4$ **(a)** Bright field TEM image **(b)** Dark field TEM image **(c)** SAED patterns **(d)** HRTEM image for lattice fringes

4.3. Vibrating sample magnetometer (VSM)

The magnetic properties are the most important properties of ferrites, upon which biomedical applications nano ferrites are largely dependent. The magnetic properties of ferrites are dependent on the processing conditions, nanostructure, chemical composition, and the type of the additives **[111]**. The net magnetic moment in the ferrimagnetic materials depends upon the number of magnetic ions occupying the tetrahedral and octahedral sites. Although saturation magnetization is an intrinsic property for bulk material that doesn't depend on the structure of the materials however, for nanoparticle saturation magnetization strictly depends on the crystallite size, cation distribution and particle agglomeration because of the large surface to volume ratio **[112]**. Fig. 4.5 shows the M-H hysteresis loops of as-dried $CoFe_2O_4$ nanoparticles at 27 °C measured with the maximum applied field of 90 kOe. It might be observed that even at this high magnetic field the magnetization didn't saturate. A finite slope exists towards the highest magnetic field. The values of maximum magnetization, M_{max} are 51 emu/g for uncoated $CoFe_2O_4$ nanoparticles and 40 emu/g for folate chitosan-coated samples. The reduction of magnetization may be attributed due to the presence of non-magnetic polymer layer on to the surface of the nanoparticles which reduces the particle-particle interaction and lowers the exchange energy **[113].** In Fig. 4.5 the magnified value of M-H hysteresis loop in the region of the applied field of 3 kOe is presented to demonstrate the effect of coating on remanence and coercivity. The remanence and coercivity are 15 emu/g and 679 Oe for uncoated cobalt ferrite whereas 8 emu/g and 459 Oe for coated samples. This drastic decreases of the remanence magnetization and the coercivity strongly demonstrate the surface modification by folate-chitosan coating of the cobalt ferrite nanoparticle.

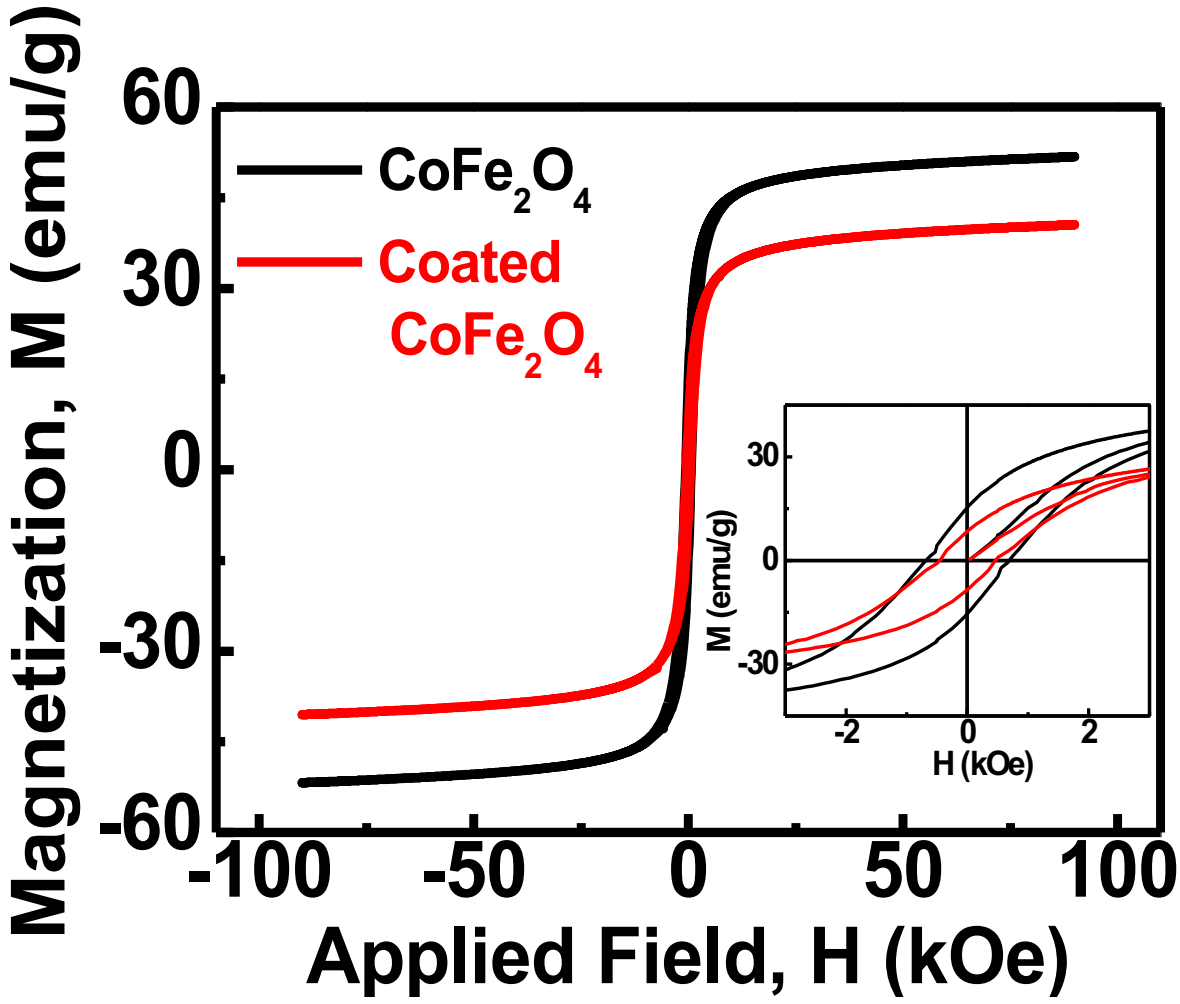

Figure 4.5: M-H hysteresis loops for the uncoated and coated $CoFe_2O_4$ at 27 °C with applied field 90 kOe and 3 kOe

4.4 Mössbauer spectrocopy

Due to fine energy resolution, Mössbauer spectroscopy can be used to detect even a minute change in the nuclear realm of the iron atoms. In Mössbauer spectroscopy, γ-rays are emitted or absorbed by the crystal without energy loss. The hyperfine parameters of the Mössbauer spectroscopy is a convenient tool to determine the cation distribution and magnetic state of the materials **[114]**. Mössbauer spectra of $CoFe_2O_4$ nanoparticle is presented in Fig. 4.6 spectral fits were performed assuming lorentzian absorption line shapes using the Mössbauer spectral line fitting software WMOSSR which allows for fitting the spectra with mixed relaxation. The goodness of fitting χ^2 value is = 0.898 which demonstrate that there is a good agreement between theoretical and experimental data. Fig. 4.6 shows the Mössbauer spectrum of $CoFe_2O_4$ nano-ensembles in the as-dried condition at room temperature and without any magnetic field. The spectrum exhibited the nature of mixed relaxation consisting of a central doublet region with relatively smaller peaks of Zeeman contribution. Five sub-species were required to fit the experimental data. There are four sub-species that exhibit the Zeeman type sextets splitting which is responsible for slow relaxation and therefore the ferromagnetic phases. The other single sub-species characterizing the central doublet represents fast relaxation and therefore superparamagnetic **[115].** The hyperfine interactions like isomer shift (IS), quadrupole splitting (QS), magnetic hyperfine field (H_f), relative area (A), and cation distribution were determined from the analysis of the spectra which are presented in Table 4.2. Since higher quadruple splitting are assigned to the A sites and the lower values are assigned to the B sites. By reviewing literature, we can assume that the outer sextets correspond to Fe^{3+} ions in tetrahedral or A site and the inner sextets correspond to Fe^{3+} ion in octahedral or B site **[115].** Thus, the cobalt ferrite synthesized in this study possesses 51% and 49% of A and B site occupancy. Further, it can be observed that 21% of sub-species represent superparamagnetic behavior and 89% of the sub-species represent

ferrimagnetic behavior. This agrees well with the MH loop of the uncoated sample in Fig. 4.5. The nature of the hysteresis loop is mainly ferrimagnetic. But the finite slope at a higher magnetic field demonstrates superparamagnetic phases embedded in the ferrimagnetic matrix.

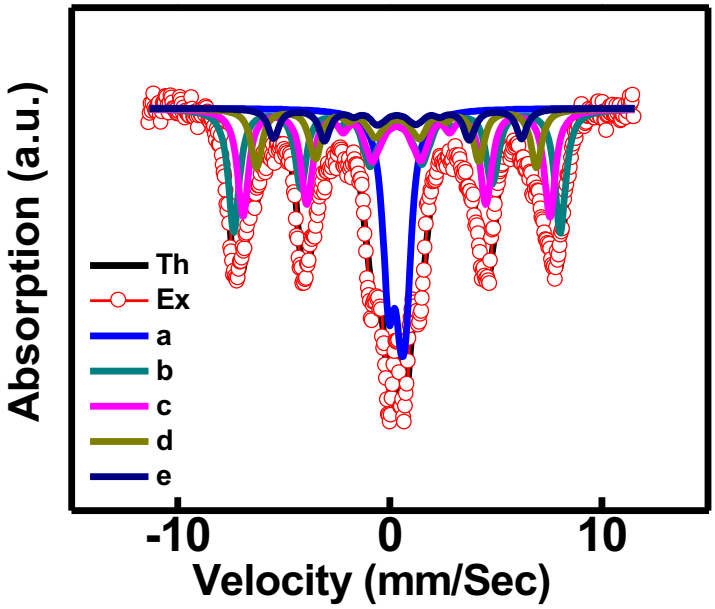

Figure 4.6: Mössbauer spectra at room temperature of $CoFe_2O_4$ nanoparticles in the as-dried condition.

Table 4.2: Mössbauer parameters of $CoFe_2O_4$ nanoparticles at room temperature

Sub-species	**Chemical shift (δ) mm/sec**	**Quadruple splitting (ΔEq) mm/sec**	**Hyperfine field (H_{int}) kG**	**Rel. area (%)**	**Total B site occupancy (%)**	**Total A site occupancy (%)**
Fe_A^{3+}	0.294	0.705	0	21	51	49
Fe_B^{3+}	0.320	0.086	479.271	28		
Fe_A^{3+}	0.311	0.175	450.393	28		
Fe_B^{3+}	0.331	0.133	410.797	15		
Fe_B^{3+}	0.346	0.105	364.339	8		

4.5. Fourier transform infrared spectroscopy (FTIR)

Folic acid conjugated chitosan was used to coat the cobalt ferrite nanoparticles. Here electrostatic interaction occurred since the cobalt ferrite nanoparticles are negatively charged due to the presence of –OH group on the surface and chitosan is slightly positive (protonated). Confirmation of the presence of folate-chitosan on the surface of nanoparticles is done by Fourier transformation infrared spectroscopy (FTIR) shown in Fig. 4.7.

In spinel ferrite structure, the vibrational band around 550 cm^{-1} corresponds to the stretching vibration of tetrahedral group and the vibrational band around 350 cm^{-1} corresponds to the stretching vibration of octahedral groups **[116].** It is found from Fig. 4.7 of uncoated samples that the octahedral and tetrahedral absorption peaks are at 357 cm^{-1} and 594 cm^{-1}. These absorption bands further confirm the formation of $CoFe_2O_4$ spinel ferrite structure.

Folate Chitosan (FC) conjugation was also confirmed by FTIR spectra as shown in Fig. 4.7. The broad band between 3500-3300 cm^{-1} is attributed to N-H and O-H vibrations respectively. The peak at 2920.27 cm^{-1} was for C–H stretching vibration of CH_2 symmetry. The peaks appear at 1550 cm^{-1} and 1017 cm^{-1} were responsible for the vibration of newly formed C–N bond. The peak at 1430 cm^{-1} was for the presence of pteridine ring stretching of folate group which confirmed the binding of folic acid to chitosan. FTIR spectra of folate chitosan in this study exactly match with those obtained by Tiwari el at **[116].** The folate chitosan coating on the surface of cobalt ferries is confirmed by the shift of the peaks of the folate chitosan coated cobalt ferrites (FCNPs) FTIR spectroscopes image shown in Fig. 4.7.

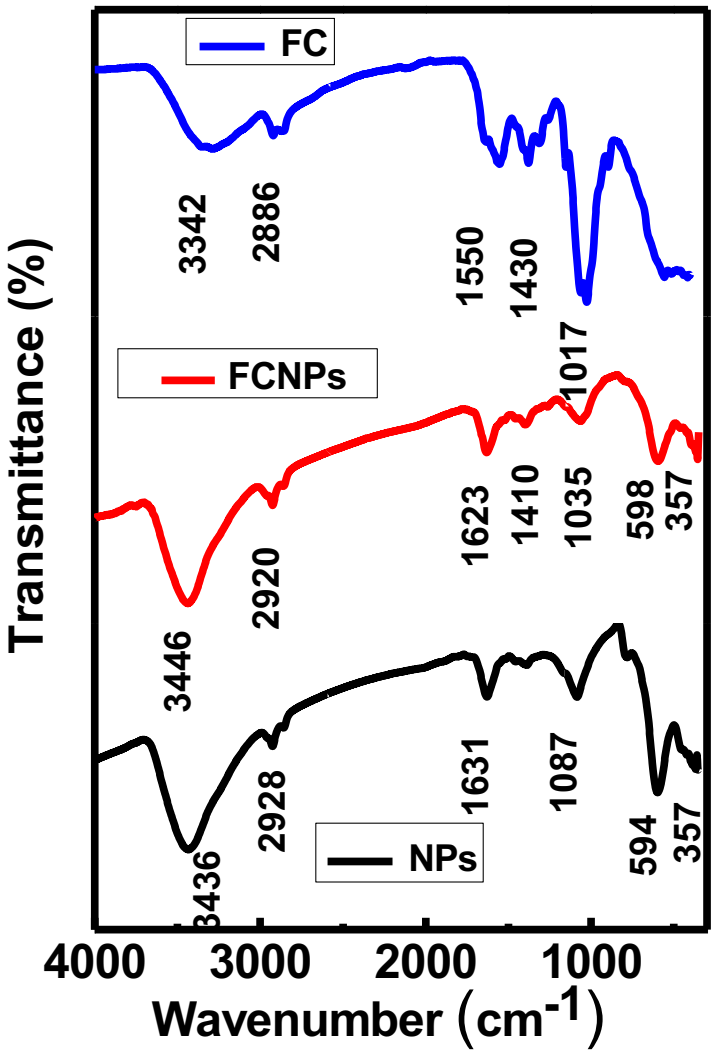

Figure 4.7: FTIR spectra of $CoFe_2O_4$ nanoparticles (NPs), folate chitosan coated $CoFe_2O_4$ nanoparticles (FCNPs), folate chitosan.

4.6. Raman spectroscopy

Raman spectroscopy is a powerful technique for investigating the atomic structure of nanoparticles **[118].** Fig. 4.8 shows the Raman spectra of $CoFe_2O_4$ spinel ferrite nanoparticles. Group theory analysis predicts the following optical phonon distribution: $5T_{1u} + A_{1g} + E_g + 3T_{2g}$, in which the $5T_{1u}$ modes are IR active, whereas the other five ($A_{1g} + E_g + 3T_{2g}$) modes are Raman active composed to the motion of O ions and both A-site and B-site ions in the spinel structure **[119].** Furthermore, the A_{1g} mode is associated with symmetric stretching of the oxygen anion, the E_g mode is associated to symmetric bending of the oxygen anion, and the T_{2g} mode is due to asymmetric stretching of the oxygen anion with respect to the tetrahedral and octahedral cations **[120].** The Raman modes at 619 cm^{-1} were assigned to A_{1g} (1) modes, demonstrating the stretching vibrations of the Fe–O bonds in tetrahedral sites. The lower frequency Raman modes 240 cm^{-1}, 300 cm^{-1}, 461 cm^{-1}, 545 cm^{-1} were assigned to the T_{2g} and E_g Raman modes, demonstrating the vibration of the spinel structure **[116].**

Since, folate chitosan is characterized by very high absorption, the intensity of the coated peaks is very weak compared to their bare counterpart. However, the peaks in the coated nanoparticles are shifted which demonstrates successful coating.

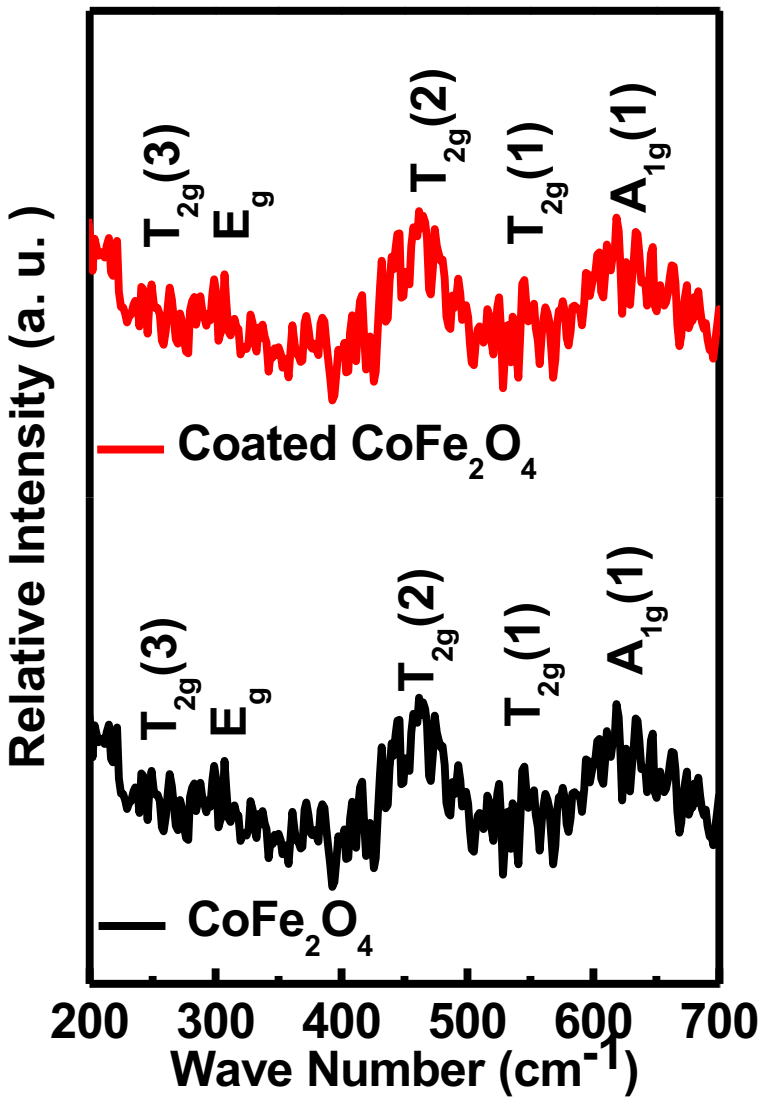

Figure 4.8: Raman spectra of $CoFe_2O_4$ nanoparticles, folate chitosan coated $CoFe_2O_4$ nanoparticles (FCNPs).

4.7. TG-DSC Curves

The TG-DSC curves were recorded under the N_2 flow inert environment and the temperature rose at 10 ºC /min. Singh et al **[124]** reported that dehydration takes place up to 450 ºC and further increasing the temperature brings more crystallinity of the cobalt ferrites nanoparticles. In this present study the Fig. 4.9 (a) to (b) and Fig.4.10 (a) to (b) show the DSC-DDSC and TG-DTG curve for $CoFe_2O_4$ and folate-chitosan coated $CoFe_2O_4$. In Fig. 4.9 (a) the DSC-DDSC curve shows a sharp exotherm peak at 50 ºC followed by another exotherm peak at 150 ºC due to dehydrazination. The TG-DTG curve in Fig 4.9 (b) also shows the 3.84% mass loss due to dehydrazination exotherm reaction. Since the samples were prepared co-precipitation method that is why a lot of deionized water was used during the sample preparation time. This water remained in the inter molecular space and outer surface of the prepared samples. The FTIR studies also confirmed the presence of this water. After the temperature 1100 ºC, the Fe^{2+} ions turn to the Fe^{3+} ions.

In the Fig. 4.10 (a), the DSC-DDSC curve shows the same peaks as $CoFe_2O_4$ with an additional exothem peak at 288 ºC due to the breakdown of the folate chitosan coating. The TG-DTG curve in Fig 4.10 (b) shows the 2.34% mass loss due to folate chitosan break down.

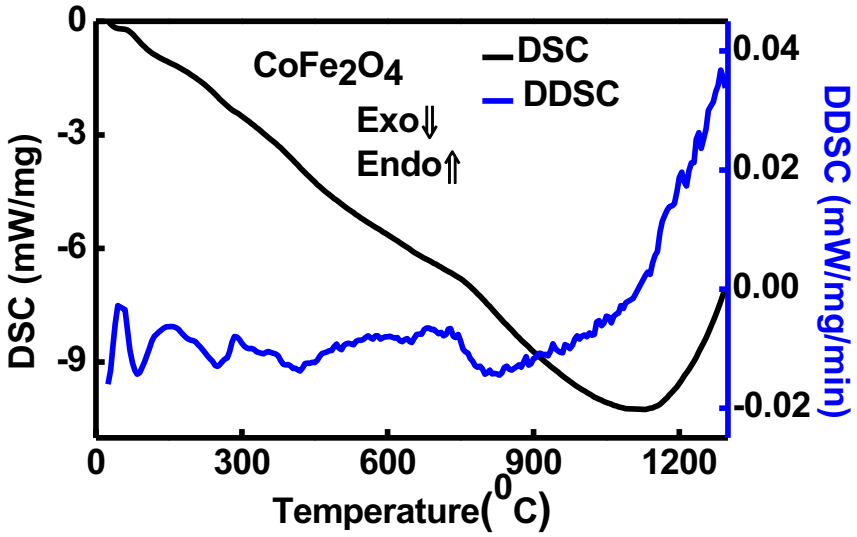

(a)

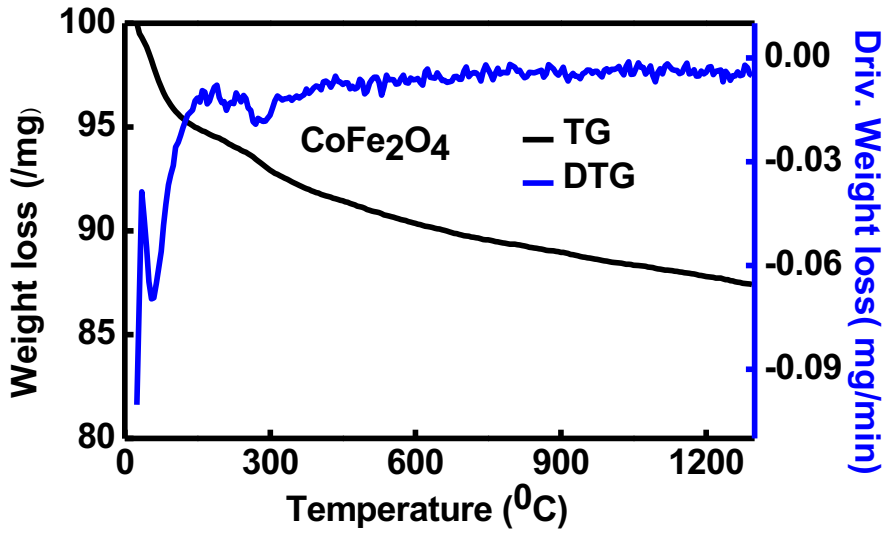

(b)

Figure 4.9: (a) DSC and DDSC curves (b) TG and DTG curves $CoFe_2O_4$ nanoparticles.

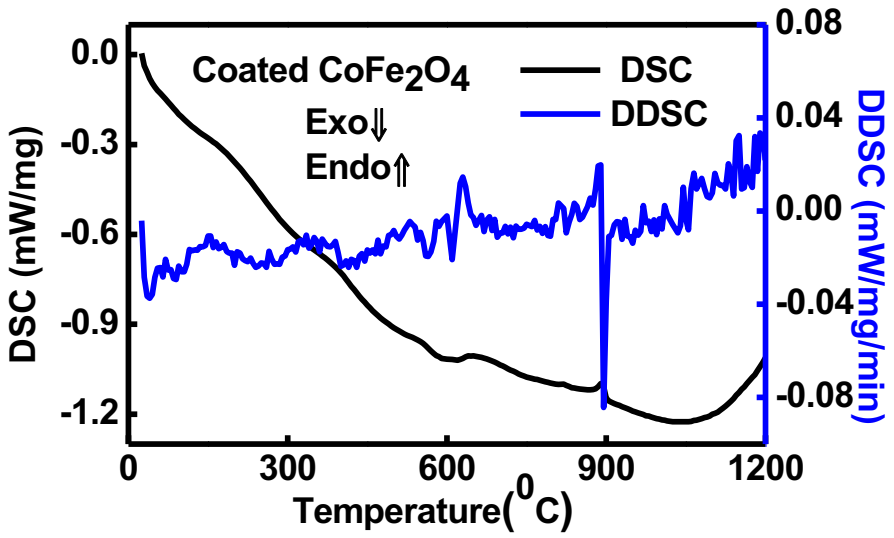

(a)

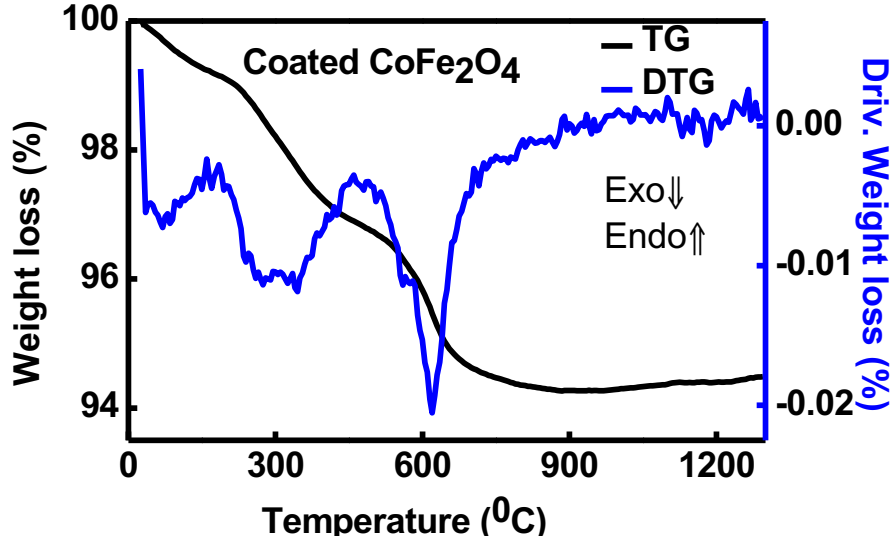

(b)

Figure 4.10: (a) DSC and DDSC curves (b) TG and DTG curves of folate chitosan coated $CoFe_2O_4$ nanoparticles.

4.8. Dynamic light scattering (DLS)

The hydrodynamic diameter of the nanoparticle is very important to know before using it for biomedical applications. Dynamic light scattering (DLS) is the most versatile and useful set of techniques for measuring in situ the sizes, size distributions, and (in some cases) the shapes of nanoparticles in liquids. It reveals information about the diameter of the inorganic core along with the attached dragging fluid while the coated nanoparticle is in the Brownian motion **[37].** Information only about the organic core were gathered during the estimation of grain size using XRD, TEM in the absence of the hydration layer. But for better understanding during in-vivo transportation of the nanoparticles and optimizing its performance in biological application, the measurement of hydrodynamic diameter is crucial and this value should be below 250 nm **[121- 112].** The polydispersity index is another important parameter. In general, a low polydispersity index is a prerequisite for biomedical applications and its normal range should be less than 0.3.

The sample were diluted to 0.5 mg/ml, 1 mg/ml, 2 mg/ml, 4 mg/ml, 6 mg/ml concentration then hydrodynamic diameter and poly-dispersity index (PDI) measurements were carried out using dynamic light scattering (DLS) at 25 ºC, 37 ºC and 45 ºC temperatures. These three temperatures were selected because 25 ºC is room temperature, 37 ºC is human body fluid temperature and 42-46 ºC is cancer cell destroy temperature. All the data are represented in Fig.4.11 (a-c) and tabulated in Table 4.3. The value of hydrodynamic size increases with the increases of concentration of the suspended samples and PDI value remained below 0.25 for all the concentrations. For the biomedical applications as well as the low concentration samples are more applicable, here 0.5 mg/ml concentrated sample showed the low hydrodynamic value and PDI value for all temperatures.

Figure 4.12 shows the zeta potentials distribution for all diluted coated samples. Zeta potential analysis was used to evaluate the electrostatic charge on the surface of the folate

chitosan-coated cobalt ferrites nanoparticles and this surface charge depends strongly on the pH of the suspension **[123].** The obtained results for all the different concentration suspended samples are represented in Table 4.3. The zeta value of all suspension was +39.5 mV to +48.4 mV, which confirmed that folate chitosan was stably coated on the surface of the nanoparticles **[124].** The uncoated samples have negative zeta value; coated nanoparticles have a positive zeta value.

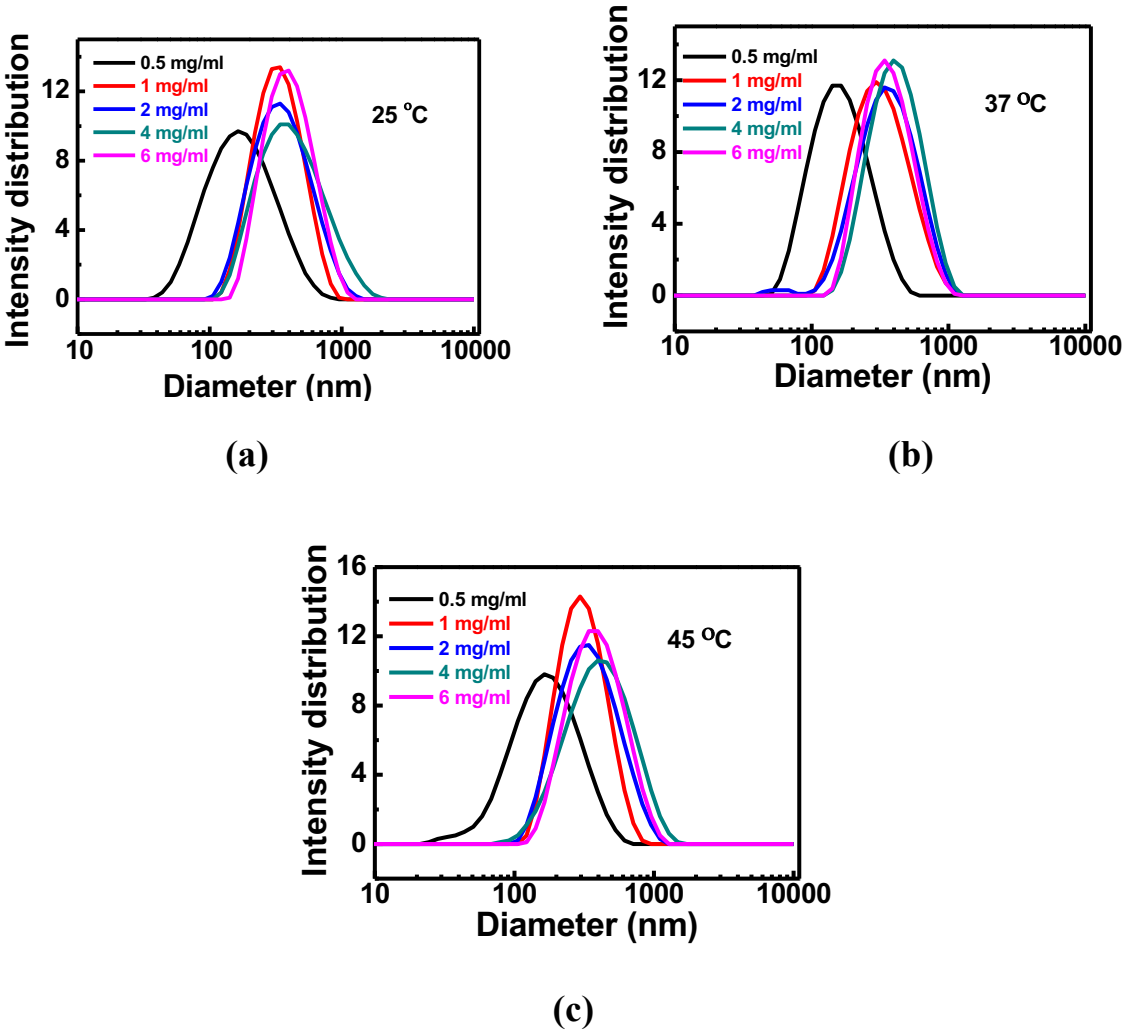

Figure 4.11: Hydrodynamic diameter, polydispersity index of folate chitosan coated $CoFe_2O_4$ nanoparticles at (a) 25 ºC (b) 37 ºC (c) 45 ºC

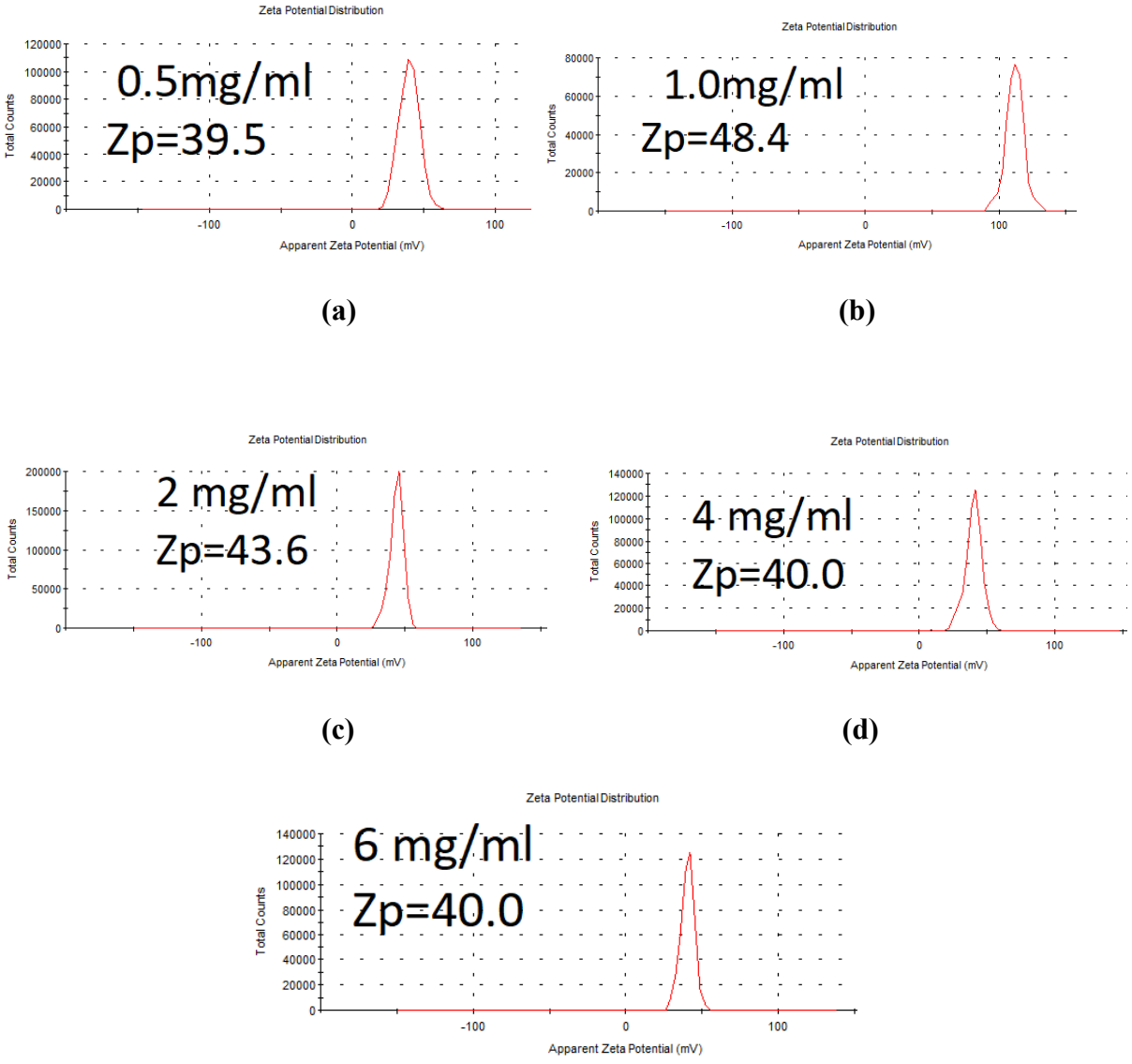

Figure 4.12: Zeta potential of (a) 0.5 mg/ml (b) 1 mg/ml (c) 2 mg/ml (d) 4 mg/ml (e) 6 mg/ml folate chitosan coated $CoFe_2O_4$ nanoparticles at 25 ºC

Table 4.3: Hydrodynamic diameter, polydispersity index PDI and zeta potential of folate chitosan-coated $CoFe_2O_4$ suspension.

Concentration	DLS			Zeta potential (mV) at 25 ºC
	Temperature(ºC)	Hydrodynamic Size (nm)	Polydispersity index	
0.5 mg/ml	25 ºC	144	0.237	39.5
	37 ºC	143	0.227	
	45 ºC	154	0.331	
1 mg/ml	25 ºC	285	0.197	48.4
	37 ºC	275	0.207	
	45 ºC	271	0.185	
2 mg/ml	25 ºC	306	0.212	43.6
	37 ºC	304	0.216	
	45 ºC	295	0.214	
4 mg/ml	25 ºC	354	0.249	40
	37 ºC	349	0.205	
	45 ºC	341	0.229	
6 mg/ml	25 ºC	361	0.211	40
	37 ºC	350	0.215	
	45 ºC	345	0.233	

4.9. Hyperthermia

Fig. 4.13 shows the induction heating properties of chitosan coated $CoFe_2O_4$ nanoferrite solutions with the application of an external rf magnetic field with the amplitude of 28 mT and frequency 400 kHz. Time dependence of the temperature curves demonstrates that the temperature increases with the increase of time linearly and turns towards a plateau value through a kink point. In Fig. 4.13 though the temperature didn't attain the saturation temperature yet the nature of the curve indicates that it would tend to attain the saturation temperature. The reason of not attaining the temperature towards a saturation value is the large anisotropy of $CoFe_2O_4$ even in the coated state. Again, large anisotropy associated with $CoFe_2O_4$ with the finite hysteresis area led to the possibility of raising the temperature of 48 °C even at the concentration as low as 0.5 mg/ml. The temperatures rise by the hyperthermia effect of folate chitosan-coated $CoFe_2O_4$ ferrite solutions of concentrations 6 mg/ml 4 mg/ml, 2 mg/ml, 1 mg/ml and 0.5 mg/ml are 66°C, 62°C, 54°C, 50°C, 48°C respectively. Here, it can be remembered that the thermotherapeutic temperature by the magnetic particle hyperthermia is in the range of 42-46 °C. This range of temperature is achievable (Fig 4.13) with the variation of maximum temperature attained in the plateau value that is almost linear and therefore it might be tuned by tuning the concentration of the nanoparticle solution. The concentration dependence of maximum temperature attained by each solution is presented in Fig. 4.14.

The specific loss power, SLP is the ultimate parameter that tells us about the efficiency of the particle heating exposed to a rf induction heating. The specific loss of power can be expressed by the equation,

$$SLP = \frac{C}{m}\frac{dT}{dt} \qquad (4)$$

In the above equation, *c* is the heat capacity of the solution, *m* is the mass of the nanoparticle, and *dT/dt* is the slope of the linear region of the curve presented in Fig. 4.13. The values of the specific loss power are presented in Table 4.4.

Table 4.4: Specific loss power (SLP) of folate chitosan-coated cobalt ferrite nanoparticles at different concentrations.

Concentration	Heat capacity, *c* ($jg^{-1}K^{-1}$)	Volume of sample (ml)	Mass, *m* (g)=concentration × 0.6/1000	*dT/dt* (slope)	SLP
0.5mg/ml	4.18	0.6	0.0003	0.00957	133.34
1mg/ml	4.18	0.6	0.0006	0.01022	71.19
2mg/ml	4.18	0.6	0.0012	0.01714	59.70
4mg/ml	4.18	0.6	0.0024	0.02174	37.86
6mg/ml	4.18	0.6	0.0048	0.03251	28.31

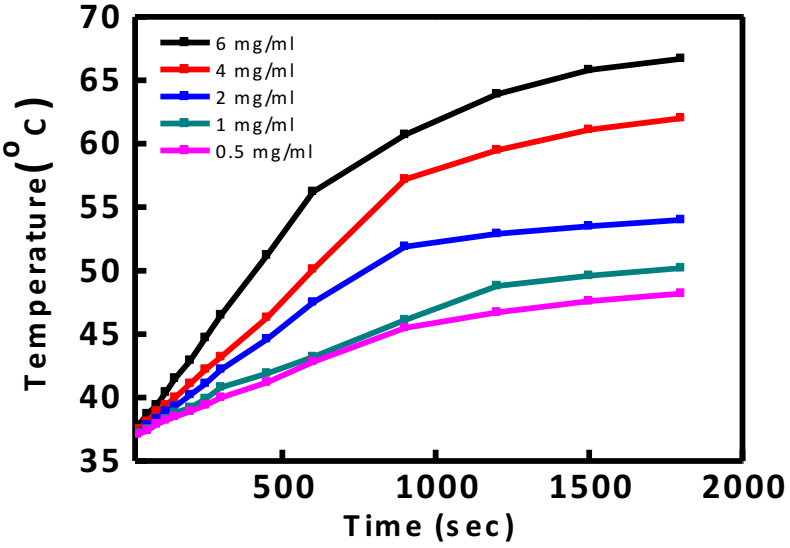

Figure 4.13: Hyperthermia of folate chitosan-coated cobalt ferrite nanoparticle at different concentration.

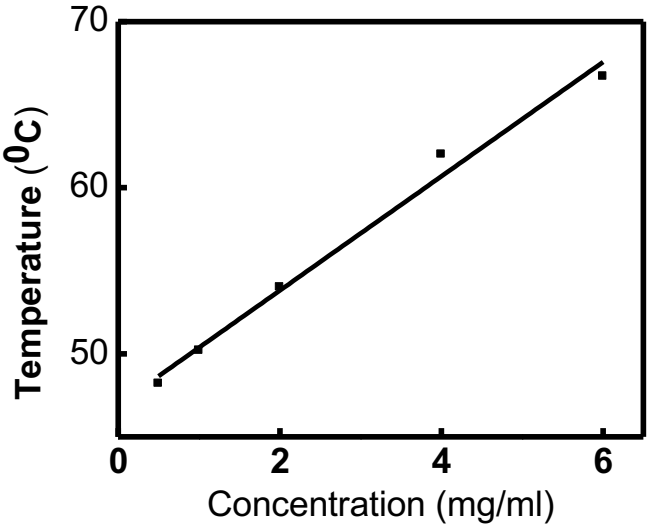

Figure 4.14: Effect of concentration on maximum temperature.

4.10 Magnetic resonance imaging (MRI)

In this study, in-vitro and in-vivo experiments were carried out using the folate chitosan coated $CoFe_2O_4$ nanoparticles as a contrast agent. In order to examine the performance of the contrast agent phantom imaging was carried out using a preclinical MRI with the static magnetic field of 3 Tesla. The phantom was prepared by filling the eppen dorf tube with the folate chitosan coated $CoFe_2O_4$ with a concentration of 0.125 mg/ml. The eppen dorf tube was placed inside a 50 ml falcon tube surrounded with a sponge. The falcon tube was placed inside a mouse bedding and body coil. The axial images were acquired with the repetition time T_R of 4000 ms and the echo time T_E starting from 7 ms with an interval of multiple of 7. The images are presented in Fig. 4.15 (a), which shows that the signal diminishes with the echo time as a result of which the white areas of the voxels darkens. The rate of darkening of the signal changes exponentially with the echo time. The data are plotted in Fig. 4.15 (b). Comparing the exponential fitting curve of Fig. 4.15 (b) with the equation $I=I_0e^{-x/T_2}$ (where I= Intensity of the MRI image, I_0= Initial Intensity of the MRI image, $1/T_2$= Relaxation time of the contrast agent, x= constant) , the relaxation time was obtained 50 ms-1 for the concentration 0.125 mg/ml.

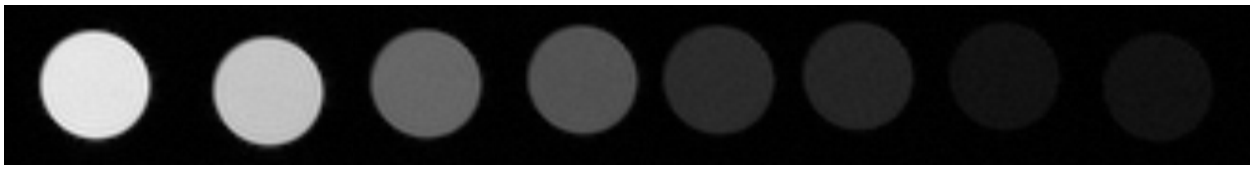

7 14 21 28 35 42 49 56

Echo Time (ms)

(a)

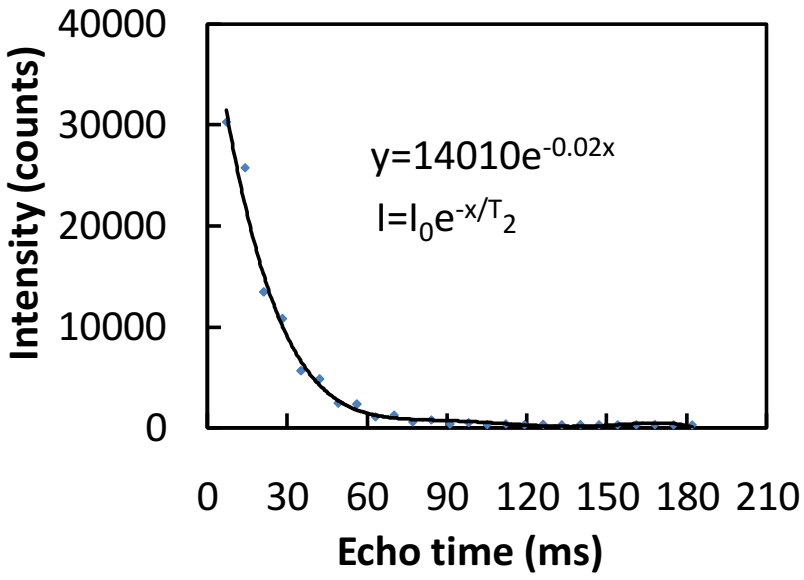

(b)

Figure 4.15: (a) the echo time dependence of spin echo images of the phantoms containing folate chitosan coated $CoFe_2O_4$ nanoparticle and (b) Exponential variation of the signal with the echo time.

In order to further evaluate the performance of the contrast agent developed in this study angiography experiments were performed. In order to carry out the in-vivo experiments, *Albino Wister* rats were used. The rat was injected with 0.5 ml of ketamine, which was sufficient for the rat to become unconscious. At first, the angiography of the whole body and brain were acquired without any contrast agent. The rat was of small size and fit into the mouse coil and bedding. After acquiring the images without a contrast agent the rat was injected with the folate chitosan coated $CoFe_2O_4$ nanoparticle as the contrast agent. After injection, the rat was allowed to stay in the same position for 30 min. and inserted into the MRI machine in the region of homogeneous magnetic field B_o=3T. The 3T magnetic field is very common for clinical applications. In Fig. 4.16 (a) angiography of whole-body rat and (b) angiography of rat brain acquired by using the time of flight (TOF) sequences were acquired. The left images of (a) and (b) are without contrast agent and the right images of (a) and (b) are with the contrast agent developed in this study namely folate chitosan coated $CoFe_2O_4$. In the time of flight experiments, the signal is saturated for the dynamic object. In this case, the dynamic object is the blood in the vasculature. Therefore, in the TOF images only blood vessels are visible. When the TOF images were acquired after injecting the contrast agent the vasculatures are more visible. While some of the veins and capillaries were not visible in the images without a contrast agent, more veins and capillaries are visible in the images with the contrast agent. This is because the signals of the dynamic fluid i.e, blood is saturated more in presence of the magnetic $CoFe_2O_4$ based contrast agent. Clearly, the contrast was enhanced for the images with contrast agent.

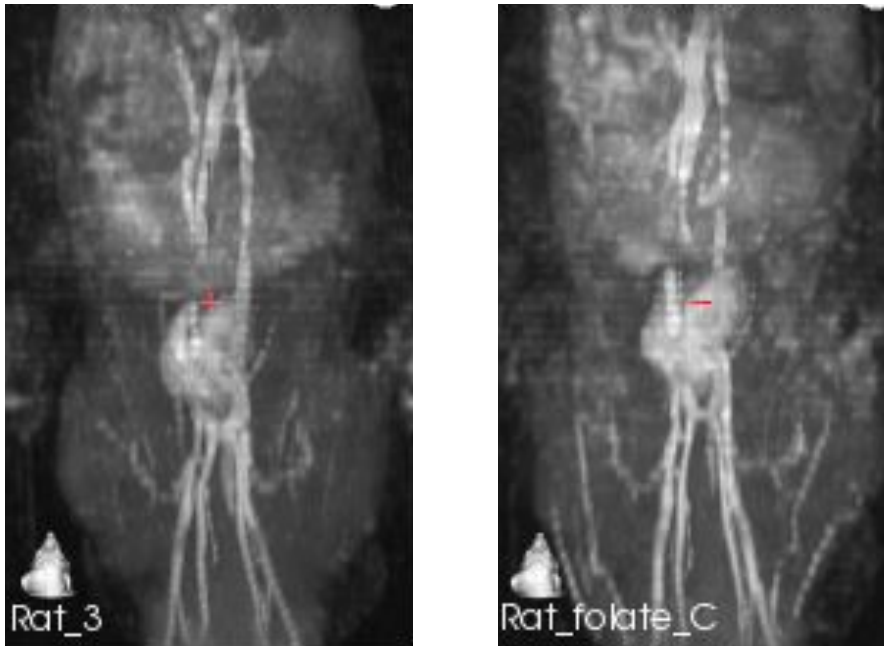

(a)

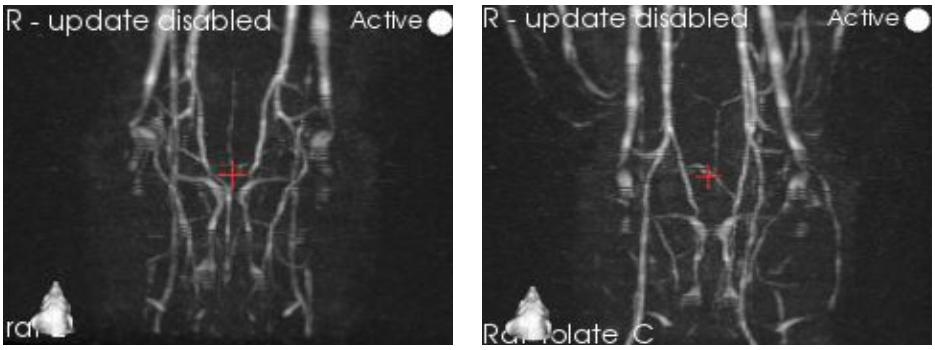

(b)

Figure 4.16: (a) The angiography of the whole body and **(b)** the angiography of rat brain using time of flight sequence. On the left of both the images are without contrast agent and on the right with contrast agent.

Chapter 5: Conclusions & Suggestion

5.1 Conclusions

Cobalt ferrite nanoparticles were synthesized by the coprecipitation method. The structure and size of the nanoparticles were confirmed by XRD, TEM, PPMS, Mössbauer, FTIR, and Raman spectroscopy. These experiments suggested that this synthesized cobalt ferrite was appropriate for biomedical applications. Therefore, the cobalt ferrite nanoparticles were coated with folate chitosan and their dynamic light scattering (DLS), magnetic induction heating and T_2 relaxivity in-vitro and in-vivo images were examined.

The XRD studies confirmed the formation of single phase with inverse spinel structure. The average crystallite size was determined using Scherrer's formula correspond to the (311) plane. The crystallite size was founded as ~12 nm. The lattice parameter was carried out to be 8.335 Å which also confirmed the inverse spinel structure. The particle size was also determined 5-15 nm from the TEM bright field, dark fields images. The selected area diffraction (SAED) patterns showed the diffraction rings of all lattice planes and HRTEM studies showed the distinct lattice fringes. These were also demonstrated good crystallinity and single-phase formation of the synthesized bare cobalt ferrite nanoparticles. The coating of folate chitosan is also confirmed by the TEM analysis.

Magnetic characterizations were performed by the physical properties measurement system (PPMS). The value of saturation magnetization for uncoated $CoFe_2O_4$ nanoparticle was 51 emu/g and it reduces to 40 emu/g for folate chitosan coated $CoFe_2O_4$. The remanence and coercivity were 15 emu/g and 679 Oe for uncoated $CoFe_2O_4$ whereas 8 emu/g and 459 Oe for coated $CoFe_2O_4$. The Mössbauer spectra provided mixed relaxation. The Mössbauer parameters like isomer shift, quadrupole splitting, hyperfine field, and cation distributions at tetrahedral (A) and octahedral (B) sites were also determined. These parameters demonstrated superparamagnetic phases embedded in the ferromagnetic matrix.

In the FTIR studies, the uncoated sample showed the octahedral and tetrahedral absorption peaks at 357 cm^{-1} and 594 cm^{-1} which confirmed the formation of the spinel structure of $CoFe_2O_4$. The shifting of the peaks of the folate chitosan coated samples confirmed their satisfactory coating. The Raman spectroscopy also confirmed the spinel structure of the uncoated sample and coating of the samples.

The thermal properties were performed by DSC-TG analysis. The DSC-TG curves show that the exothermal reaction occurred due to the dehydration of the uncoated samples. In the coated samples the exothermal reaction occurred due to dehydration as well as break-down of the folate chitosan coating.

The hydrodynamic size and polydispersity index showed a lower value at different temperatures for different concentrations. which are promising results for biomedical applications. The Zeta potential value of all the concentrations confirmed that folate chitosan was stably coated on the surface of the nanoparticles.

For biomedical applications, rf induction heating was carried out for different concentrations. The temperature was raised by the hyperthermia effect of folate chitosan coated $CoFe_2O_4$ solutions of concentrations 6 mg/ml 4 mg/ml, 2 mg/ml, 1 mg/ml and 0.5 mg/ml are 66 °C, 62 °C, 54 °C, 50 °C, 48 °C respectively. This result suggested that synthesized $CoFe_2O_4$ are potential candidate for the thermo-therapeutic application of cancer therapy. MRI images obtained from the in-vitro and in-vivo experiments based on phantoms and *Albino Wister* rats were demonstrated good contrast agent. The relaxation time was obtained 50 ms^{-1} for the concentration of 0.125 mg/ml.

5.2 Suggestions for further work

The current study has shown that magnetic nanoparticles have significant results for biomedical applications. Further study is required to develop their technological application and optimize their best properties for biological purposes. For the complete evaluation of these nanoparticles due to their promising magnetic response can be used in the magnetic hyperthermia for cancer treatment and MRI as a contrast agent for diagnosis in vivo studies should be carried out using cancer cell and tumor cells of the rats.

References

[1] R. Feynman "Plenty of room, plenty of history", *Journal of nature nanotechnology*, **4**, (2009).

[2] N. K. Tolochko, "Nanoscience and nanotechnology", *Journal of History of Nanotechnology*, SEolss Published, **40**, (2009).

[3] https://www.science.org.au/curious/technology-future/nanotechnology-where-to-from-here

[4] A. Akbarzadeh, M. Samiei, S. Davaran, "Magnetic nanoparticles: preparation, physical properties, and applications in biomedicine", *Journal of Nanoscale Research Letter*, **7(1)**, (2012), 144.

[5] M. Zhang, J. Liu, and G. Wang,"Highly Biocompatible Nanoparticles of Au@Fluorescent Polymers as Novel Contrast Agent for In Vivo Bimodality", *Journal of NIR Fluorescence/CT Imaging Contrast Media & Molecular Imaging,***11**, (2019).

[6] R. C. Huxford, R. J. Della, W. Lin, "Metal-organic frameworks as potential drug carriers", *Current Opinion in Chemical Biology*, **14**, (2010), 262-268.

[7] R. Askeland, P. Pradeep, F. Wendelin, *et al.*, "The Science and Engineering of materials 6th Edition", CL Engineering Publisher, (2010).

[8] *https://nanosense.sri.com › activities › sizematters › sizeandscale › SM_Less_2*

[9] S. C McBain, H. HP Yiu, J. Dobson**,** "Magnetic nanoparticles for gene and drug delivery", *International Journal of Nanomedicine*, **3(2)**, (2008), 169–180.

[10] L. Kafrouni and O. Savadogo *et al.,* "Recent progress on magnetic nanoparticles for magnetic hyperthermia", *Progress Biomater*, **5**, (2016), 147–160.

[11] Y. Wu, X. Yang, X. Yi *et al*, "Magnetic Nanoparticle for Biomedicine Applications", *Journal of Nanotechnol Nanomed Nanobiotechnol*, **2**, (2015), 003.

[12] S. P. Yeap, J. Lim, A. L. Ahmed *et al*., "Agglomeration, colloidal stability, and magnetic separation of magnetic nanoparticles**:** collective influences on environmental engineering applications", *Journal of Nanoparticles Research,* **19**, (2017), 368.

[13] A. S. Ethiraj, N. Hebalkar, S. Kharraz, *et al.,* "Photolumincescent core-shell particles of organic dye in silice", *Journal of Luminescence*, **114**, (2005), 115-23.

[14] P. L. Hariani, M. Faizal, R. Marsi *et al.*, "Synthesis and Properties of Fe_3O_4 Nanoparticles by Co-precipitation Method to Removal Procion Dye", *International Journal of Environmental Science and Development*, **4(3)**, (2013), 336-340.

[15] S. W. Shin, I. H. Song, S. H. Um, "Role of Physicochemical Properties in Nanoparticle Toxicity", *Journal of Nanomaterials*, **5**, (2015), 1351-1365.

[16] S. Sun, H. Zeng, D. B. Robinson *et al.,* "Monodisperse MFe_2O_4 (M= Fe, Co, Mn) Nanoparticles", *Journal of the American Chemical Society*, **126(1)**, (2004), 273-9.

[17] Q. A. Pankhurst, J. Connolly, S. K. Jones *et al.,* "Applications of magnetic nanoparticles in biomedicine", *Journal of Physics. D: Applied Phys*ics, **36**, (2003), 167-181.

[18] M. F. Huq, D. K. Saha, R. Ahmed *et al.*, "Ni-Cu-Zn Ferrite Research: A Brief Review", *Journal of Science Research*, **5 (2**), (2013), 215-233.

[19] K. M. Namara, S. A. M. Tofail, "Nanoparticles in biomedical applications", *Advances in Physics: X*, **2(1)**, (2017), 54-88.

[20] S. Sunagawa, L. P. Elho, S. Chaffron *et al.,* "Structure and function of the global ocean microbiome", *Journal of Science,* **348**, (2015), 1261359.

[21] G. G. Pircalabioru, C. Bleotu, C. Curutiu *et al.*, "Biomedical Applications of Nanoparticles," *Journal of Nanodrug delivery systems in cancer*, Chapter 2, (2019), 31-62.

[22] I. Negut, V. Grumezescu**,** "Biomedical Applications of Nanoparticles", *Journal of Nanoparticles and Hyperthermia,* Chapter 3, (2019), 63-90.

[23] Q. Zhao, L. Wang, R. Cheng et al., "Magnetic Nanoparticle- Based Hyperthermia for Head & Neck Cancer in Mouse Model", *Theranostics,* **2(1)**, (2012), 113-121.

[24] B. Issa, I.M. Obaidat, "Magnetic Nanoparticles as MRI contrast Agent", (2019).

[25] Y. Javed, K. Akhtar, H. Anwar *et al*., "MRI based on iron oxide nanoparticles contrast agents:effect of oxidation state and architecture", *Journal of Nanoparticle Research*, **19**, (2017), 366.

[26] Y. Bao, J. A. Sherwood, Z. Suna, "Magnetic iron oxide nanoparticles as T_1 contrast agents for magnetic resonance imaging", *Journal of Materials Chemistry C*, **6**, (2018).

[27] X. Li, L. Wang, Y. Fan *et al.,* "Biocompatibility and Toxicity of nanoparticles and nanotubes", *Journal of Nanomaterials,* **2012** (2012), 1-9.

[28] F. Ahmad, X. Liu, Y. Zhou *et al.,* "An in vivo evaluation of acute toxicity of cobalt ferrite ($CoFe_2O_4$) nanoparticles in larval-embryo Zebrafish (Danio rerio)", *Journal of Aquatic Toxicology,* **166,** (2015), 21-28.

[29] L. H. Azaria, G. Baldi, D.Beno *et al*., "Predictive toxicology of cobalt ferrite nanoparticles: comparative in-vitro study of different cellular models using methods of knowledge discovery from data", *Journal of Particle and fibre toxicology,* **10(1)**, (2013), 32.

[30] J. Klostergaard, C. E. Seeney, "Magnetic nanovectors for drug delivery", *Journal of Maturitas,* **73(1)**, (2012), 33-44.

[31] D. Hork, B. Rittich, A. Spanov *et al.,* "Carboxyl-functionalized magnetic microparticle carrier for isolation and identification of DNA in dairy products", *Journal of Magnetism and Magnetic Materials*, **311**, (2007), 249–254.

[32] D. S. Mathew, R. S. Juang, "An overview of the structure and magnetism of spinel ferrite nanoparticles and their synthesis in microemulsions", *Journal of Chemical Engineering*, **129(1)**, (2007), 51-65.

[33] L. Cheng, H. Ma, M. Shao *et al*., "Synthesis of folate-chitosan nanoparticles loaded with ligustrazine to target folate receptor positive cancer cells", *Molecular Medicine Reports*, **16(2)**, (2017), 1101-1108.

[34] S. M. Hoque, M. S. Hossain, S. Choudhury *et al.,* "Synthesis and characterization of $ZnFe_2O_4$ nanoparticles and its biomedical applications", *Journal of Materials Letter*, **162**, (2016) 60-63.

[35] S. Nasrin, F. U. Z. Chowdhury, S.M. Hoque, "Study of hydrodynamic size distribution and hyperthermia temperature of chitosan encapsulated zinc-substituted manganese nano ferrites suspension", *Physica B: Physics of CondensedMatter,* **143(1)**, (2019), 305-310,

[36] S. M. Hoque, Y. Huang, E. Cocco *et al.*, "Improved specific loss power on cancer cells by hyperthermia and MRI contrast of hydrophilic $Fe_xCo_{1-x}Fe_2O_4$ nanoensembles", *Contrast media & molecular imaging*, **11**, (2016), 514-526.

[37] S. M. Hoque, M. Tariq, S. I. Liba *et al.*, "Thermo-therapeutic applications of chitosan- and PEG-coated $NiFe_2O_4$ nanoparticles, *Nanotechnology*, **27**, (2016), 10.

[38] H. Das, A. Inukai, N. Debnath *et al.*, "Influence of crystallite size on the magnetic and heat generation properties of $La_{0.77}Sr_{0.23}MnO_3$ nanoparticles for hyperthermia applications", *Journal of Physics and Chemistry of Solids*, **112**, (2018), 179-184.

[39] P. Roy, S. M. Hoque, S. I. Liba *et al.*, "Investigation of various magnetic features of spinel type cobalt ferrite ($CoFe_2O_4$) nanoparticles tuned by annealing temperature", *AIP Advance*, **8**, (2018), 105-124.

[40] D. Gingasu, I. Mindru, L. Patron *et al.*, "Synthesis and Characterization of Chitosan-Coated Cobalt Ferrite Nanoparticles and Their Antimicrobial Activity", *Journal of Inorganic and Organometallic Polymers and Materials*, **28**, (2018), 1932-1941.

[41] C. Sun, R. Sze, M. Zhang, "Folic acid-PEG conjugated superparamagnetic nanoparticles for targeted cellular uptake and detection by MRI", *Journal Biomedical Materials Research Part A,* **78(3)**, (2006), 550-557.

[42] G. Unsoy, S. Yalcin, R. Khodadust *et al.*, "Synthesis optimization and characterization of chitosan coated iron oxide nanoparticles produced for biomedical applications", *Journal of Nanopart Research,* **14**, (2012), 964.

[43] Y. Il Kima, D. Kima, C. S. Leeb, "Synthesis and characterization of $CoFe_2O_4$ magnetic nanoparticles prepared by temperature-controlled coprecipitation method", *Physica B*, **337**, (2003), 42–51.

[44] S. Gyergyek, D. Makovec, A. Kodre *et al.*, "Influence of synthesis method on structural and magnetic properties of cobalt ferrite nanoparticles", *Journal of Nanopart Research*, **12**, (2010), 1263–1273.

[45] M. Houshiar, F. Zebhi, Z. J. Razi *et al.*, "Synthesis of cobalt ferrite (CoFe2O4) nanoparticles using combustion, coprecipitation, and precipitation methods: A comparison study of size, structural, and magnetic properties", *Journal of Magnetism and Magnetic Materials,* **371**, (2014), 43–48

[46] S. Amiri, H. Shokrollahi, "The role of cobalt ferrite magnetic nanoparticles in medical science", *Journal of Materials Science and Engineering*, **33**, (2013), 1-8

[47] Y. Qu, H. Yang, N. Yang *et al.*, "The effect to freaction temperature on the particle size, structure and magnetic properties of co-precipitated $CoFe_2O_4$ nanoparticles", *Journal of Materials Lett*er, **60**, (2006), 3548 – 3552

[48] Magnetism: Molecules to Materials V Edited by joel S. Miller and marc Drillon, ACS Publication, (2005).

[49] http://electrons.wikidot.com/magnetism-iron-oxide-magnetite.

[50] http://electricalacademia.com/electromagnetism/hysteresis-loop-magnetization-curve/

[51] B. D. Plouffe, S. K. Murthy, L. H. Lewis, "Fundamentals and application of magnetic particles in cell isolation and enrichment" *A review Reports on Progress in Physics,* **78(1)**, (2014), 016601

[52] C. C. Berry, S. G. Adam, "Functionalisation of magnetic nanoparticles for applications in biomedicine", *Journal Physics D Applied Physics*, **36**, (2003), 198.

[53] P. Weiss, "L hypothèse du champ moléculaire et la propriété ferromagnétique" *Journal de Physics*, **6**, **(**1907), 661.

[54] R. C. O. Handley, "Modern Magnetic Materials: Principles and applications", John Wiley & Sons, (2000)

[55] M. Prevot, D. Dunlop. L. Néel, "forty years of magnetism. Physics of the Earth and Planetary Interiors', *Elsevier*, **126**, (2001), 3-6.

[56] W. F. Brown, "Thermal Fluctuations of a Single-Domain Particle" *Journal Physics Review*, **130**, (1963), 1677.

[57] S. Laurent, D. Forge, M. Por *et al.*, "Multifunctional magnetic nanoparticles for medical imaging applications", *Chemical Review,* **108**, (2008), 2064.

[58] Z. Yuanbi, Q. Zumin, J. Huang, "Preparation and Analysis of Fe_3O_4 Magnetic Nanoparticles Used as Targeted-drug Carriers, Supported by the Technology Project of Jiangxi Provincial Education Department and Jiangxi Provincial Science Department", *Journal of Chemical Engineering,* **16(3**), (2008), 451-455.

[59] T. Sugimoto, E. Matijević, "Formation of uniform spherical magnetite particles by crystallization from ferrous hydroxide gels", *Journal of Colloid and Interface Science,* **74(1)**, (1980), 227-243.

[60] R. Massart, V. Cabuil, "Effect of some parameters on the formation of colloidal magnetite in alkaline-medium-yield and particle-size control", *Journal of de Chimie Physique et de Physico-Chimie Biologique,* **84(7-8)**, (1987), 967-973.

[61] J. P. Jolivet, M. Henry, J. Livage, Metal oxide chemistry and synthesis: from solution to solid state: Wiley-Blackwell, (2000).

[62] K. J. Klabunde, Nanoscale Materials in Chemistry, John Wiley & Sons, ACS Publications, (2004).

[63] R. Dziembaj, M. Molenda, D. Majd *et al.*, "Synthesis, thermal and electrical properties of $Li_{1+\delta}Mn_{2-\delta}O_4$ prepared by a sol–gel method", *Solid State Ionics,* **157(1)**, (2003), 81-87.

[64] D. Langevin, "Micelles and microemulsions", *Annual Review of Physical Chemistry,* **43(1)**, (1992), 341-369.

[65] B. K. Paul, S. P. Moulik, "Uses and applications of microemulsions", *Current science*, (2001), 990-1001.

[66] A. K. Gupta, M. Gupta, "Synthesis and surface engineering of iron oxide nanoparticles for biomedical applications", *Biomaterials,* **26(18)**, (2005), 3995-4021.

[67] Z. Li, L. Wei, M. Gao *et al.*, "One-Pot Reaction to Synthesize Biocompatible Magnetite Nanoparticles", *Advanced Materials,* **17(8)**, (2005), 1001-1005.

[68] A. Giri, "Photomagnetism and structure in cobalt ferrite nanoparticles"*, Applied physics letters*, **80 (13)**, (2002), 2341-2343.

[69] Z. Ristanovic, A. K. Glisovic, N. Mitrovic *et al.*, "The Influence of Mechanochemical Activation and Thermal Treatment on Magnetic Properties of the $BaTiO_3$-Fe_xO_y Powder Mixture", *Science of Sintering*, **47**, (2015), 3-14.

[70] I. Bashar, I. M. Obaidat, "Magnetic Nanoparticles as MRI contrast Agent", (2019).

[71] M. W. Dewhirst, F. A. Gibbs, R. B. Roemer *et al.*, "Hyperthermia. In: Gunderson LL, Tepper JE (eds.)", *Clinical Radiation Oncology,* **14**, (2000), 256–82.

[72] P. R. Stauffer, "Thermal therapy techniques for skin and superficial tissue disease", *Matching the Energy Source to the Clinical Need: A Critical Review*, **10297**, (2000).

[73] S. B. Edge, C. C. Compton, "The American Joint Committee on Cancer: the 7th edition of the AJCC cancer staging manual and the future of TNM", *Annals of surgicaloncology,* **17(6)**, (2010), 1471-1474.

[74] S. C. David, C. M. Townsend, Sabiston textbook of surgery: The biological basis of modern surgical practice. *Saunders*, (2002).

[75] Ambrogi, Marcello Carlo, et al. "Long-term results of radio frequency ablation treatment of stage I non-small cell lung cancer: a prospective intention-to-treat study." *Journal of Thoracic Oncology,* **6(12)**, (2011), 2044-2051.

[76] R. F. Casal, A. L. Tam, G. A. Eapen,"Radiofrequency ablation of lung tumors", *Clinics in chest medicine*, **31(1)**, (2010), 151-163.

[77] A. Chichel, J. Skowronek, M. Kubaszewska *et al.,* "Hyperthermia–description of a method and a review of clinical applications", *Reports of Practical Oncology & Radiotherapy,* **12(5)**, (2007), 267-275.

[78] A. Jordan, P. Wust, H. Fahlin *et al.,* "Inductive heating of ferrimagnetic particles and magnetic fluids: physical evaluation of their potential for hyperthermia", *International Journal of Hyperthermia,* **9(1)**, (1993), 51-68.

[79] D. K. Kim, "Energy absorption of superparamagnetic iron oxide nanoparticles by microwave irradiation." *Journal of Applied physics,* **97(10)**, (2005), 10510.

[80] V. M. Khot, A. B. Salunkhe, N. D. Thorat *et al.,* "Induction heating studies of dextran coated $MgFe_2O_4$ nanoparticles for magnetic hyperthermia." *Dalton Transactions,* **42(4)**, (2013), 1249-1258.

[81] R. W. Rand, H. D. Snow, D. G. Elliott *et al.*, "Induction heating method for use in causing necrosis of neoplasm." *U.S. Patent No*. **4**, **(**1985), 545, 368.

[82] G. Glockl, R. Hergt, M. Zeisberger *et al.,* "The effect of field parameters, nanoparticle properties and immobilization on the specific heating power in magnetic particle hyperthermia." *Journal of Physics: Condensed Matter* **18(38)**, (2006), 2935

[83] P. Li, Y. Wang, F. Zeng *et al.,* "Synthesis and characterization of folate conjugated chitosan and cellular uptake of its nanoparticles in HT-29 cells", *Carbohydrate Research,* **346(6)**, (2011), 801–806.

[84] L. Alupei, G. Lisa, A. Butnariu *et al.,* "New Folic acid-chitosan derivative based nanoparticles-potential applications in cancer therapy", *Cellulose Chem. Technol*, **51 (7-8)**, (2017), 631-648.

[85] M. S. Islam, P. Haque, T. U. Rashid *et al.,* "Core–shell drug carrier from folate conjugated chitosan obtained from prawn shell for targeted doxorubicin delivery", *Journal of Materials Science: Materials in Medicine*, **28**, (2017), 55.

[86] C. H. Kuo, Y. C. Liu, C. M. Chang *et al.*, "Optimum conditions for lipase immobilization on chitosan-coated Fe_3O_4 nanoparticles", *CarbohydPolym*, **87**, (2012), 2538.

[87] G. Binnig, H. Rohrer, C. Gerber *et al.*, "Surface Studies by Scanning Tunneling Microscopy", *Physics Review Letters*, **49**, (1982), 57.

[88]https://www.researchgate.net/figure/Figure-12-Braggs-law-A-two-dimensional-crystal-lattice-and- a-set-of-imaginary-planes-is-r_47418334_fig10

[89] F. B. E. Warren, X-ray diffraction (Addison-Wesley Publishing Company, Massachusetts, (1968).

[90] B. D. Cullity and S. R. Stock, Elements of x-ray diffraction (Prentice Hall, NJ, 2002).

[91] https://www.brainkart.com/article/Transmission-Electron-microscope---Principle,-Construction,-Working,-Advantages-and-Disadvantages_6866/

[92] S. Foner, "Versatile and Sensitive Vibrating Sample Magnetometer", *The Review of Scientific Instrument*, **30**, (1959), 548.

[93] D.O, Smith, "Development of Vibrating Coil Magnetometer", *The Review of Scientific Instrument,* **27**, (1956), 261.

[94] https://en.wikipedia.org/wiki/Vibrating-sample_magnetometer.

[95] O. Leupold, J. Pollmann, E. Gerdau *et al.*, "Nuclear resonance scattering of synchrotron radiation at the 21.5 keV resonance of 151-Eu*"*, *Europhysics Lett*ers, **35**, (1996), 671.

[96] A. Konjhodzic, A. Adamczyk, F. Vagizov *et al.*, "Nuclear forward scattering vs. conventional Mdssbauer studies ofatomically tailored Eu-based materials" *Hyperfine Int*, **170,** (2006), 83.

[97] P. Gutlich, R. Link, A. Trautwein, "Mossbauer Spectroscopy and Transition", Metal Chemistry, (1978), Springer, Heidelberg.

[98] P. Gutlich, J. Ensling, "Inorganic Electronic Structure and Spectroscopy". Edited by E. I. Solomon and A. B. P. Lever, (1999).

[99] U. Gonser, "Topics in applied physics, Mossbauer Spectroscopy", *Springer-Verlag New York, LLC*, **5**, (1975).

[100] G. K. Werthein, "Mössbauer Effect: Principle and Application". Academic Press, New York, (1964).

[101] U. Goner, "Topics in Applied Physics: Springerverlag, Berlin Heidelberg, New York", **4**, (1973)

[102] https://www.rsc.org/Membership/Networking/InterestGroups/MossbauerSpect/part2p

[103] R. Finsy, "Particle sizing by quasi-elastic light scattering", *Advance. Colloid Interface Science*, **52**, (1994), 79–143.

[104] R. H. Müller, R. Schuhmann and K. Thode, "Particle size analysis in laboratory practice", (1996)

[105] https://www.particletechlabs.com/analytical-testing/particle-size-distribution-analyses/dynamic-light-scattering

[106] B. J. Kirby, E. F. Hasselbrink, "Zeta potential of microfluidic substrates: 1. Theory, experimental techniques, and effects on separations", *Electrophoresis,* **25**, (2004), 187–202

[107] D. A. Long, "*Raman Spectoscopy"*, McGraw-Hill, Inc., New York, (1977).

[108] R. L. McCreery, "*Raman Spectroscopy for Chemical Analysis",* John Wiley & Sons, Inc., New York, (2000).

[109] A. A. Bunaciu, E. G. Udristioiu, H. Y. Aboul- Enein, "X-Ray Diffraction: Instrumentation and Applications", *Critical Reviews in Analytical Chemistry*, **45 (4)**, (2015), 289–299.

[110] I. H. Gul, A. Maqsood, "Structural, magnetic and electrical properties of cobalt ferrites prepared by the sol–gel route", *Journal of Alloys and Compounds,* **465(1–2)**, (2008), 227-231.

[111] A. B. Salunkhe, V. M. Khot, N. D. Thorat *et al.,* "Polyvinyl alcohol functionalized cobalt ferrite nanoparticles for biomedical applications", *Applied Surface Science*, **264**, (2013), 598-604.

[112] R. Sagayaraj, S. Aravazhi, P. Praveen *et al.*, "Structural, morphological and magnetic characters of PVP coated $ZnFe_2O_4$ nanoparticles", *Journal of Materials Science: Materials in Electronics*, **29(3)**, (2018), 2151–2158.

[113] A. Jha, K. Prasad, "Biological synthesis of cobalt ferrite", *Nanotechnology Development*, **2**, (2012).

[114] S. K. Gore, S. S. Jadhav, S. M. Patange *et al.*, "The structural and magnetic properties of dual phase cobalt ferrite", *Scientific Reports***, 7**, (2017), 2524.

[115] R. S. Yadav, I. Kuritka, J. Vilcakova *et al.*, "Impact of grain size and structural changes on magnetic, dielectric, electrical, impedance and modulus spectroscopic characteristics of $CoFe_2O_4$ nanoparticles synthesized by honey mediated sol-gel combustion method, *Advances in Natural Sciences: Nanoscience and Nanotechnology,* **8 (045002)**, (2017), 14.

[116] A. Tiwari, A. Singh, A. Debnath *et al.*, "Multifunctional Magneto-Fluorescent Nanocarriers for Dual Mode Imaging and Targeted Drug Delivery", *ACS Applied Nano Materials*, **2(5)**, (2019), 3060-3072.

[117] J. D. Baraliya, H. H. Joshi, "Spectroscopy investigation of nanometric cobalt ferrite synthesized by different techniques"*, Vibrational Spectroscopy*, **74**, (2014), 75-80**.**

[118] P. Chandramohan, M. P. Srinivasan, S. Velmurugan *et al.*, "Cation distribution and particle size effect on Raman spectrum of $CoFe_2O_4$", *Journal Solid State Chemistry*, **184(1)**, (2011), 84 -89

[119] T. Yu, Z. X. Shen, Y. Shi *et al.*, "Cation migration and magnetic ordering in spinel $CoFe_2O_4$ powder: micro-Raman scattering study", *Journal Physics: Condensed Matter,* **14**, (2002), 613.

[120] K. Maaz, S. Karim, A. Mumtaz *et al.*, "Synthesis and magnetic characterization of nickel ferrite nanoparticles prepared by co-precipitation route", *Journal Magnetism and Magnetic Materials*, **321(12)**, (2009), 1838-1842.

[121] M. Danaei, M. Dehghankhold, S. Ataei *et al.*, "Impact of Particle Size and Polydispersity Index on the Clinical Applications of Lipidic Nanocarrier Systems", *Pharmaceutics,* **10(2)**, (2018), 5773.

[122] P. Martins, C. M. Casta, M.Benelmekki, "On the origin of the electroactive poly (vinylidenefluride) β-phase nucleation by ferrite nanopartices via surface electrostatic interactions", *Crystal Engineering Communication*, **14**, (2012), 2807.

[123] K. H. Bae, M. Park, M. J. Do *et al.*, "Chitosan Oligosaccharide-Stabilized Ferrimagnetic Iron Oxide Nanocubes for Magnetically Modulated Cancer Hyperthermia", *Journal of ACS nano*, **6(6)**, (2012), 5266–5273.

[124] R. K. Singh, A. Narayan, K. Prasad *et al.*, "Thermal, structural, magnetic and photoluminescence studies on cobalt ferrite nanoparticles obtained by citrate precursor method", *Journal Thermal Analysis Calorimetry*, **110(2)**, (2012), 573-580.